



Defense Threat Reduction Agency
8725 John J. Kingman Road, MS
6201 Fort Belvoir, VA 22060-6201



DTRA-TR-17-50

TECHNICAL REPORT

Fragmentation of Solid Materials Using Shock Tubes. Part 2: First Test Series in a Large-Diameter Shock Tube

Distribution Statement A. Approved for public release; distribution is unlimited.

December 2017

HDTRA1-14-C-0001

Bryan Bewick et al.

Prepared by:
Protection Engineering
Consultants
P.O. Box 781607
San Antonio, TX 78278

DESTRUCTION NOTICE:

Destroy this report when it is no longer needed.
Do not return to sender.

PLEASE NOTIFY THE DEFENSE THREAT REDUCTION
AGENCY, ATTN: DTRIAC/ RD-NTF, 8725 JOHN J. KINGMAN ROAD,
MS-6201, FT BELVOIR, VA 22060-6201, IF YOUR ADDRESS
IS INCORRECT, IF YOU WISH IT DELETED FROM THE
DISTRIBUTION LIST, OR IF THE ADDRESSEE IS NO
LONGER EMPLOYED BY YOUR ORGANIZATION.

REPORT DOCUMENTATION PAGE

Form Approved
OMB No. 0704-0188

Public reporting burden for this collection of information is estimated to average 1 hour per response, including the time for reviewing instructions, searching existing data sources, gathering and maintaining the data needed, and completing and reviewing this collection of information. Send comments regarding this burden estimate or any other aspect of this collection of information, including suggestions for reducing this burden to Department of Defense, Washington Headquarters Services, Directorate for Information Operations and Reports (0704-0188), 1215 Jefferson Davis Highway, Suite 1204, Arlington, VA 22202-4302. Respondents should be aware that notwithstanding any other provision of law, no person shall be subject to any penalty for failing to comply with a collection of information if it does not display a currently valid OMB control number. **PLEASE DO NOT RETURN YOUR FORM TO THE ABOVE ADDRESS.**

1. REPORT DATE (DD-MM-YYYY)		2. REPORT TYPE	3. DATES COVERED (From - To)		
4. TITLE AND SUBTITLE			5a. CONTRACT NUMBER		
			5b. GRANT NUMBER		
			5c. PROGRAM ELEMENT NUMBER		
6. AUTHOR(S)			5d. PROJECT NUMBER		
			5e. TASK NUMBER		
			5f. WORK UNIT NUMBER		
7. PERFORMING ORGANIZATION NAME(S) AND ADDRESS(ES)			8. PERFORMING ORGANIZATION REPORT NUMBER		
9. SPONSORING / MONITORING AGENCY NAME(S) AND ADDRESS(ES)			10. SPONSOR/MONITOR'S ACRONYM(S)		
			11. SPONSOR/MONITOR'S REPORT NUMBER(S)		
12. DISTRIBUTION / AVAILABILITY STATEMENT					
13. SUPPLEMENTARY NOTES					
14. ABSTRACT					
15. SUBJECT TERMS					
16. SECURITY CLASSIFICATION OF:			17. LIMITATION OF ABSTRACT	18. NUMBER OF PAGES	19a. NAME OF RESPONSIBLE PERSON
a. REPORT	b. ABSTRACT	c. THIS PAGE			19b. TELEPHONE NUMBER (include area code)

UNIT CONVERSION TABLE

U.S. customary units to and from international units of measurement*

U.S. Customary Units	Multiply by Divide by [†]	International Units
Length/Area/Volume		
inch (in)	2.54 × 10 ⁻²	meter (m)
foot (ft)	3.048 × 10 ⁻¹	meter (m)
yard (yd)	9.144 × 10 ⁻¹	meter (m)
mile (mi, international)	1.609 344 × 10 ³	meter (m)
mile (nmi, nautical, U.S.)	1.852 × 10 ³	meter (m)
barn (b)	1 × 10 ⁻²⁸	square meter (m ²)
gallon (gal, U.S. liquid)	3.785 412 × 10 ⁻³	cubic meter (m ³)
cubic foot (ft ³)	2.831 685 × 10 ⁻²	cubic meter (m ³)
Mass/Density		
pound (lb)	4.535 924 × 10 ⁻¹	kilogram (kg)
unified atomic mass unit (amu)	1.660 539 × 10 ⁻²⁷	kilogram (kg)
pound-mass per cubic foot (lb ft ⁻³)	1.601 846 × 10 ¹	kilogram per cubic meter (kg m ⁻³)
pound-force (lbf avoirdupois)	4.448 222	newton (N)
Energy/Work/Power		
electron volt (eV)	1.602 177 × 10 ⁻¹⁹	joule (J)
erg	1 × 10 ⁻⁷	joule (J)
kiloton (kt) (TNT equivalent)	4.184 × 10 ¹²	joule (J)
British thermal unit (Btu) (thermochemical)	1.054 350 × 10 ³	joule (J)
foot-pound-force (ft lbf)	1.355 818	joule (J)
calorie (cal) (thermochemical)	4.184	joule (J)
Pressure		
atmosphere (atm)	1.013 250 × 10 ⁵	pascal (Pa)
pound force per square inch (psi)	6.984 757 × 10 ³	pascal (Pa)
Temperature		
degree Fahrenheit (°F)	[T(°F) - 32]/1.8	degree Celsius (°C)
degree Fahrenheit (°F)	[T(°F) + 459.67]/1.8	kelvin (K)
Radiation		
curie (Ci) [activity of radionuclides]	3.7 × 10 ¹⁰	per second (s ⁻¹) [becquerel (Bq)]
roentgen (R) [air exposure]	2.579 760 × 10 ⁻⁴	coulomb per kilogram (C kg ⁻¹)
rad [absorbed dose]	1 × 10 ⁻²	joule per kilogram (J kg ⁻¹) [gray (Gy)]
rem [equivalent and effective dose]	1 × 10 ⁻²	joule per kilogram (J kg ⁻¹) [sievert (Sv)]

* Specific details regarding the implementation of SI units may be viewed at <http://www.bipm.org/en/si/>.

[†] Multiply the U.S. customary unit by the factor to get the international unit. Divide the international unit by the factor to get the U.S. customary unit.

EXECUTIVE SUMMARY

The report describes the second of four test series, each of which is part of an overall effort to develop a probabilistic, physics-based model for the fragmentation of building components subjected to airblast. The primary objective of this second test series was to explore how conventional façade wall components fragment under relatively long duration, low pressure loads. A secondary objective was to explore how the façade material – glass, concrete, and masonry – affected fragment size and velocity distributions.

A large-diameter explosively-driven shock tube was employed to produce the desired low pressure, long duration loads. The long-durations were achieved using long line charges of Primacord and spaced packets of Unigel.

Five full-scale samples were tested in this series, namely, three 4-ft x 6-ft tempered glass windows, one 8-ft x 8-ft minimally-reinforced concrete masonry unit (CMU) wall, and one 8-ft x 8-ft reinforced concrete panel, each carefully fabricated and mounted to replicate real-world construction techniques.

In the glass tests, the fragment size and velocity distributions were estimated using rear-view and side-view high-speed video. In these cases, a positive Weibull distribution obtained the best fit. In the CMU wall test, dust obscured the high-speed video. Thus the fragment size distribution was estimated by physically collecting over 800,000 fragments. In this case, a negative Weibull distribution (i.e., a power law) obtained the best fit. The concrete panel cracked, folded and displaced, but otherwise survived with minimal fragment production.

Contents

Executive Summary	i
1 Background	1
1.1 Purpose and Scope	1
1.2 Testing Overview	2
1.3 Test Setup.....	3
2 Results Overview	9
2.1 Window Glass Tests	9
2.2 CMU Wall Tests	13
2.3 Concrete Panel	15
3 Fragment Distribution Analysis Techniques	16
3.1 Analysis of Early-Time Rear-View High-Speed Videos.....	16
3.2 Analysis of Mid-Time Side-View High-Speed Videos	17
3.2.1 Frag Track Analysis Methodology.....	17
3.2.2 Frag Track Velocity Analysis Validation Using Kinovea	19
3.3 Analysis of Late-Time Physically-Collected Fragments	19
4 Results.....	22
4.1 Introduction.....	22
4.2 Analysis and Distribution Fit Approach	22
4.3 Mass Distributions From SigmaScan Analysis of Rear-View HSV.....	24
4.4 Mass and Velocity Distributions from Side-View HSV Analysis.....	29
4.5 Mass Distributions From Physical Collection Analysis	36
5 Conclusions.....	38
6 References.....	40
Appendix A: LS-DYNA Results for Test Planning and Design.....	41
A.1. LS-DYNA Results for Concrete Slabs.....	41
A.2. LS-DYNA Results for CMU Walls.....	43
Appendix B: Large Diameter Shock Tube Pressure Data	45

Figures

Figure 1. SRI’s 8-ft diameter 257-ft-long shock tube with a 12-ft diameter 10-ft-long expansion chamber.....	3
Figure 2. Typical test setup including shock tube, expansion section, sample mounting and fragment containment structure.	4
Figure 3. A view of glass sample set-up used in Tests 17, 18 and 19.	4
Figure 4. A view of CMU sample set-up used in Test 20.....	5
Figure 5. Design schematic for CMU wall sample used in Test 20.	6
Figure 6. A view of concrete panel sample set-up used in Test 21.	7
Figure 7. Design schematic for concrete panel sample used in Test 21.	7
Figure 8. An illustration of the high-speed video camera and lighting setup.	8
Figure 9. Pressure gauge locations.....	9
Figure 10. Reflected pressure histories for glass window samples in a) Test 17 and b) Test 19.	10
Figure 11. Zoomed in view of peak pressure waveform in Test 19.	10
Figure 12. Glass fragmentation approximately 10ms after the airblast arrived for a) Test 17 and b) Test 19.	11
Figure 13. Glass fragmentation in Test 17 at 0ms, 5ms, 10ms, and 15ms after the shock arrived.	12
Figure 14. Glass fragmentation in Test 19 at 0ms, 5ms, 10ms, and 15ms after the shock arrived.	13
Figure 15. Reflected pressure history for CMU wall sample in Test 20.	14
Figure 16. CMU fragmentation in Test 20 shortly after the airblast arrived.	14
Figure 17. Reflected pressure history for concrete panel sample in Test 21.	15
Figure 18. Reinforced concrete panel failure in Test 21 at three different times after the airblast arrived.	16
Figure 19. Progression of image analysis for size distribution using SigmaScan for Test 17.17	
Figure 20. SigmaScan fragment tracings based on rear-view high-speed video for a) Test 17, b) Test 18, and c) Test 19.....	17
Figure 21. Frag Track used to estimate airborne fragment velocities from side-view HSV. .	18
Figure 22. Frack Track applied to two glass tests. (a) Test 18, (b) Test 19.....	18
Figure 23. Frag Track applied to a reinforced concrete slab test (Test 21).	19
Figure 24. Kinovea applied to a reinforced concrete panel (Test 21).....	19
Figure 25. Fragments generated in Test 20: a) designated collection area immediately after testing; b) after using a series of increasingly finer sieves to sort fragments into size bins.	20
Figure 26. Digital photographs of the fragments captured in Sieve no. 4 in Test 20 arrayed on a flat surface. The top shows the original full-color image. The bottom shows a high-contrast grey-scale image produced by SigmaScan.	21
Figure 27. SigmaScan results for Sieve no. 4 in Test 20. Fragments were identified and measured in SigmaScan. The results were output to and post-processed in a MS Excel spreadsheet.	22
Figure 28. Best-fit Weibull mass distribution for rear-view HSV test data for PDF (top) and CDF (bottom) for Test 17 for tempered glass.....	26
Figure 29. Best-fit Weibull mass distribution for rear-view HSV test data for PDF (top) and CDF (bottom) for Test 18 for tempered glass.....	27

Figure 30. Best-fit Weibull mass distribution for rear-view HSV test data for PDF (top) and CDF (bottom) for Test 19 for tempered glass.....	28
Figure 31. Best-fit Weibull mass distribution for rear-view HSV test data for PDF (top) and CDF (bottom) for Tests 17, 18 and 19 for tempered glass.	29
Figure 32. Best-fit Weibull mass distribution for side-view HSV test data for PDF (top) and CDF (bottom) for Test 18 involving tempered glass.....	31
Figure 33. Best-fit Weibull mass distribution for side-view HSV test data for PDF (top) and CDF (bottom) for Test 19 involving tempered glass.....	32
Figure 34. Best-fit Weibull mass distribution for side-view HSV test data for PDF (top) and CDF (bottom) for Tests 18 and 19 involving tempered glass.....	33
Figure 35. Glass fragments experience mid-air collisions leading to breakup in Test 17.....	34
Figure 36. Best-fit Weibull velocity distribution for rear-view HSV test data for CDF for Test 18 involving tempered glass.	35
Figure 37. Best-fit Weibull velocity distribution for rear-view HSV test data for CDF for Test 19 involving tempered glass.	35
Figure 38. Best-fit Weibull velocity distribution for side-view HSV test data CDF for Tests 18 and 19 involving tempered glass.....	36
Figure 39. Best-fit power law mass distribution for physically-collected test data for PDF (top) and CDF (bottom) for Test 20 involving CMU.....	37
Figure 40. Response of 5-1/2"-thick simply-supported solid concrete panel (p=50-psi, t=100-msec) predicted by LS-DYNA.....	42
Figure 41. Response of 5-1/2"-thick, fixed-fixed solid concrete panel (p=50-psi, t=100-msec) as predicted by LS-DYNA.....	42
Figure 42. Response of 4" architectural precast panel (p=50-psi, t=100-msec) as predicted by LS-DYNA.....	43
Figure 44. Response of partially grouted CMU wall (p=50-psi, t=100-msec) as predicted by LS-DYNA.....	44
Figure 46. Test 17 P0 A-location pressure gauge data.	45
Figure 47. Test 17 P0 B-location pressure gauge data.....	45
Figure 48. Test 17 P1 east pressure gauge data.	46
Figure 49. Test 17 P1 west pressure gauge data.	46
Figure 50. Test 17 P12 pressure gauge data.	47
Figure 51. Test 17 P20 pressure gauge data.	47
Figure 52. Test 17 P39 pressure gauge data.	48
Figure 53. Test 17 P80 pressure gauge data.	48
Figure 54. Test 17 P118 pressure gauge data.	49
Figure 55. Test 17 P176 pressure gauge data.	49
Figure 56. Test 18 P0 A-location pressure gauge data.	50
Figure 57. Test 18 P0 B-location pressure gauge data.....	50
Figure 58. Test 18 P1 east pressure gauge data.	51
Figure 59. Test 18 P1 west pressure gauge data.	51
Figure 60. Test 18 P12 pressure gauge data.	52
Figure 61. Test 18 P20 pressure gauge data.	52
Figure 62. Test 18 P39 pressure gauge data.	53
Figure 63. Test 18 P80 pressure gauge data.	53
Figure 64. Test 18 P118 pressure gauge data.	54

Figure 65. Test 18 P176 pressure gauge data.	54
Figure 66. Test 19 P0 A-location pressure gauge data.	55
Figure 67. Test 19 P0 B-location pressure gauge data.....	55
Figure 68. Test 19 P1 east pressure gauge data.	56
Figure 69. Test 19 P1 west pressure gauge data.	56
Figure 70. Test 19 P12 pressure gauge data.	57
Figure 71. Test 19 P20 pressure gauge data.	57
Figure 72. Test 19 P39 pressure gauge data.	58
Figure 73. Test 19 P80 pressure gauge data.	58
Figure 74. Test 19 P118 pressure gauge data.	59
Figure 75. Test 19 P176 pressure gauge data.	59
Figure 76. Test 20 P1 east pressure gauge data.	60
Figure 77. Test 20 P1 west pressure gauge data.	60
Figure 78. Test 20 P12 pressure gauge data.	61
Figure 79. Test 20 P20 pressure gauge data.	61
Figure 80. Test 20 P39 pressure gauge data.	62
Figure 81. Test 20 P80 pressure gauge data.	62
Figure 82. Test 20 P118 pressure gauge data.	63
Figure 83. Test 20 P176 pressure gauge data.	63
Figure 84. Test 21 P1 east pressure gauge data.	64
Figure 85. Test 21 P1 west pressure gauge data.	64
Figure 86. Test 21 P12 pressure gauge data.	65
Figure 87. Test 21 P20 pressure gauge data.	65
Figure 88. Test 21 P39 pressure gauge data.	66
Figure 89. Test 21 P80 pressure gauge data.	66
Figure 90. Test 21 P118 pressure gauge data.	67
Figure 91. Test 21 P176 pressure gauge data.	67

Tables

Table 1. Large diameter shock tube experiment parameters.	2
Table 2. Sample properties.	3
Table 3. Summary of measurement techniques.	22
Table 4. Statistical parameters for rear-view HSV mass in Tests 17, 18, and 10 involving plate glass test objects.	25
Table 5. Best-fit Weibull parameters based on rear-view HSV mass in Tests 17, 18, and 10 involving plate glass test objects.	25
Table 6. Statistical parameters for side-view HSV mass in Tests 18 and 19 involving plate glass test objects.	30
Table 7. Best-fit Weibull parameters based on side-view HSV mass in Tests 18 and 19 involving plate glass test objects.	30
Table 8. Best-fit Weibull parameters based on side-view HSV velocity in Tests 18 and 19 involving plate glass test objects.	34
Table 9. Statistical parameters for physical collection in Test 20 with a CMU wall.	36
Table 10. Best-fit power law parameter based on physical collection in Test 20 with a CMU wall.	36
Table 11. Summary of best-fit Weibull and power law size distributions.	38

1 BACKGROUND

This report is the second in a four part series:

- Part 1. Measured fragment size distributions, velocity size distributions, and the time-dependency of fragment size distributions in a large number of different small-scale tests [1].
- Part 2 (*this report*). Measured fragment size distributions in a small number of different large-scale tests. These tests showed that, in some cases, the size distributions obtained at small scales in Part 1 also occur at large scales.
- Part 3. Measured fragment size distributions in a large number of different small-scale tests. Increased the range of test conditions to obtain a wider variety of fragment size distributions than in Part 1. In particular, the experimental techniques used in Part 1 were modified to allow for higher-pressures and increased fragment sample sizes.
- Part 4. Measured fragment size distributions in a small number of different large-scale tests. Building on Part 2, this test series provided further evidence that the size distributions obtained at small scales in Parts 1 and 3 may also occur at large scales.

All of these tests used explosively-driven shock tubes [2]. Shock tubes have rarely, if ever, been used to systematically study fragmentation prior to this work. Parts 1 and 3 used a small (6.5-in diameter) shock tube to load square plates with relatively short-duration high-overpressure airblast, creating conditions where material properties (e.g., strength, density) dominate structural response (e.g., bending, flexing). Parts 2 and 4 used a large (8 ft diameter) shock tube to load realistic building façade panels and roofing sections with relatively long-duration low-overpressure air blast, creating conditions where structural response dominates material properties.

1.1 PURPOSE AND SCOPE

The primary objective of this test series was to explore how building façade components fragment under relatively long duration, low pressure loads. A secondary objective was to explore how fragment size and velocity distributions vary for three common façade materials: tempered glass, concrete masonry unit (CMU) and reinforced concrete.

This test series was performed in an explosively-driven 8-ft-diameter 257-ft-long shock tube located at SRI's privately-owned Corral Hollow Experiment Site (CHES). An expansion chamber was mounted to the shock tube exit, which increased the diameter to 12-ft and the length to 267-ft.

This shock tube was used to fragment realistic, full-scale building façade panels using peak overpressures ranging from 8 to 80 psi and overpressure durations ranging from 80 to 160ms. By contrast, an earlier test series in SRI International's explosively-driven 6.5-in-diameter 37-ft-long shock tube obtained peak overpressures ranging from 250 to 4,000 psi and overpressure durations ranging from 5 to 25ms [1]. This illustrates the tradeoff between high overpressures and extended durations inherent to explosively-driven shock tubes. Because of the larger time and length scales, this test series produced significant global structural level (SL) responses, such as bending and flexing, while the earlier test series produced mainly local material level (ML) responses.

1.2 TESTING OVERVIEW

Table 1 and Table 2 summarize the five tests completed in this series. Notice that Tests 1 to 16 took place in the previous test series [1] while Tests 17 to 21 took place in the current test series. The long overpressure durations in this test series were obtained using techniques described in Reference [2].

Table 1. Large diameter shock tube experiment parameters.

Test	Sample	Charge	Peak Reflected Overpressure (psi)				Approximate Duration (ms)				Impulse (psi-ms)			
			A ¹	B ¹	East ¹	West ¹	A ¹	B ¹	East ¹	West ¹	A ¹	B ¹	East ¹	West ¹
17	4-ft x 6-ft x ¼-in Fully Tempered Glass	2x150 gr/ft. Primacord suspended over 0 ft. to 120 ft. ⁴ (total charge weight: 2.3 kg)	8.3	9.6	10.3	12.7	135.8	136.1	137.6	122.9	508.9	549.5	443.4	548.7
18	4-ft x 6-ft x ¼-in Fully Tempered Glass	Same as Test 17	14.3	11.0	11.5	11.1	156.6	150.9	124.9	130.7	612.4	660.9	658.3	658.6
19	4-ft x 6-ft x ¼-in Fully Tempered Glass	26 Unigel packets ⁵ spaced 3 ft. apart attached to 50 gr/ft. Primacord suspended over 0 ft. to 80 ft. ⁴ (total charge weight: 13.5 kg)	31.9	31.3	28.0	28.1	N/A ²	N/A ²	99.3	102.9	N/A ²	N/A ²	873.5	869.7
20	8-ft x 8-ft x 8-in CMU	57 Unigel packets ⁵ spaced 17 in. apart attached to 50 gr/ft. Primacord suspended over 0 ft.-80 ft. ⁴ (total charge weight: 29.4 kg)	N/A ³	N/A ³	68.3	78.0	N/A ³	N/A ³	84.0	79.1	N/A ³	N/A ³	1779.0	1787.4
21	8-ft x 8-ft x 5.5-in Concrete	35 Unigel packets ⁵ (3 Unigel packets evenly spaced over 8 ft. to 32 ft. ⁴) (4 Unigel packets evenly spaced over 32 ft. to 48 ft. ⁴) (8 Unigel packets evenly spaced over 48 ft. to 64 ft. ⁴) (20 Unigel packets evenly spaced over 64 ft. to 80 ft. ⁴) attached to 50 gr/ft. Primacord suspended over 8 ft. to 80 ft. ⁴ (total charge weight: 18.1 kg)	N/A ³	N/A ³	48.0	48.8	N/A ³	N/A ³	111.9	111.7	N/A ³	N/A ³	1614.8	1614.8

¹ See gage locations and accompanying description in Figure 9 below

² Full or partial loss of test data due to instrumentation/trigging failures

³ Gages not included in these tests

⁴ All distances are measured from the driver end of the shock tube.

⁵ Unigel packets are 2 in.-diameter and 8-in. long and weigh 0.51 kg each

Table 2. Sample properties.

Test	Description	Dimensions	Weight (lbs.)	Strength (psi)	Notes
17	Fully Tempered Glass Window	4-ft x 6-ft x ¼-in	81.4 (*)	13,500	Mounted in the center of a thick steel plate.
18	Fully Tempered Glass Window	4-ft x 6-ft x ¼-in	81.4 (*)	13,500	Mounted in the center of a thick steel plate.
19	Fully Tempered Glass Window	4-ft x 6-ft x ¼-in	81.4 (*)	13,500	Mounted in the center of a thick steel plate.
20	Concrete Masonry Unit (CMU) Wall	8-ft x 8-ft x 8-in	2,720	2,000	Two vertical reinforcement columns, 4-ft on-center, welded to a steel frame. CMU blocks partially grouted and tuck pointed on top.
21	Reinforced Concrete Panel	8-ft x 8-ft x 5.5-in	4,250	6,940 (**)	Reinforced by #5 steel rods w/18-in spacing in both directions. Rod ends, embedded steel plates and clips were welded to a steel frame.

(*) Estimated weight of glass plus white paint coating.

(**) Unconfined compressive strength (UCS) was 6500-psi.

The window samples were 4-ft x 6-ft x 0.25-in fully-tempered (FT) glass sheets mounted in rigid metal frames. The glass was not specifically strength tested; the strength reported in Table 2 is typical. The CMU sample was a partially-grouted, minimally-reinforced wall with two vertical reinforcement columns spaced 4-ft on-center. The CMU strength reported in Table 2 is an estimate of prism strength for medium weight CMU. The reinforced concrete sample was a 5.5-in thick solid panel. To evaluate its strength, concrete cylinders were tested 7, 14, and 28 days after pour. These samples achieved significantly higher strengths than the design specification of 4,000-psi.

1.3 TEST SETUP

Figure 1 shows SRI International’s 8-ft-diameter 257-ft-long shock tube with a 12-ft-diameter 10-ft-long expansion chamber mounted on the exit.

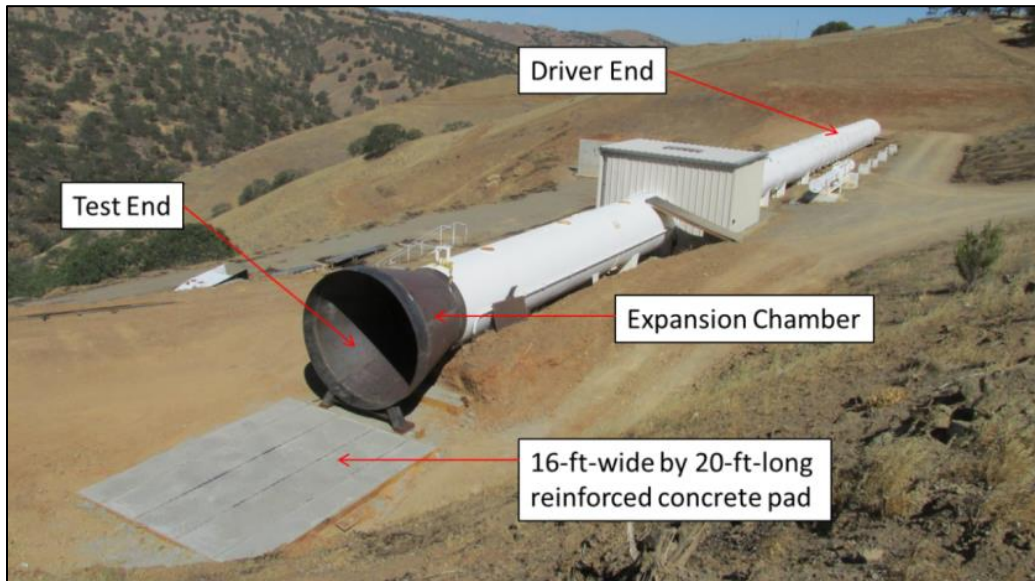


Figure 1. SRI’s 8-ft diameter 257-ft-long shock tube with a 12-ft diameter 10-ft-long expansion chamber.

Figure 2 shows a typical test setup including the shock tube, expansion chamber, test sample and fragment containment system. The fragment containment system consisted of layers of tarps, carpets, and Kevlar blankets mounted on a hollow structural steel (HSS) frame, backed by layers of honeycomb cardboard pallets and a 0.75-in-thick steel plate. The cardboard pallets were 6-in thick for glass samples and 16-in thick for concrete and CMU samples. Notice that the first test series [1] used a similar fragment containment system, minus the cardboard and steel backer. Both the driver and the test end of the shock tube were confined. On the driver end, the confining

structure was a massive steel plate; a gap was introduced between the steel plate and the driver end to allow pressure release. On the test end, the confining structure was the test article and its support.

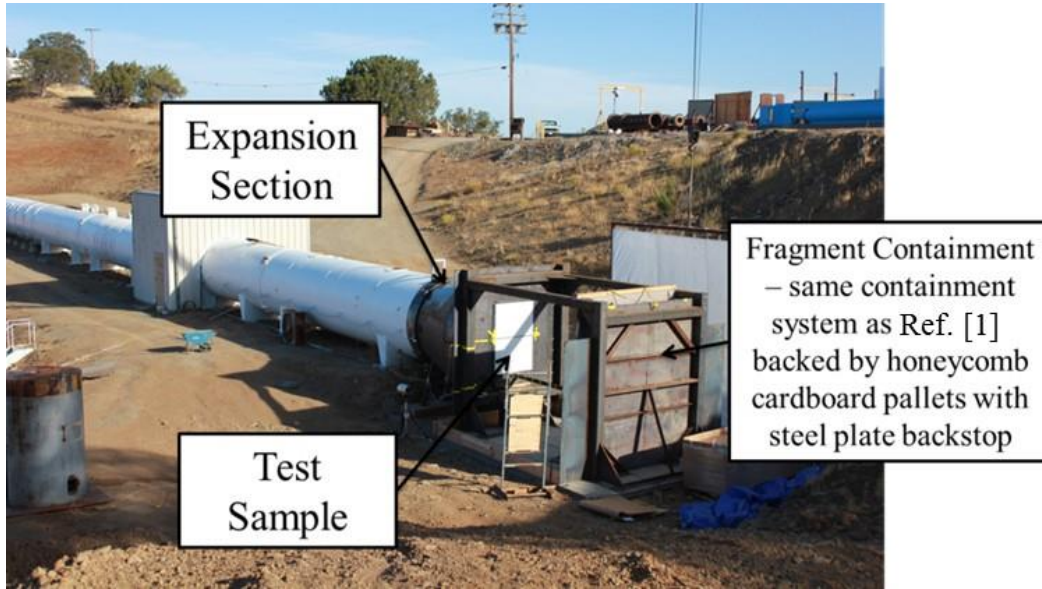


Figure 2. Typical test setup including shock tube, expansion section, sample mounting and fragment containment structure.

Figure 3 shows the plate glass used in Tests 17, 18 and 19. The windows were mounted in the center of a thick steel plate. The steel plate was bolted onto a steel frame. The steel frame was attached to the end of the expansion chamber. The glass was painted white on both sides to make the resulting fragments more easily visible in high-speed video.

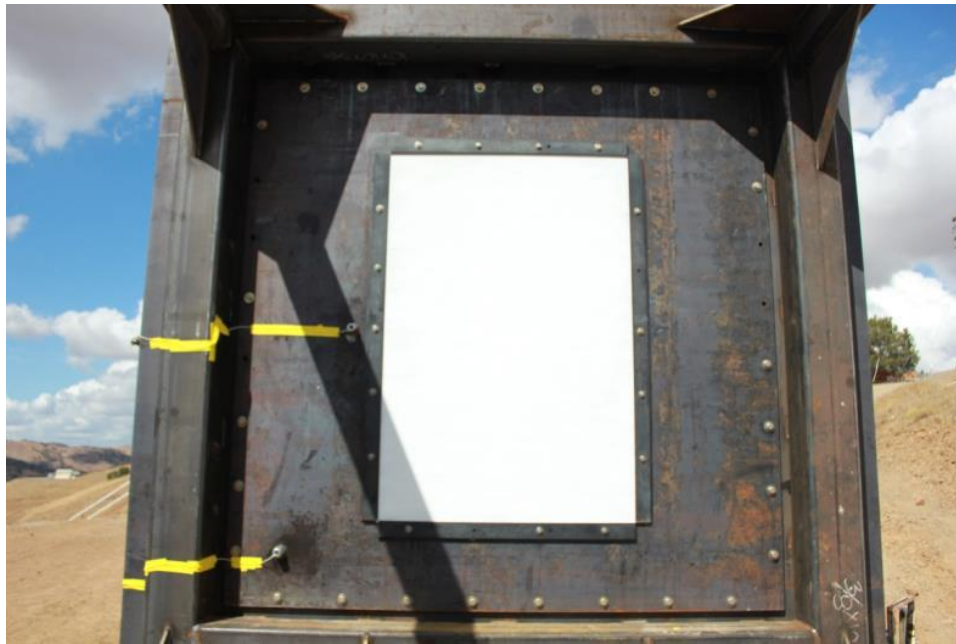


Figure 3. A view of glass sample set-up used in Tests 17, 18 and 19.

Figure 4 and Figure 5 show the CMU wall used in Test 20. To simulate dowelled connections to structural members, the vertical reinforcements in the CMU wall were welded to the top and bottom of an angle-steel frame. The angle-steel frame was attached to the end of the expansion chamber. After attaching the frame, the CMU wall was tuck-pointed at the top, a typical construction method in which the gap between the top of the wall and the ceiling (or, in this case, the steel frame) is filled with a layer of mortar. A tuck-pointed CMU wall has a higher horizontal-load-bearing capacity. Tuck-pointing leads to compression arching, i.e., the wall develops a vertical compressive force that resists horizontal flexure.

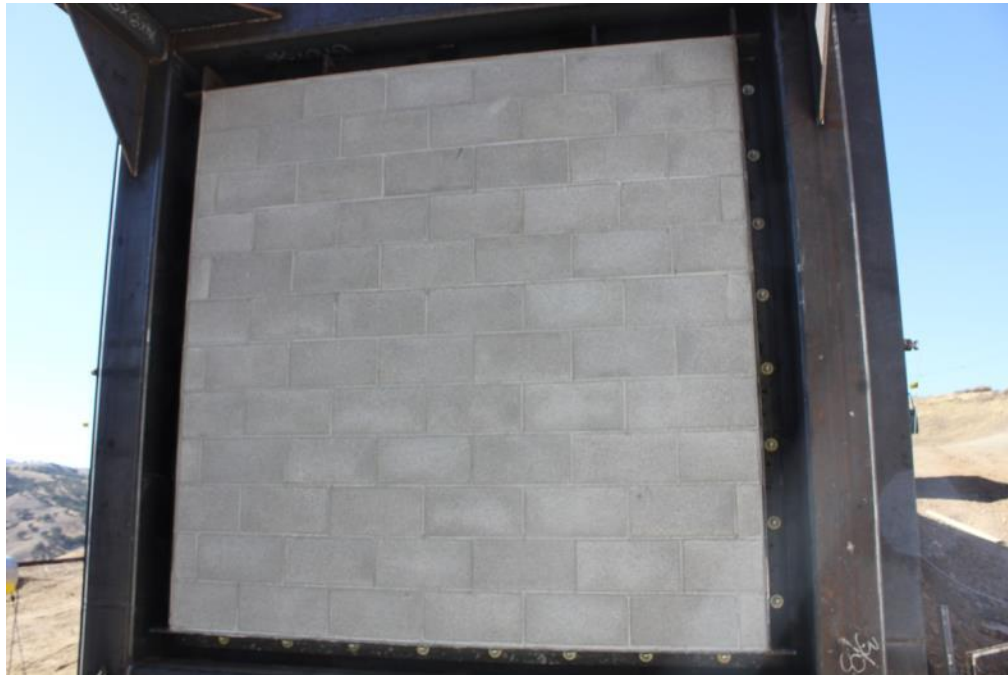


Figure 4. A view of CMU sample set-up used in Test 20.

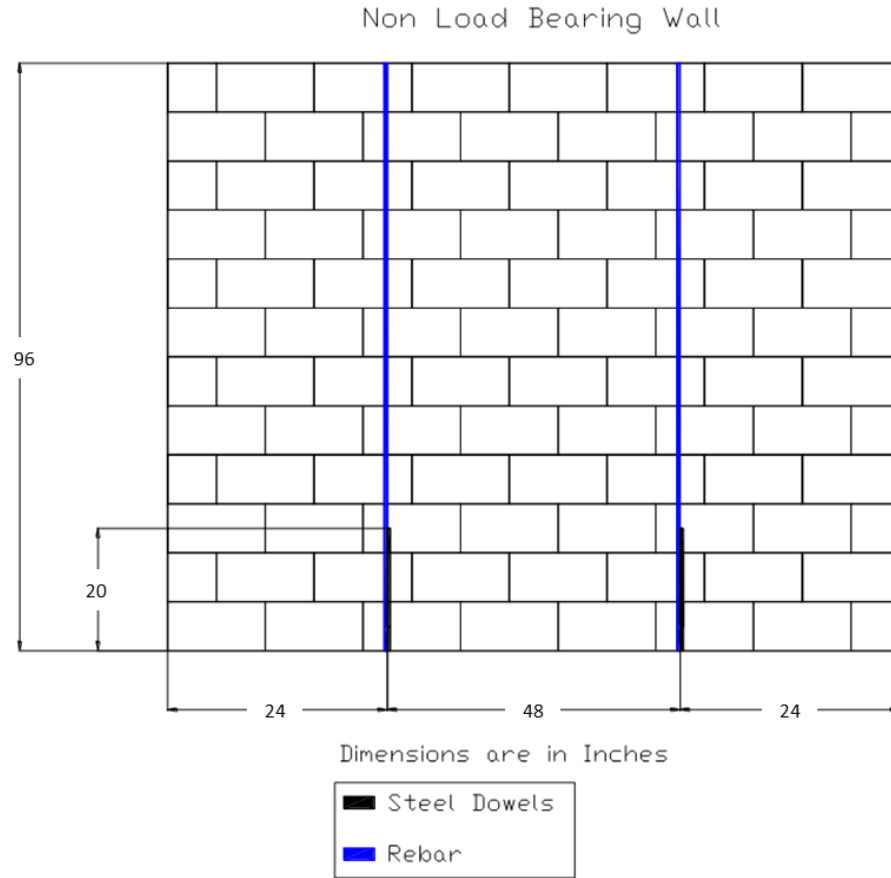


Figure 5. Design schematic for CMU wall sample used in Test 20.

Figure 6 and Figure 7 show the concrete panel used in Test 21. Reinforcement consisted of one mat of #5-bars with 18-in spacing in both directions, located at the panel mid-thickness. The panel was connected to the test frame by six 3/8-in-thick A36-steel angle clips located along the top and bottom. These clips were welded to both the test frame and to plates that were embedded in the panel itself. For these welds, E70XX electrodes obtained a throat thickness of around 1/4-in. The reinforcing rods were welded to an angle steel frame, as well as to embed plates located at the top and bottom in the rear, which simulates typical reinforced concrete panel construction methods. The angle-steel frame was then bolted to the end of the expansion chamber.



Figure 6. A view of concrete panel sample set-up used in Test 21.

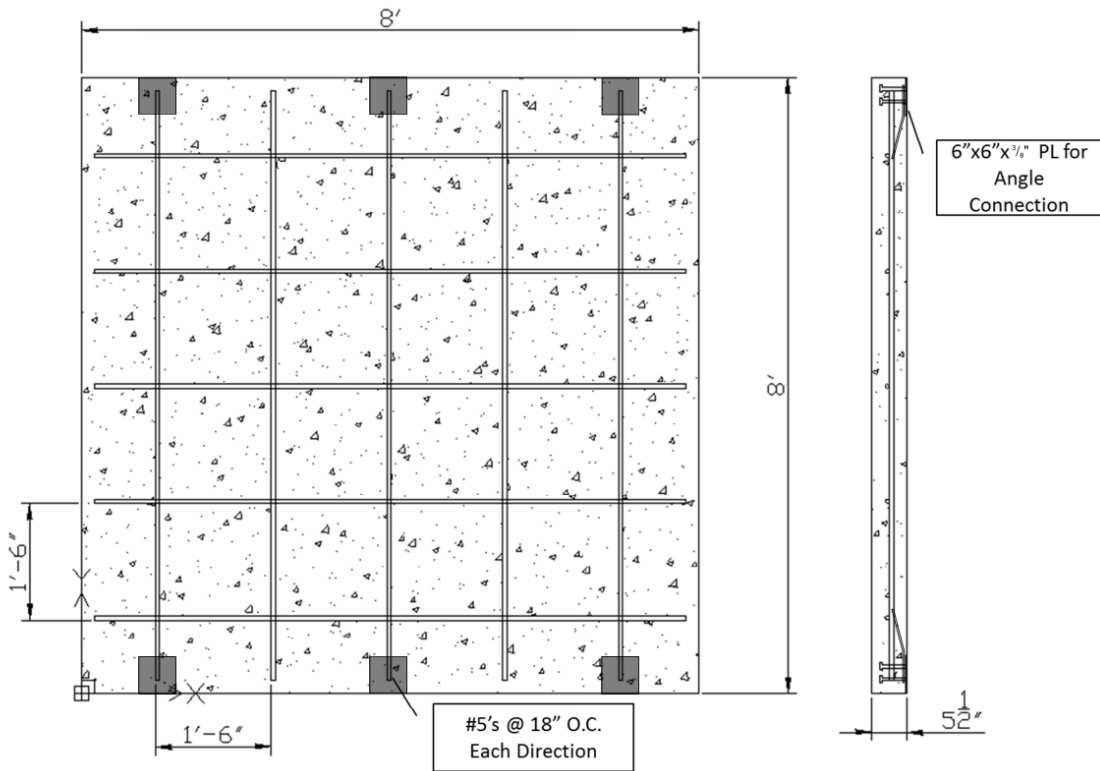


Figure 7. Design schematic for concrete panel sample used in Test 21.

Figure 8 shows the high-speed video (HSV) cameras and lighting setup used in this test series.

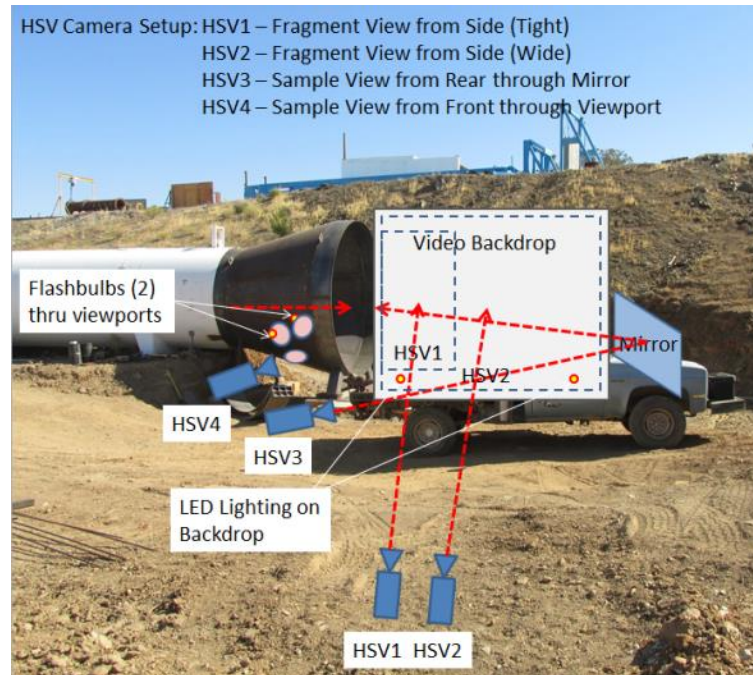


Figure 8. An illustration of the high-speed video camera and lighting setup.

The earlier test series used a fragment stripper to ensure that all fragments recorded by the side-view HSV camera traveled in or near a single plane [1]. However, the fragment stripper eliminated all but a limited random subset of the largest fragments, making it difficult to infer the underlying full-range fragment size distribution. Thus the fragment stripper was eliminated from this test series. However, for analysis purposes, it was still necessary to assume that the fragments were traveling in a single plane at a fixed distance from the side-view HSV camera. This meant that fragments traveling out-of-plane – either toward or away from the side-view HSV camera – appeared to have a lower velocity than they actually had. In addition, this meant that fragments located closer to the side-view HSV camera than the assumed plane appeared to be larger than they actually were and, conversely, fragments located farther from the side-view HSV camera than the assumed plane appeared to be smaller than they actually were.

As shown in Figure 9, Kulite pressure transducers were placed in strategic locations including the following:

- along the length of the shock tube to evaluate the developing shock wave
- flush with the wall of the 12-ft-diameter expansion chamber close to the test article
- in the support structure next to the test article to measure reflected peak pressure.

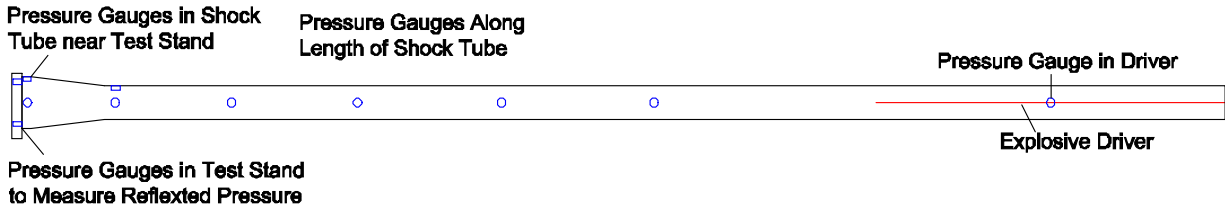


Figure 9. Pressure gauge locations.

The pressure gauge locations were labeled as follows:

- P0A - Vertical centerline next to glass sample
- P0B - Lower corner of glass sample holder
- P1E - East side of shock tube, at 1.5-in from end of tube
- P1W - West side of shock tube, at 1.5-in from end of tube
- P12 - 12.4-ft from end of shock tube (in concrete transition zone)
- P20 - 20-ft from end of shock tube (before area change transition)
- P39 - 39-ft from end of shock tube
- P80 - 80-ft from end of shock tube
- P118 - 118-ft from end of shock tube
- P176 - 176-ft from end of shock tube (inside explosive driver)

Data from the pressure gauges were collected using a Nicolet Odyssey data acquisition system; see Appendix B for a full set of plots of pressure gage information.

2 RESULTS OVERVIEW

The test objective was to obtain experimental data for the mass and speed of façade debris generated by low-pressure, long-duration blast loads impinging on full-scale structural components. In such cases, structural components fail primarily due to flexure, as opposed to the high-strain-rate crushing or impact-type failures that occur at higher overpressures.

2.1 WINDOW GLASS TESTS

Tests 17, 18 and 19 involved fully-tempered glass with dimensions of 4-ft x 6-ft x 0.25-in. Figure 10 compares the reflected pressure-time histories for Tests 17 and 19. Averaging over all gages, Tests 17 and 18 had peak static overpressures of approximately 10psi while Test 19 had a peak static overpressure of approximately 30psi; see Table 1.

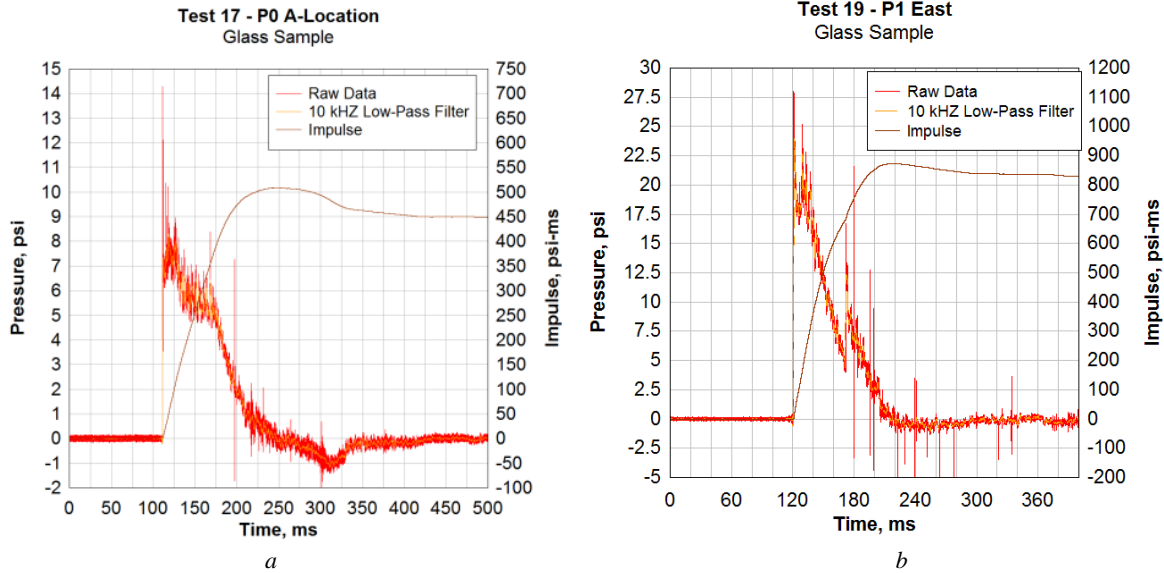


Figure 10. Reflected pressure histories for glass window samples in a) Test 17 and b) Test 19.

In general, the reflected pressure spiked briefly before achieving a second sustained peak. For example, Figure 11 shows a magnified view of the initial pressure pulse in Test 19.

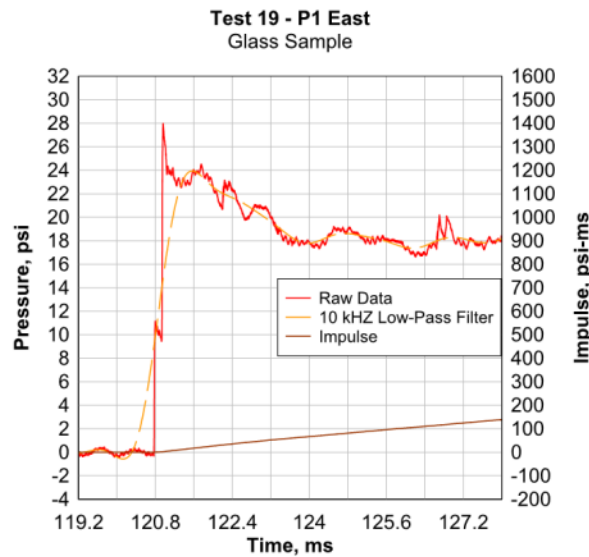


Figure 11. Zoomed in view of peak pressure waveform in Test 19.

Figure 12 shows a rear view of the glass samples in Tests 17 and 19 approximately 10-ms after the airblast arrived. In both cases, the fragments were smaller near the periphery and larger near the center of the panel. As expected, the fragments in Test 19 were visibly smaller than those in Test 17, due to the increased pressure.



Figure 12. Glass fragmentation approximately 10ms after the airblast arrived for a) Test 17 and b) Test 19.

Figure 13 and Figure 14 show rear views of the glass samples in Tests 17 and 19, respectively, at 0ms, 5ms, 10ms, and 15ms after the airblast arrives. As expected, the number of fragments increased, and the size of the fragment decreased, over time.

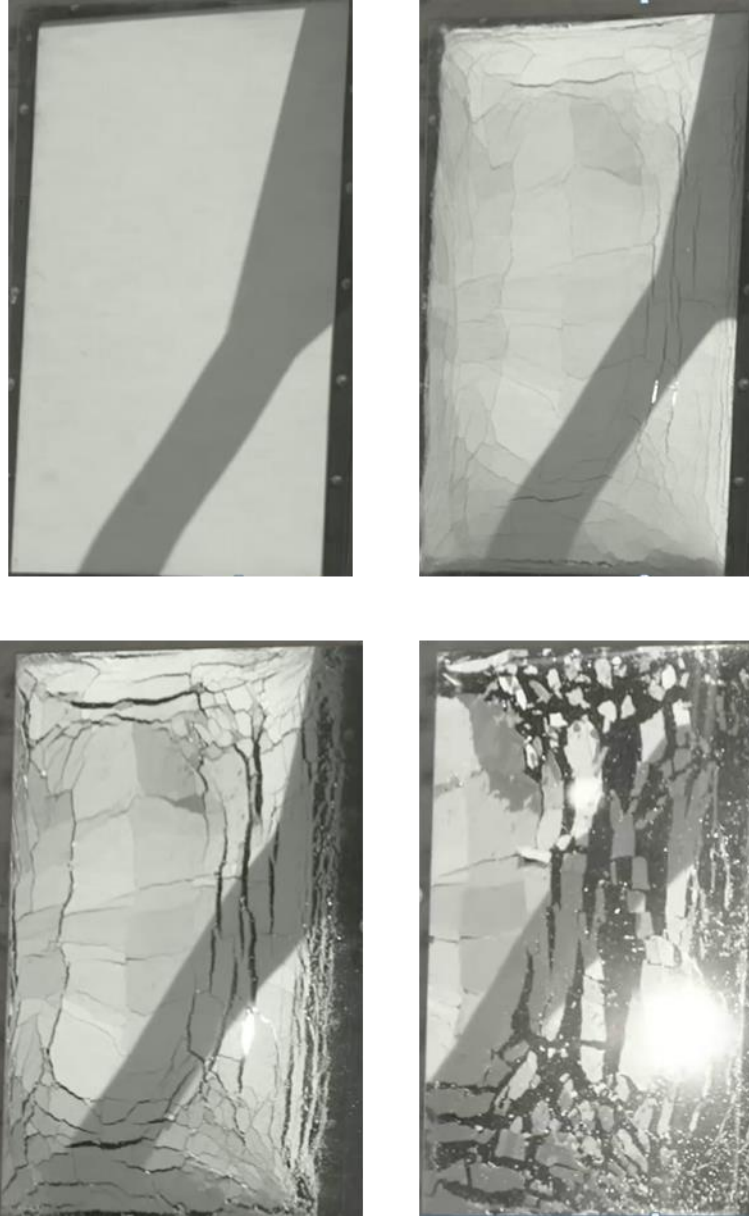


Figure 13. Glass fragmentation in Test 17 at 0ms, 5ms, 10ms, and 15ms after the shock arrived.



Figure 14. Glass fragmentation in Test 19 at 0ms, 5ms, 10ms, and 15ms after the shock arrived.

2.2 CMU WALL TESTS

Test 20 involved a concrete masonry unit (CMU) wall with dimensions of 8-ft x 8-ft x 8-in. Figure 15 shows the reflected pressure-time history for Test 20. Notice that the overpressure spiked to 63-psi for about 2-msec and then dropped to 45-psi for about 30-msec.

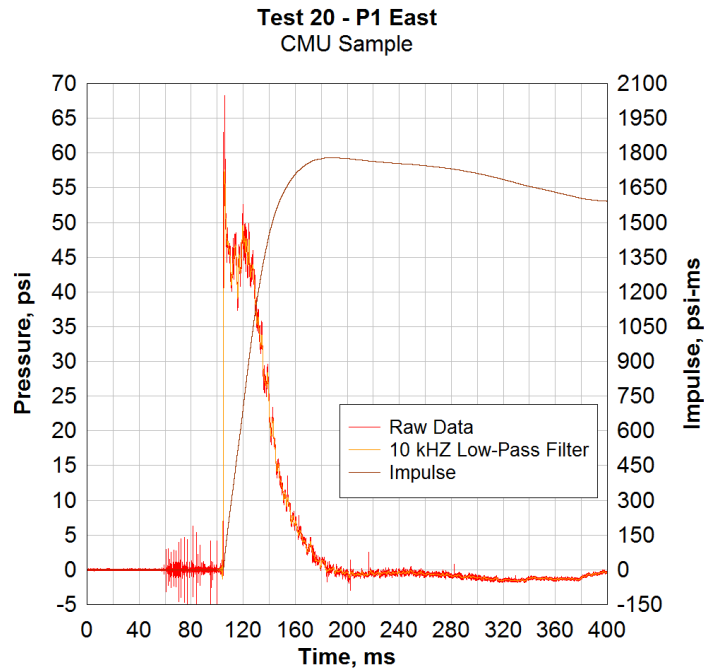


Figure 15. Reflected pressure history for CMU wall sample in Test 20.

Figure 16 shows a rear view of the CMU wall in Test 20 shortly after the airblast arrived. This demonstrates that, at first, the wall failed preferentially along mortar joints. However, as time progressed, the blocks themselves increasingly fractured, including the CMU face shells. The block and mortar failures produced large amounts of dust that heavily obscured the high-speed video.



Figure 16. CMU fragmentation in Test 20 shortly after the airblast arrived.

2.3 CONCRETE PANEL

Test 21 involved a reinforced concrete panel with dimensions of 8-ft x 8-ft x 5.5-in. Figure 17 shows the reflected pressure-time history for Test 21. The overpressure spiked to 45-psi for about 1-msec and then dropped to 25-psi for about 30-msec.

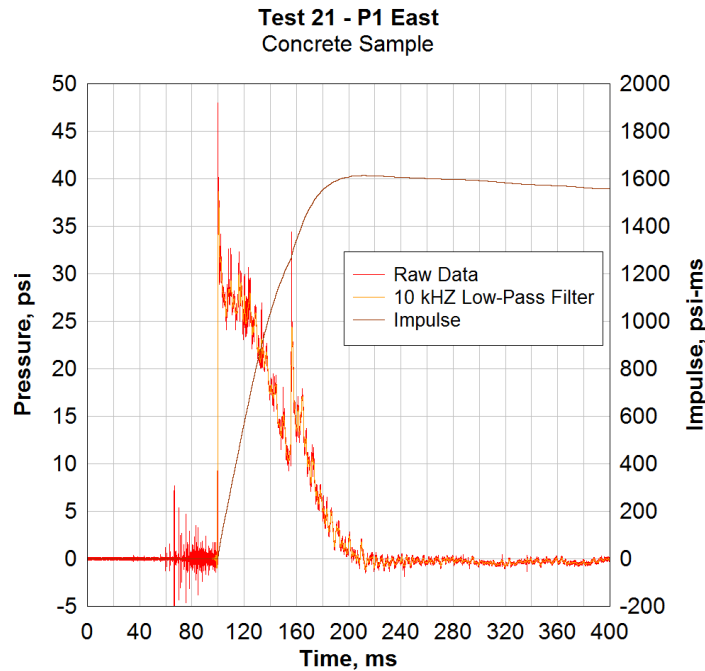


Figure 17. Reflected pressure history for concrete panel sample in Test 21.

Figure 18 shows a side view of the reinforced concrete panel at three different times following the airblast arrival. Notice that the concrete panel experienced severe hinging at the panel mid-span. In addition, the welds holding the reinforced concrete panel in the steel frame failed, and the entire panel displaced downstream as a unit. Unlike the previous tests, only a small fraction of the concrete sample fragmented, primarily the compressed regions on the back of the folded panel. More fragmentation would have occurred if the connections between the panel and the frame were stronger. However, stronger connections would not be realistic. In typical construction, stronger connections are associated with larger façade panels spanning multiple stories and/or lightly-reinforced load-bearing walls that are well-tied into the floor and roof slabs. For multi-story façade panels, intermediate floor slabs act as bearing points, allowing a tension membrane response to develop, leading to greater flexure and fragmentation.

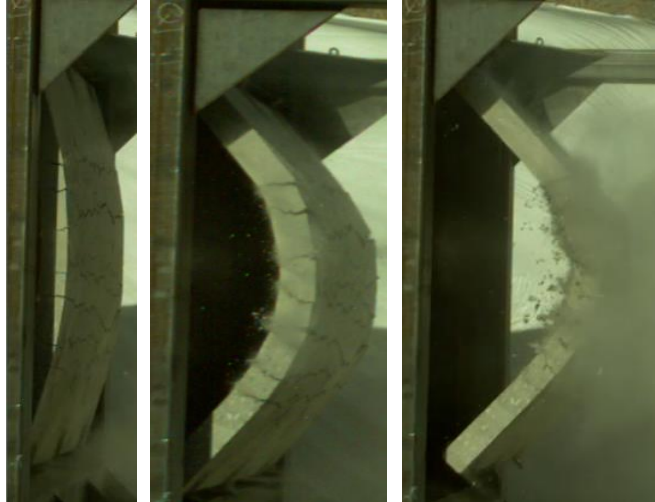


Figure 18. Reinforced concrete panel failure in Test 21 at three different times after the airblast arrived.

3 FRAGMENT DISTRIBUTION ANALYSIS TECHNIQUES

For Tests 17, 18 and 19 involving tempered glass, three digital image processing software tools were used to characterize debris size and velocity distributions. First, SigmaScan, a well-known commercial image analysis package, was used to estimate fragment sizes from the rear-view HSV. Second, Frag Track, a custom tool developed by PEC, was used to estimate fragment sizes and velocities from the side-view HSV. Finally, Kinovea, a free open-source video analysis tool, was used to validate Frag Track's velocity estimates.

For Test 20 involving CMU, physical collection was used to characterize the debris size. For Test 21 involving reinforced concrete, an attempt was made to estimate fragment sizes and velocities from the side-view HSV using Frag Track and Kinovea. However, the results are not considered reliable, due to the small sample size, and are not reported here.

3.1 ANALYSIS OF EARLY-TIME REAR-VIEW HIGH-SPEED VIDEOS

In the three glass tests, SigmaScan was used to estimate the early-time fragment size distributions based on selected frames from the rear-view high-speed video. As seen in Figure 19 and Figure 20, one quadrant in each selected frame was pre-processed to subtract the background and to outline the fragments monochromatically. SigmaScan was then used to analyze the images and create a tabular CSV file listing fragment area, length, width, aspect ratio and other statistics.



Figure 19. Progression of image analysis for size distribution using SigmaScan for Test 17.

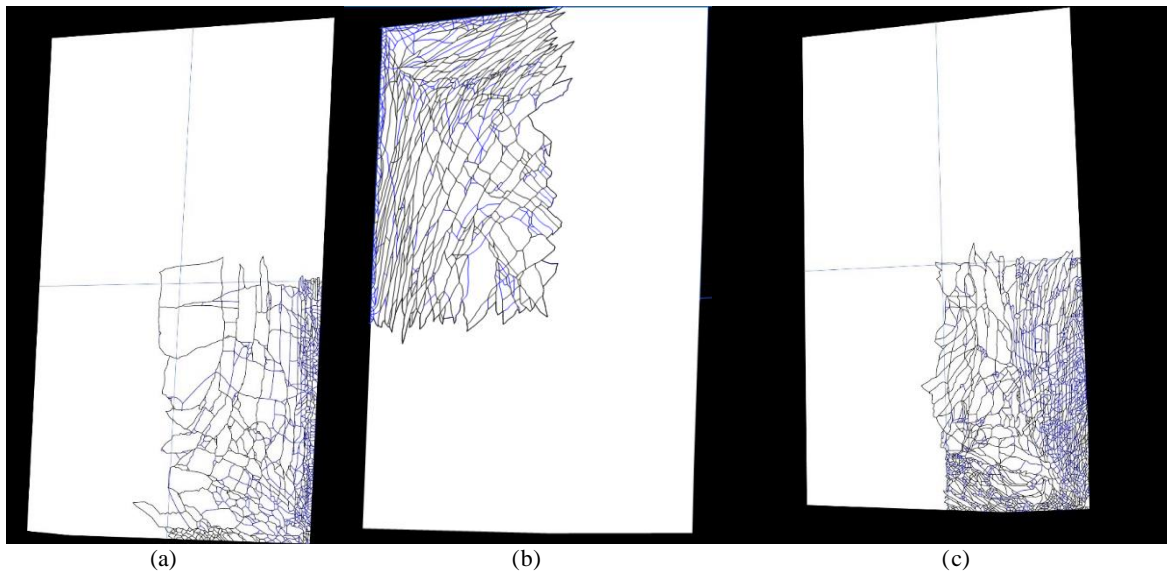


Figure 20. SigmaScan fragment tracings based on rear-view high-speed video for a) Test 17, b) Test 18, and c) Test 19.

3.2 ANALYSIS OF MID-TIME SIDE-VIEW HIGH-SPEED VIDEOS

3.2.1 FRAG TRACK ANALYSIS METHODOLOGY

In two of the three glass tests, Frag Track was used to estimate fragment sizes and velocities based on the side-view high-speed video. Frag Track has two main options, one for low and one for high obscuration conditions. Only the low obscuration option was used in this test series. As seen in Figure 21, in this option, the user selects a reference frame, and the algorithm tracks anything that is not part of the reference frame.



Figure 21. Frag Track used to estimate airborne fragment velocities from side-view HSV.

The location of each detected fragment is displayed and tracked over time, leading to estimates of each fragment’s travel distance (measured in number of pixels), travel time (measured in number of frames), area (measure in number of pixels) and aspect ratio (unitless). The Frag Track output is converted to physical units using conversion factors determined from a fiduciary video, which involves recording a planar object (“ruler”) with markings of known sizes. More specifically, the fragment velocity is converted from pixels/frame into ft/sec based on the frame rate of the camera and the fiduciary. As noted earlier, this conversion underestimates the fragment velocity for objects traveling outside of the fiduciary plane. Similarly, the fragment area is converted from the number of pixels to in² based on the average aspect ratio during the time that the fragment is tracked. As noted earlier, this conversion underestimates the sizes of fragments located behind the fiduciary plane and overestimates the sizes of fragments located in front of the fiduciary plane.

As seen in Figure 22 Frag Track worked well for two of the three glass tests, namely, Tests 18 and 19. However, in Test 17, failed background material resulted in large numbers of false positives. As seen in Figure 23, Frag Track worked reasonably well for the concrete test, Test 21, except for the inherently small sample size. Frag Track failed in the CMU test, Test 20, because the dust cloud from the mortar almost completely obscured the field of view.

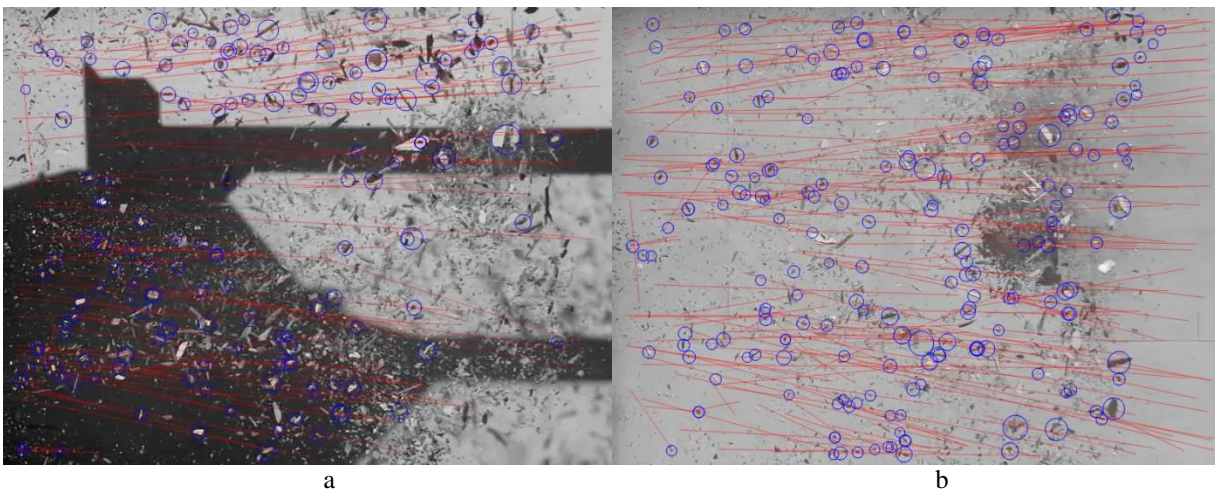


Figure 22. Frack Track applied to two glass tests. (a) Test 18, (b) Test 19.

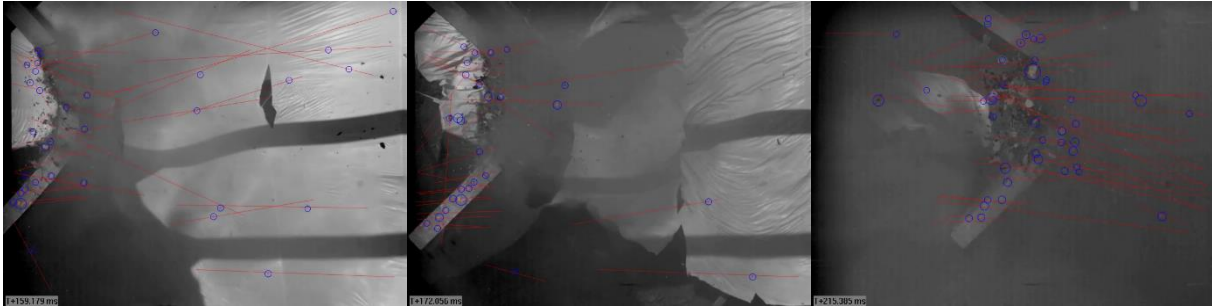


Figure 23. Frag Track applied to a reinforced concrete slab test (Test 21).

3.2.2 FRAG TRACK VELOCITY ANALYSIS VALIDATION USING KINOVEA

Kinovea was used to validate Frag Track’s velocity estimates. Kinovea operates on a semi-automated basis to develop path-trace plots for fragments tagged by the user. More so than Frag Track, dust obscuration can limit the effectiveness of the Kinovea analysis, particularly for late-time fragments Figure 24 shows Kinovea results for the concrete panel test (Test 21). In this example, Kinovea was used to track the movement of the intact portion of the concrete panel.



Figure 24. Kinovea applied to a reinforced concrete panel (Test 21).

3.3 ANALYSIS OF LATE-TIME PHYSICALLY-COLLECTED FRAGMENTS

As noted earlier, the CMU wall test, Test 20, generated large amounts of dust that completely obscured the high-speed video. Thus, for this test only, physical collection was used to characterize the debris size. Because of the large scale of the test, over 800,000 fragments were produced. Thus the new highly-efficient fragment characterization techniques introduced in Reference [1] were used. However, even with these efficient techniques, this one test still dominated the overall analysis effort. Figure 25 shows the fragments generated in Test 20, both as originally found and after using a series of increasingly finer sieves to sort them into size bins.



Figure 25. Fragments generated in Test 20: a) designated collection area immediately after testing; b) after using a series of increasingly finer sieves to sort fragments into size bins.

As seen in Figure 26, for each size bin, the fragments were staged for pictures by laying them out on a flat blue surface. These pictures were then analyzed using SigmaScan. For thin enough samples and large enough fragments, the fragments will inherit two smooth surfaces from the original samples. Then:

$$m_i = tA_i$$

where m_i is the mass of fragment i , A_i is the cross-sectional area of fragment i as measured by SigmaScan, and t is the original sample thickness, e.g., $t = 0.25$ for the plate glass in Tests 17, 18 and 19. For thicker samples and smaller fragments, the fragments will be rough on all sides, i.e., they will not inherit any smooth surfaces from the original sample. Then it is assumed that:

$$m_i \approx A_i \cdot \frac{\sum m_j}{\sum A_j}$$

where the sums refer to all of the fragments in a given size bin. In other words, the mass-to-area ratio of any individual fragment is assumed to be the same cumulative mass to cumulative area ratio of all fragments in the same bin.



Figure 26. Digital photographs of the fragments captured in Sieve no. 4 in Test 20 arrayed on a flat blue surface. The top shows the original full-color image. The bottom shows a high-contrast grey-scale image produced by SigmaScan.

A pass with MS Excel logic functions was used to exclude fragments smaller than some minimum fragment size M_{min} . In laying out the fragments from each sieve prior to photography, it was inevitable that a certain fraction of the fragments would end up touching or slightly overlapping each other. For sieves smaller than No. 4, a second pass with MS Excel logic functions was used to roughly correct for cases in which SigmaScan treated multiple adjacent small fragments as one fragment. This second pass was essentially a re-normalization. For No. 4 and larger-meshed sieves, for improved accuracy, lines were drawn by hand to force SigmaScan to treat adjacent fragments separately. For example, Figure 27 shows the final outcome for the case seen in Figure 26.

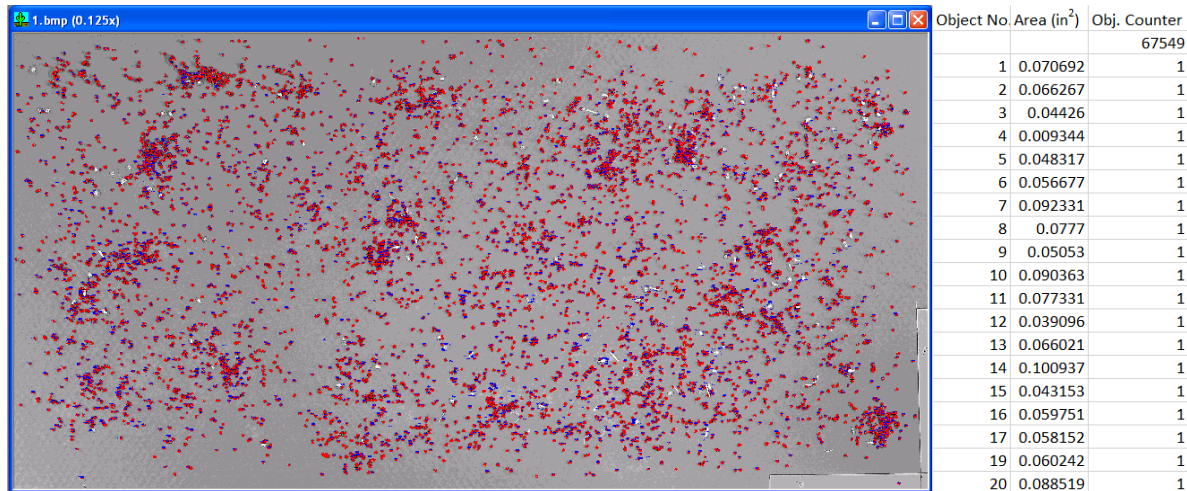


Figure 27. SigmaScan results for Sieve no. 4 in Test 20. Fragments were identified and measured in SigmaScan. The results were output to and post-processed in a MS Excel spreadsheet.

4 RESULTS

4.1 INTRODUCTION

Table 3 summarizes the measurements techniques used in this test series. The three glass tests (Tests 17, 18 and 19) produced an extremely large number of fragments. Thus these results are based entirely on high-speed video, which allows for rapid and relatively low-cost fragment characterization. The CMU wall test (Test 20) also produced an extremely large number of fragments. However, because dust from the CMU heavily obscured the high-speed video, these results are based entirely on physical collection. The concrete wall test (Test 21) produced only a small number of fragments. An attempt was made to characterize these fragments using side-view high-speed video, but this was ultimately unsuccessful due to the small sample size.

Table 3. Summary of measurement techniques.

	Mass			Velocity
	Rear-View HSV	Side-View HSV	Physical Collection	Side-View HSV
Test 17 ¹	✓			
Test 18 ¹	✓	✓		✓
Test 19 ¹	✓	✓		✓
Test 20 ²			✓	
Test 21 ³				

(1) In the glass tests, high-quality results were obtained from HSV. Thus no attempt was made to characterize the physically collected fragments.

(2) In the CMU test, high-speed video was obscured by dust. Thus only the physically-collected fragments were characterized.

(3) In the concrete test, while an attempt was made to analyze the side-view HSV, no results are reported due to the small number of fragments.

4.2 ANALYSIS AND DISTRIBUTION FIT APPROACH

Fragment size distributions are commonly described by cumulative distribution functions (CDFs) and probability density functions (PDFs). The *cumulative distribution function* $F(M)$ is the number fraction of fragments with masses greater than or equal to M . Similarly, the *probability density function* $f(M)$ is the number fraction of fragments with masses in a range dM centered on

M divided by dM . Notice that $F(x)$ is monotone decreasing such that $F(0) = 1$ and $F(\infty) = 0$. In addition, notice that $f(x)$ is always non-negative such that:

$$\int_0^{\infty} f(x)dx = 1.$$

Finally notice that:

$$F(M) = -\int_M^{\infty} f(x)dx; \quad f(M) = -\frac{dF}{dM}$$

This assumes an infinite range of fragment sizes. The CDFs and PDFs over the limited range $M_{\min} \leq M \leq M_{\max}$ are related to the CDFs and PDFs over an infinite range as follows:

$$\tilde{F}(M) = \frac{F(x) - F(M_{\min})}{F(M_{\max}) - F(M_{\min})}$$

$$\tilde{f}(M) = \frac{f(M)}{F(M_{\max}) - F(M_{\min})}$$

The *count mean mass* is defined as follows:

$$M_{avg} = \int_0^{\infty} Mf(M)dM$$

for an infinite range and:

$$\tilde{M}_{avg} = \int_{M_{\min}}^{M_{\max}} M\tilde{f}(M)dM = \frac{\int_{M_{\min}}^{M_{\max}} Mf(M)dM}{\int_{M_{\min}}^{M_{\max}} f(M)dM}$$

for a finite range. Notice that, for one-step fragmentation of unitary objects, conservation of mass, momentum, and energy yield expressions for M_{avg} as a function of strain rate, e.g., [3] [4]. However, this is obviously not the case for \tilde{M}_{avg} , which depends on the arbitrary values M_{\min} and M_{\max} . Normalizing by the count mean mass, *Weibull size distributions* may be defined as follows:

$$F(M) = \exp\left[-c\left(\frac{M}{M_{avg}}\right)^r\right]$$

$$f(M) = \frac{c|r|}{M_{avg}} \left(\frac{M}{M_{avg}} \right)^{r-1} \exp \left[-c \left(\frac{M}{M_{avg}} \right)^r \right]$$

where r is a free parameter and where:

$$c = \Gamma \left(1 + \frac{1}{r} \right)^r$$

As seen in Reference [5]:

$$r = \frac{n}{m}$$

where n is the exponent in the Weibull size distribution written in terms of fragment diameter and m is the fragment dimension, e.g., $m = 3$ for CMU and concrete and $m = 2$ for plate glass.

As before, the Weibull size distribution can be modified to account for a limited range. As a specific example, suppose that $r > 0$ and $M \leq M_{max} \ll M_{avg}$. As another specific example, suppose that $r < 0$ and $M \geq M_{min} \gg M_{avg}$. In either case, Weibull size distributions are approximately equal to *power law size distributions*:

$$F(M) = \begin{cases} 1 - (M / M_{max})^r & r > 0 \\ (M / M_{min})^r & r < 0 \end{cases}$$

$$f(M) = \begin{cases} \frac{r}{M_{max}} \left(\frac{M}{M_{max}} \right)^{r-1} & r > 0 \\ \frac{|r|}{M_{min}} \left(\frac{M}{M_{min}} \right)^{r-1} & r < 0 \end{cases}$$

Approximate values for r were obtained by curve fitting the experimental results. This is a surprisingly complex problem; see Reference [1] for more details.

4.3 MASS DISTRIBUTIONS FROM SIGMASCAN ANALYSIS OF REAR-VIEW HSV

This subsection describes the mass distributions obtained from an analysis of the early-time rear-view HSV using SigmaScan. As described earlier, results are limited to the three tests involving plate glass test objects, namely, Tests 17, 18 and 19. As seen in Figure 20, the results are based on a single quadrant in a single frame. Because the fragments were still evolving both in time and space, the results may be different in other quadrants and in other frames. In general, the parameter $|r|$ decreases over time until it reaches a final value. An attempt was made to choose a time after $|r|$ reached a stable value in at least one quadrant but before transverse motions led to fragments in the front blocking views of fragments in the rear.

Table 4 and Table 5 summarize the outcome of the SigmaScan size analysis of the rear-view HSV. More specifically, the first three rows of Table 5 show the best-fit Weibull parameters obtained for Tests 17, 18 and 19 individually; see also Figure 28, Figure 29 and Figure 30, respectively.¹ The last row of Table 5 shows the best-fit Weibull parameters for Tests 17, 18 and 19 combined; see also Figure 31. Notice that the binning scheme used in Method 2 retains a greater range of large and small fragments than the binning scheme used in Method 1. In either case, the fragment sizes span over four orders-of-magnitude, more than large enough to obtain reliable curve fits. In these tests, the differences between the Methods 1 and 2 are minor.

Table 4. Statistical parameters for rear-view HSV mass in Tests 17, 18, and 19 involving plate glass test objects.

Material	Test	Peak Overpressure (psi)	# Frags Observed	Mass Frags Observed (g)	% Original Quadrant Mass	% Original Sample Mass
Tempered Glass	17	Low (~10)	885	7,925	~89.6%	22.4%
	18	Low (~10)	712	6,701	~75.6%	18.9%
	19	High (~30)	1,782	6,588	~74.4%	18.6%

Table 5. Best-fit Weibull parameters based on rear-view HSV mass in Tests 17, 18, and 19 involving plate glass test objects.

Material	Test	Weibull Parameters Method 1 (July 2016)				Weibull Parameters Method 2 (Sept 2016)			
		r	M_{min} (g)	M_{max} (g)	\tilde{M}_{avg} (g)	r	M_{min} (g)	M_{max} (g)	\tilde{M}_{avg} (g)
Tempered Glass	17	0.49	0.01	200	7.07	0.52	0.003	200	8.95
	18	0.62	0.01	200	9.34	0.62	0.002	240	9.41
	19	0.57	0.01	200	3.74	0.57	0.003	151	3.70
	Combined	0.56				0.57			

Even though Tests 17 and 18 were essentially the same, they obtained substantially different size distributions. This is probably because the analysis was performed on a different quadrant and frame, i.e., different points in space and time. Because of this apparent sensitivity to time and space, it is hard to draw firm conclusions about the early-time fragment size distributions.

¹ In these and all subsequent figures, the label “Probability Density” on the vertical axis refers to the PDF *times the count mean mass*, i.e., it refers to $M_{avg}f(M)$.

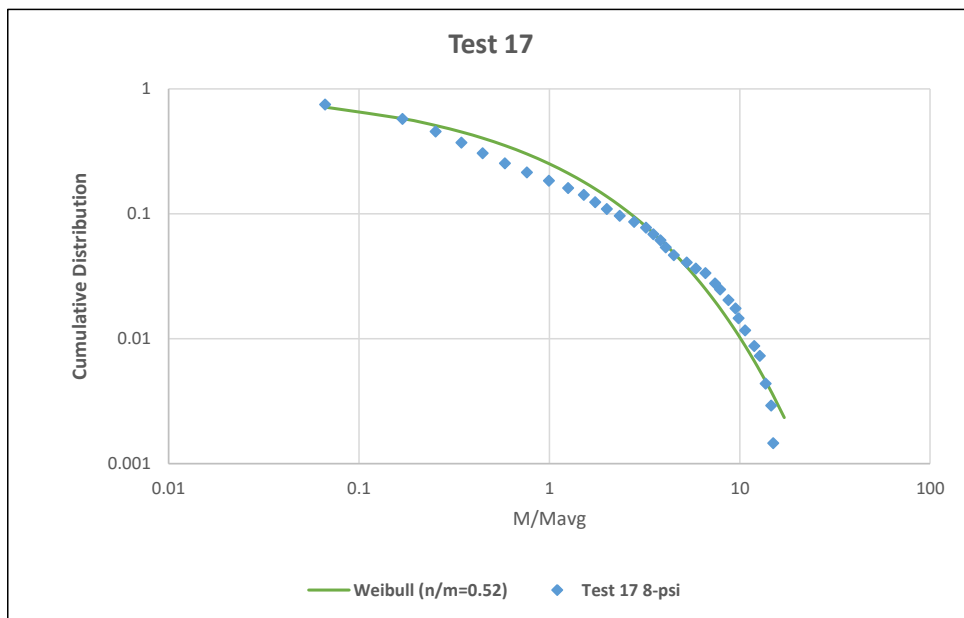
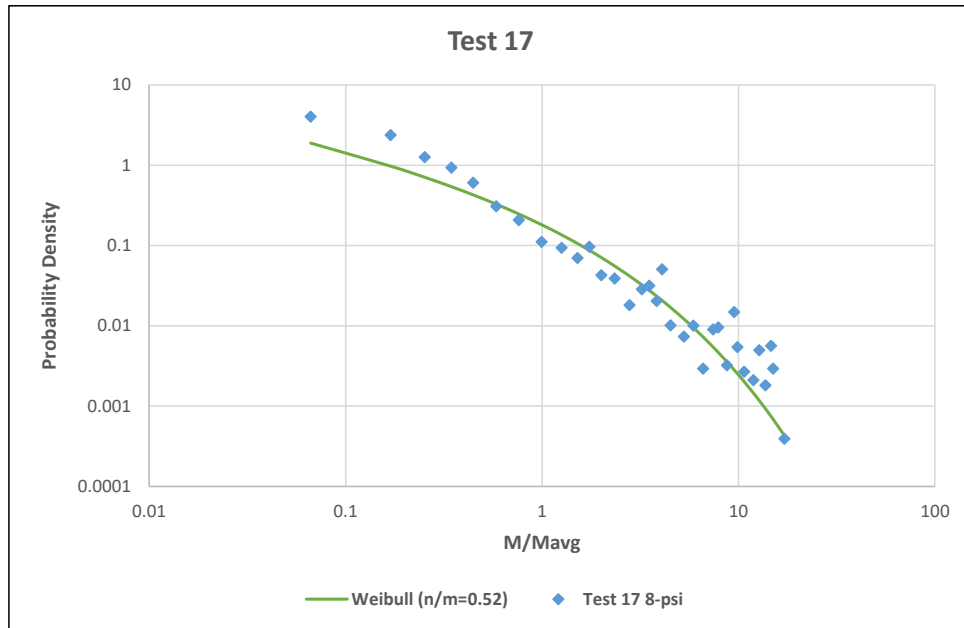


Figure 28. Best-fit Weibull mass distribution for rear-view HSV test data for PDF (top) and CDF (bottom) for Test 17 for tempered glass.

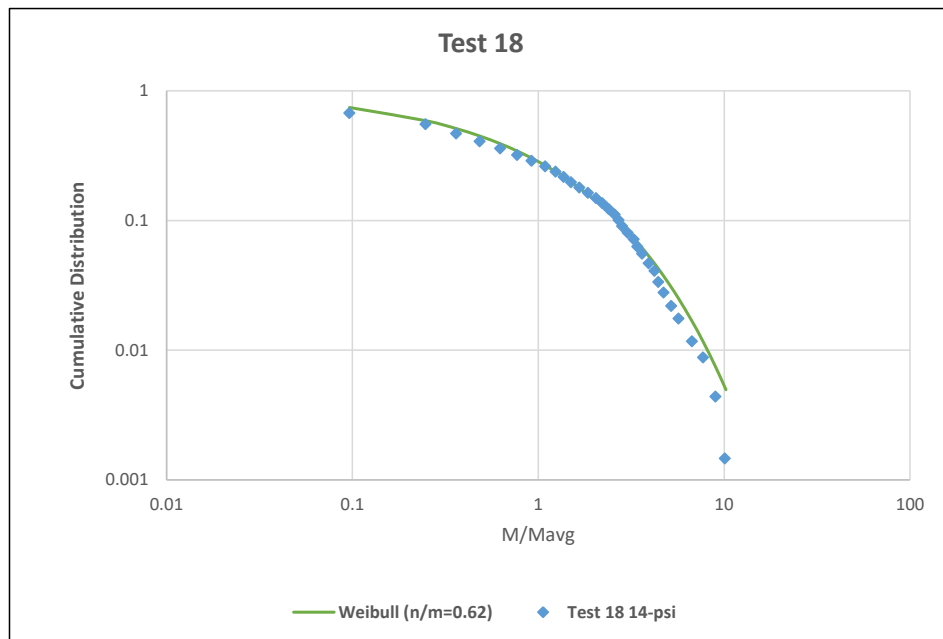
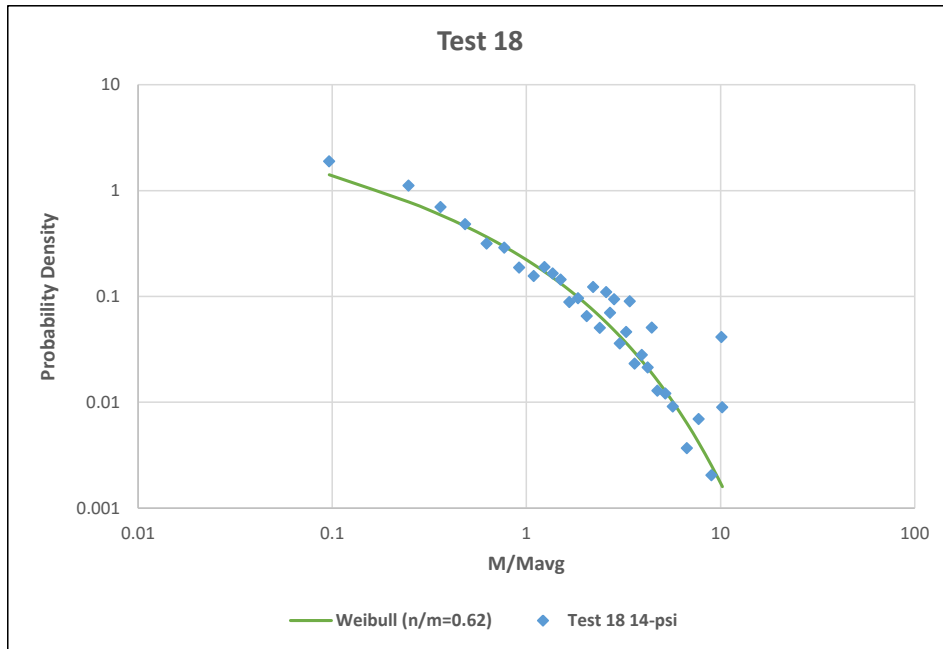


Figure 29. Best-fit Weibull mass distribution for rear-view HSV test data for PDF (top) and CDF (bottom) for Test 18 for tempered glass.

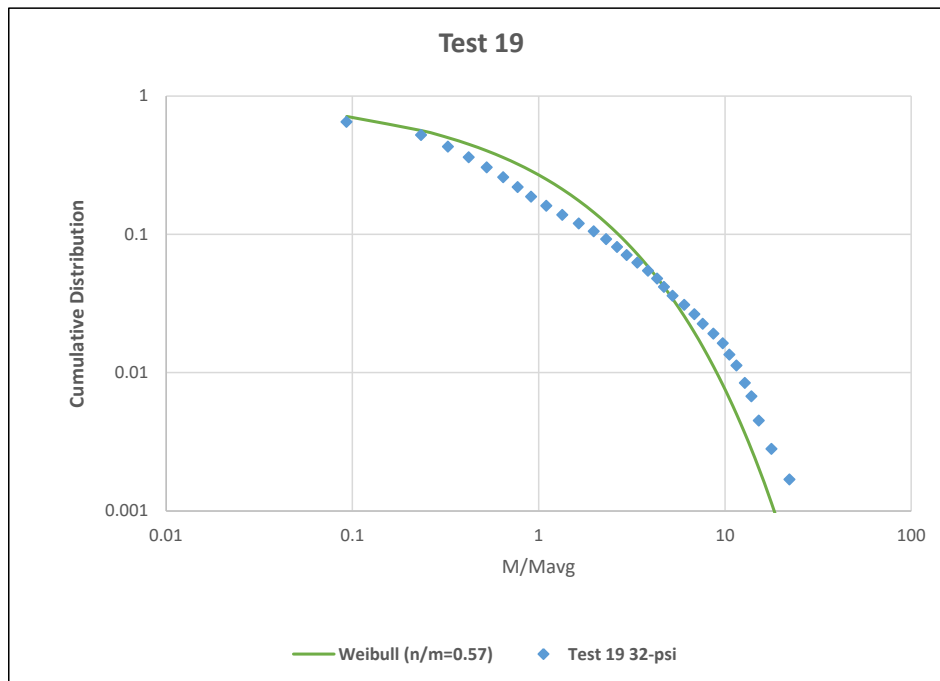
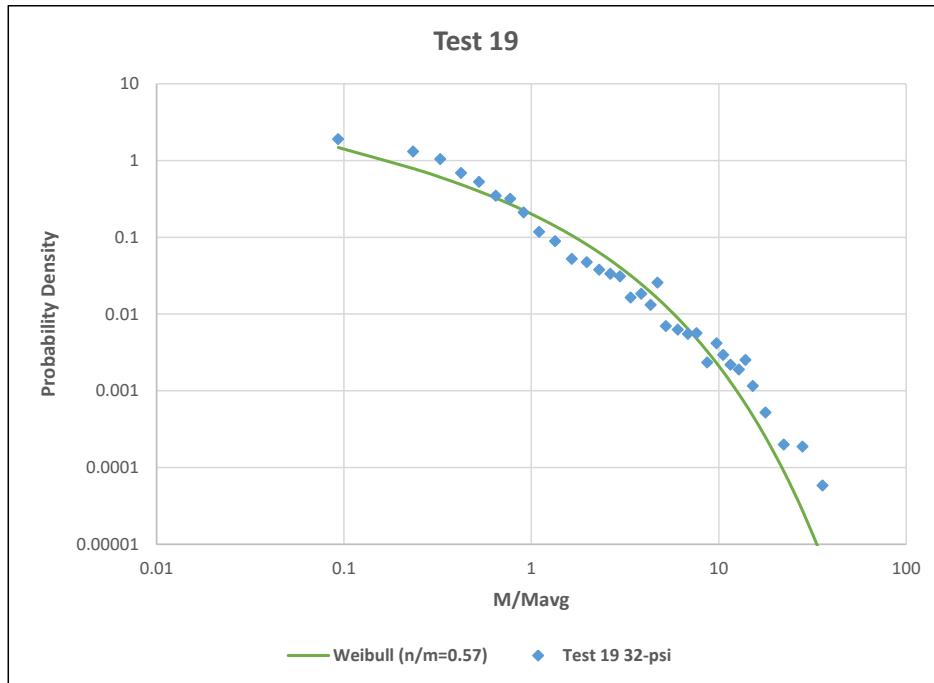


Figure 30. Best-fit Weibull mass distribution for rear-view HSV test data for PDF (top) and CDF (bottom) for Test 19 for tempered glass.

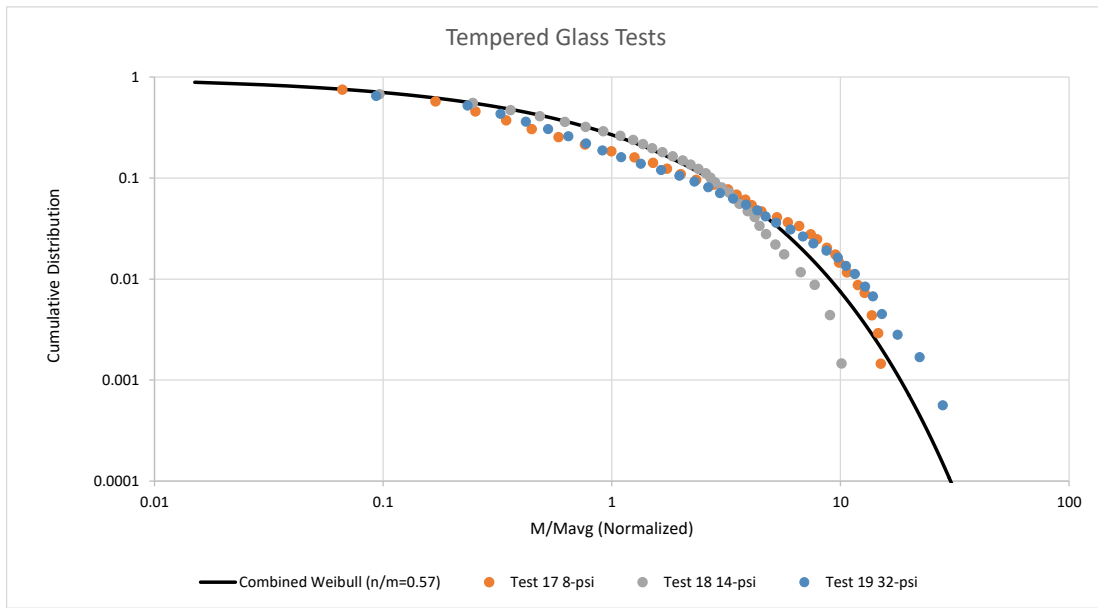
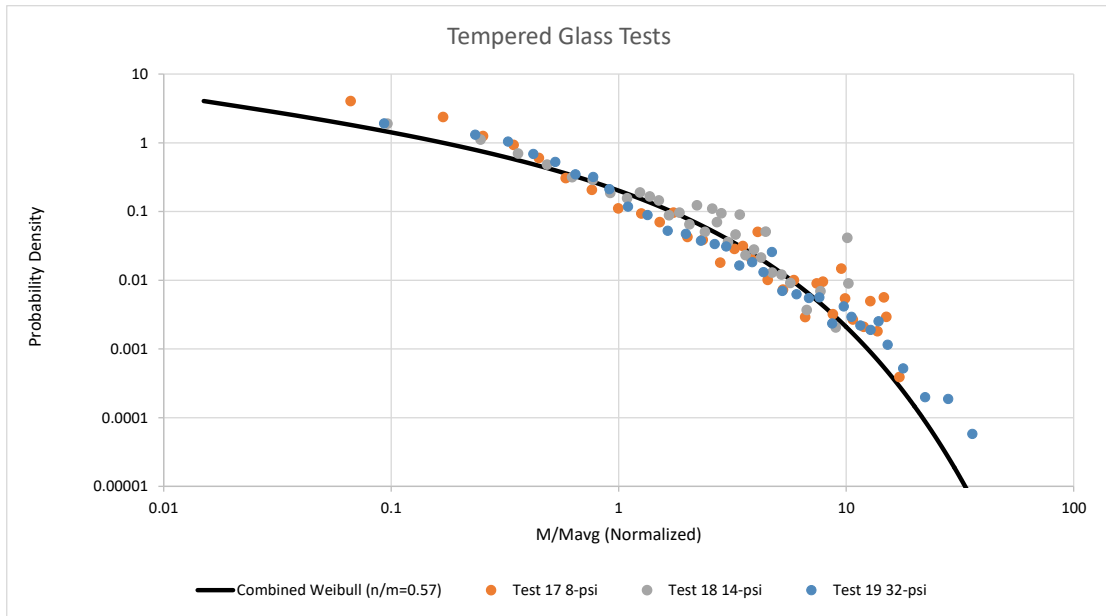


Figure 31. Best-fit Weibull mass distribution for rear-view HSV test data for PDF (top) and CDF (bottom) for Tests 17, 18 and 19 for tempered glass.

4.4 MASS AND VELOCITY DISTRIBUTIONS FROM SIDE-VIEW HSV ANALYSIS

This subsection describes the mass and velocity distributions obtained from an analysis of the mid-time side-view HSV using Frag Track. As described earlier, results are limited to two of the three tests involving plate glass test objects, namely, Tests 18 and 19. The side-view HSV for Test 17 was not analyzed due to a failure in the background material, which resulted in unreliable results.

Table 6 and Table 7 summarize the outcome of the Frag Track size analysis of the side-view HSV.

Table 6. Statistical parameters for side-view HSV mass in Tests 18 and 19 involving plate glass test objects.

Material	Test	Peak Overpressure (psi)	# Frags Observed	Mass Frags Observed (g) (*)	% Original Sample Mass (*)
Tempered Glass	18	Low (~10)	2,003	39,019	106%
	19	High (~30)	1,397	35,999	97.5%

(*) Significant overestimate due to large fragments that were much closer to the camera than assumed.

Table 7. Best-fit Weibull parameters based on side-view HSV mass in Tests 18 and 19 involving plate glass test objects.

Material	Test	Weibull Parameters Method 1 (July 2016)				Weibull Parameters Method 2 (Sept 2016)			
		r	M_{min} (g)	M_{max} (g)	\tilde{M}_{avg} (g)	r	M_{min} (g)	M_{max} (g)	\tilde{M}_{avg} (g)
Tempered Glass	18	0.53	0.1	200	12.62	0.44	0.01	1,114	19.48
	19	0.73	0.1	200	15.55	0.49	0.06	1,300	21.30
	Combined	0.63				0.47			

The last two columns in Table 6 have large errors. As noted earlier, for analysis purposes, it was necessary to assume that the fragments were traveling in a single plane at a fixed distance from the side-view HSV camera. This meant that fragments located closer to the side-view HSV camera than the assumed plane appeared to be larger than they actually were and, conversely, fragments located farther from the side-view HSV camera than the assumed plane appeared to be smaller than they actually were. In practice, the former effect dominated the latter – a relatively small number of large fragments traveling near the camera heavily distorted the observed mass. More specifically, in Test 18, the 18 largest fragments (those that appeared to be greater than 300g) accounted for about 25% of the observed mass and the 36 largest fragments (those that appeared to be greater than 200g) accounted for almost 40% of the observed mass. Except for imposing a maximum fragment size to eliminate the worst of the distortion, no attempt was made to correct for this effect. This makes it hard to draw firm conclusions about the mid-time fragment size distributions.

The first two rows of Table 7 show the best-fit Weibull parameters obtained for Tests 18 and 19 individually; see also Figure 32 and Figure 33, respectively.² The last row of Table 7 shows the best-fit Weibull parameters for Tests 18 and 19 combined; see also Figure 34. Notice that the binning scheme used in Method 2 retains a greater range of fragments than the binning scheme used in Method 1. In Method 2, the fragment sizes span 4 to 5 orders of magnitude, more than large enough to obtain reliable curve fits. However, in Method 1, the fragment sizes span only about 3 orders of magnitude, which adversely affects the fitting accuracy. Even though Method 1 has a lower cap on fragment size, and thus avoids more of the exaggerated large fragments, it is believed that Method 2 obtained somewhat better results than Method 1.

² In these and all subsequent figures, the label “Probability Density” on the vertical axis refers to the PDF *times the count mean mass*, i.e., it refers to $M_{avg}f(M)$.

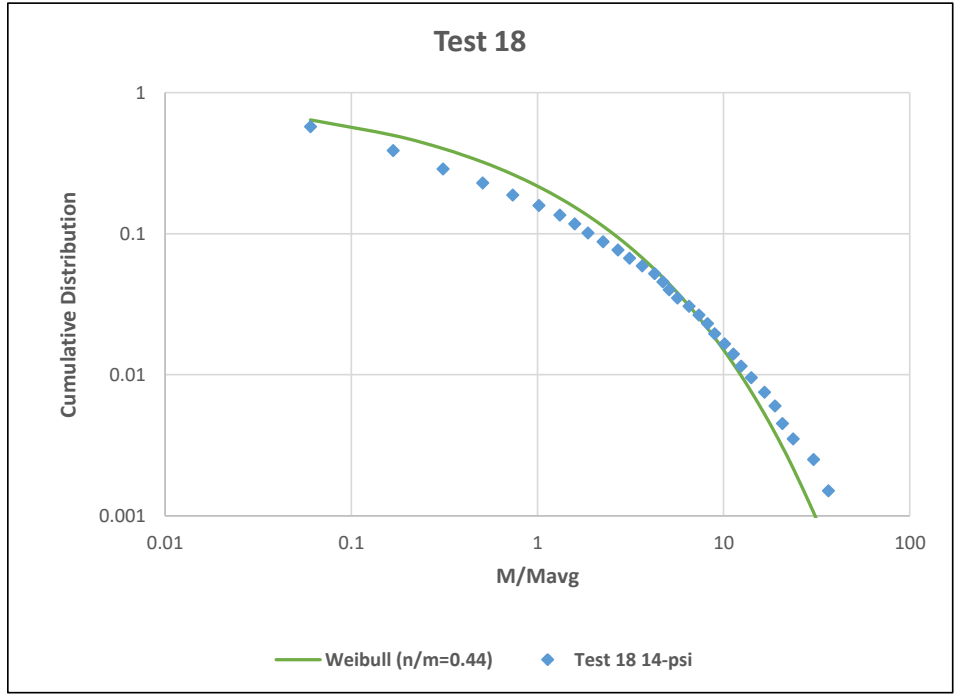
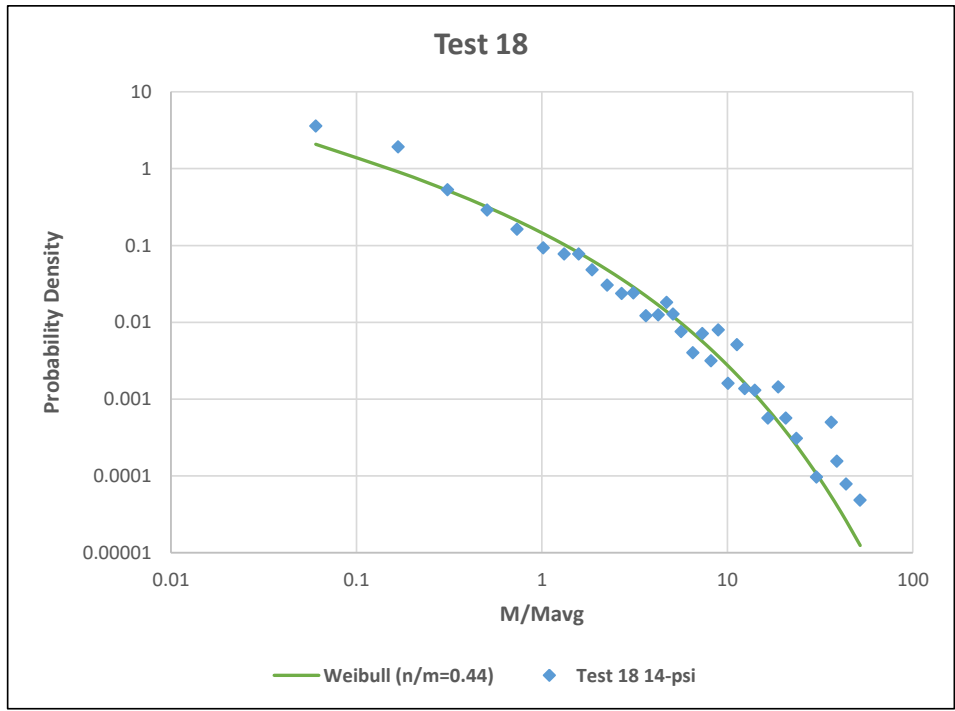


Figure 32. Best-fit Weibull mass distribution for side-view HSV test data for PDF (top) and CDF (bottom) for Test 18 involving tempered glass.

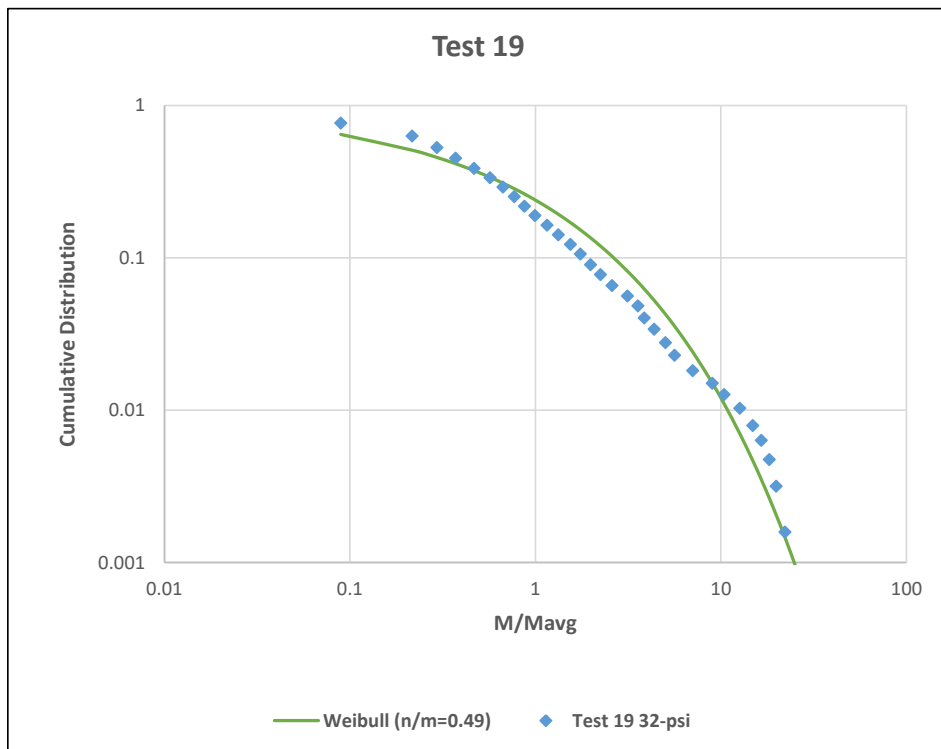
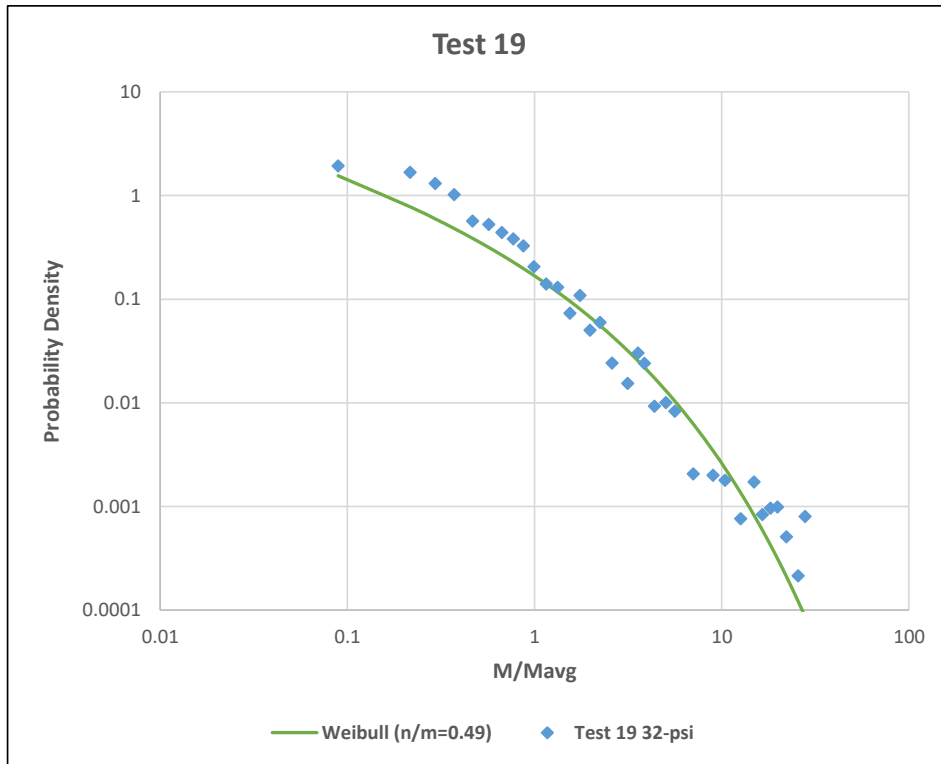


Figure 33. Best-fit Weibull mass distribution for side-view HSV test data for PDF (top) and CDF (bottom) for Test 19 involving tempered glass.

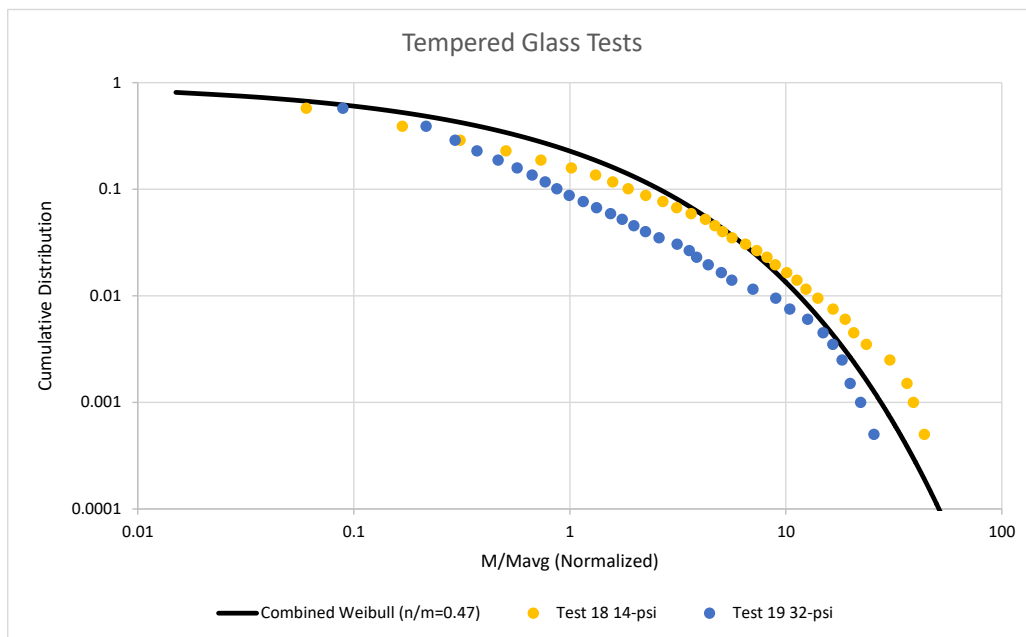
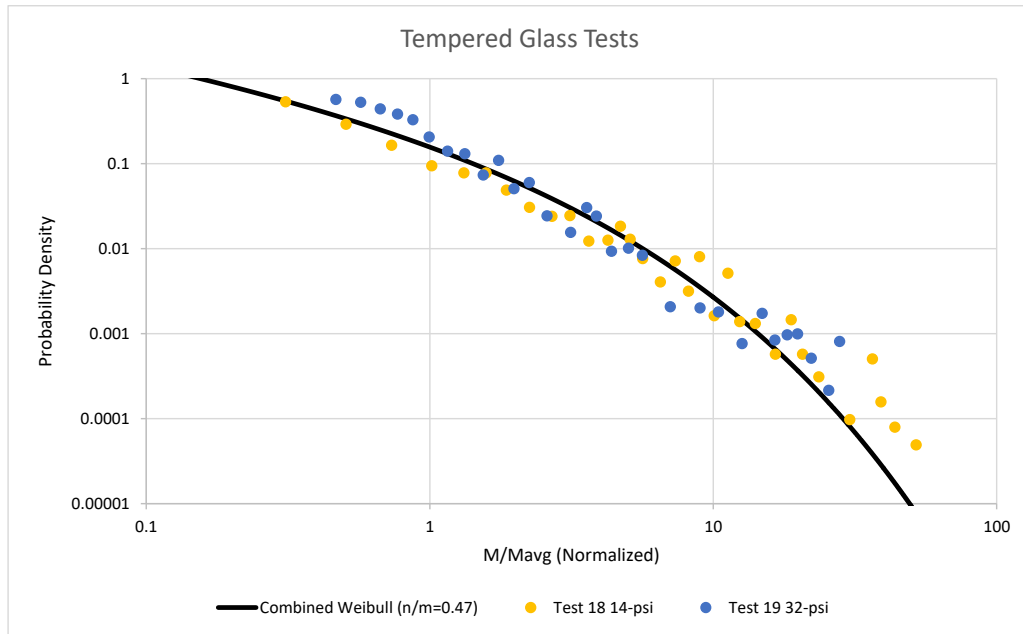


Figure 34. Best-fit Weibull mass distribution for side-view HSV test data for PDF (top) and CDF (bottom) for Tests 18 and 19 involving tempered glass.

Comparing the results of Table 5 and Table 7 indicates that r is generally somewhat smaller at mid-times than at early-times. In other words, the fragment size spread tends to increase with time. A similar trend was observed in the first test series [1]. As seen in Figure 35, the glass fragments are subject to mid-air collisions. If sufficiently energetic, such collisions cause the one or both of the participating glass fragments to shatter into smaller pieces, thus increasing the overall size spread.

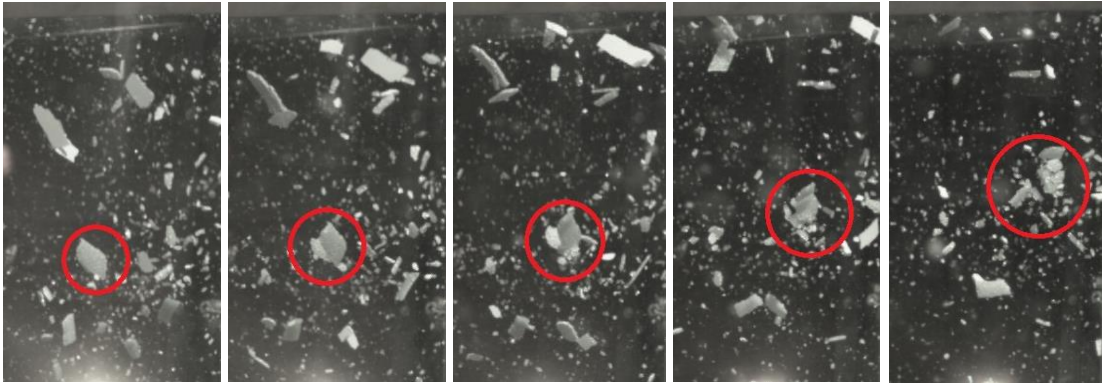


Figure 35. Glass fragments experience mid-air collisions leading to breakup in Test 17.

Table 8 summarizes the outcome of the Frag Track velocity analysis of the side-view HSV. More specifically, the first two rows of Table 8 show the best-fit Weibull parameters obtained for Tests 18 and 19 individually; see also Figure 36 and Figure 37, respectively. The last row of Table 8 shows the best-fit Weibull parameters for Tests 18 and 19 combined; see also Figure 38. Unlike mass, there is no known theoretical foundation for using Weibull distributions for velocity. Weibull distributions were used here for expediency, for consistency with the mass fits, and because they seemed to provide reasonable empirical fits. As with fragment mass, fragment velocity is subject to heavy distortion due to fragments traveling toward or away from the camera.

Table 8. Best-fit Weibull parameters based on side-view HSV velocity in Tests 18 and 19 involving plate glass test objects.

Material	Test	Weibull Parameters Method 1 (July 2016)			
		r	V_{min} (m/s)	V_{max} (m/s)	V_{avg} (m/s)
Tempered Glass	18	1.93	0	1,000	51.03
	19	2.30	0	1,000	73.85
	Combined	2.12			

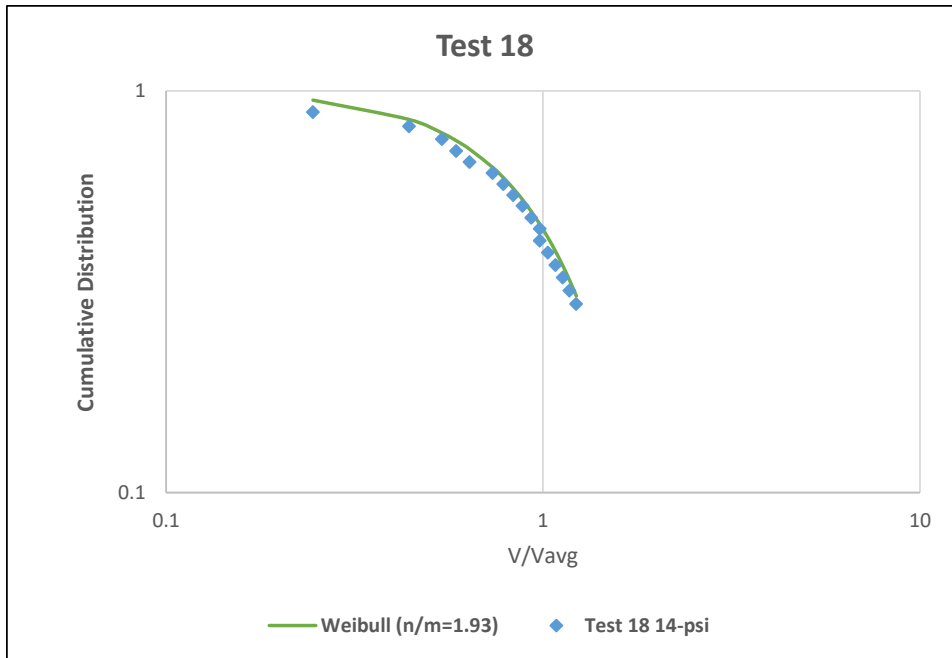


Figure 36. Best-fit Weibull velocity distribution for rear-view HSV test data for CDF for Test 18 involving tempered glass.

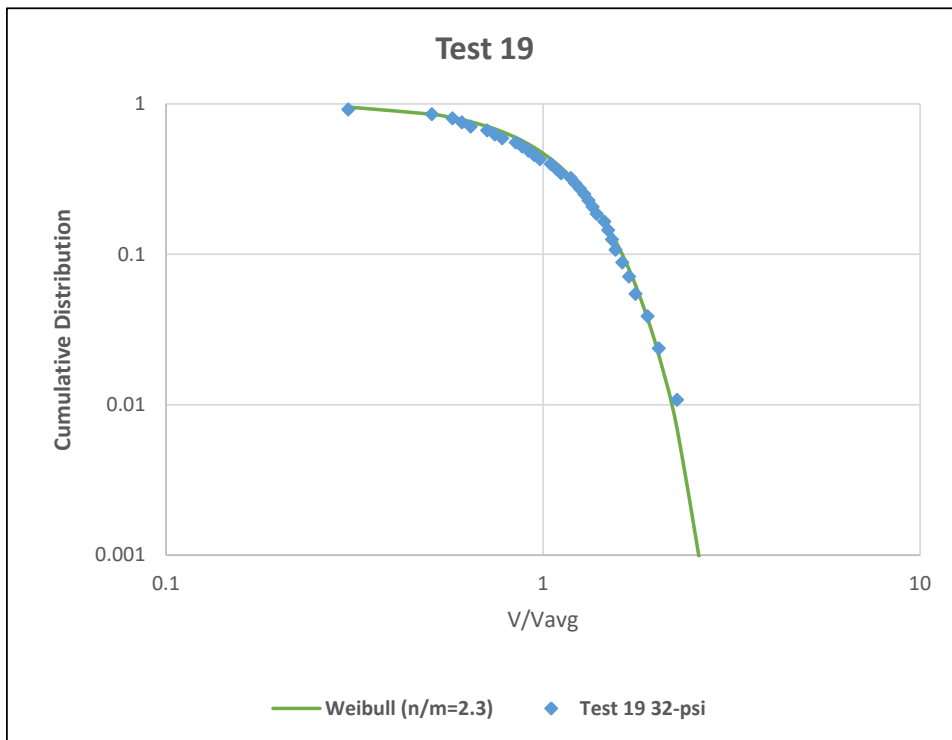


Figure 37. Best-fit Weibull velocity distribution for rear-view HSV test data for CDF for Test 19 involving tempered glass.

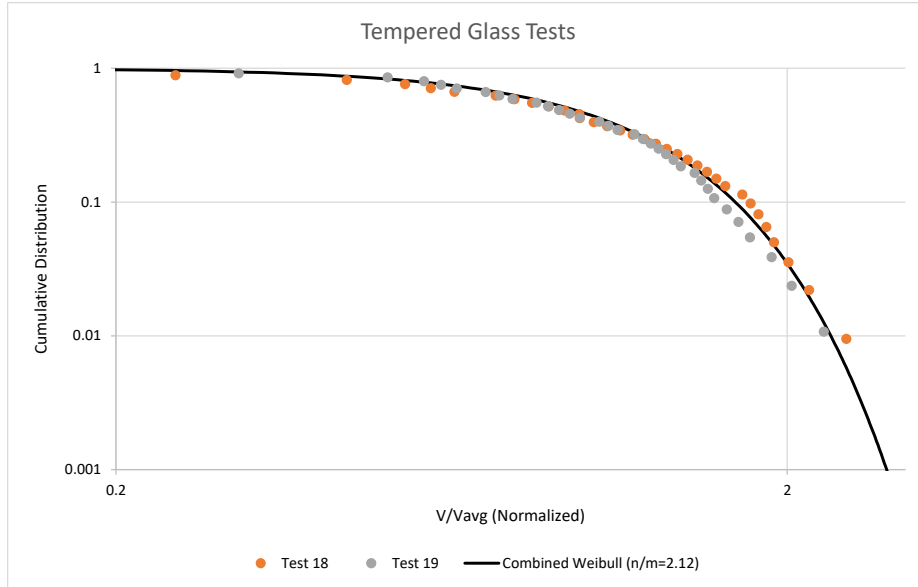


Figure 38. Best-fit Weibull velocity distribution for side-view HSV test data CDF for Tests 18 and 19 involving tempered glass.

4.5 MASS DISTRIBUTIONS FROM PHYSICAL COLLECTION ANALYSIS

This subsection describes the mass distributions obtained from late-time physically-collected fragments. Physical collection tends to be more accurate than optical techniques based on high-speed video. Thus, the earlier small-scale test series used physical collection routinely [1]. However, for this large-scale tests series, physical collection was extremely costly and difficult due to the large number of fragments produced. Thus it was used only in Test 20, where dust generated by the failing CMU wall heavily obscured the high-speed video.

Table 9 and Table 10 summarize the outcome of the physical collection; see also Figure 39.

Table 9. Statistical parameters for physical collection in Test 20 with a CMU wall.

Material	Test	Peak Overpressure (psi)	# Frags Observed	Mass Frags Observed (g)	% Original Sample Mass
CMU	20	High (~75)	811,283	993,725.7	80.5%

Table 10. Best-fit negative Weibull (i.e. power law) parameter based on physical collection in Test 20 with a CMU wall.

Material	Test	Weibull Parameters Method 1 (July 2016)				Weibull Parameters Method 2 (Sept 2016)			
		r	M_{min} (g)	M_{max} (g)	\bar{M}_{avg} (g)	r	M_{min} (g)	M_{max} (g)	\bar{M}_{avg} (g)
CMU	20	-1.00	0.2	7	0.16	-1.02	0.01	1,500	0.610

In Table 9, the fragment masses range between 0.011g and 53,073.31g (117 lb) with an average of 1.22g. The largest fragment consisted of several blocks in the reinforcement column with the rebar and grout still intact. In Table 10, notice that the binning scheme used in Method 2 retains a

greater range of large and small fragments than the binning scheme used in Method 1. In Method 2, the fragment sizes span over 5 orders of magnitude. By contrast, in Method 1, the fragment sizes span only about 1.5 orders of magnitude. More specifically, in Method 1, imposing the lower size limit reduced the fragment number by about 90% to 81,089 and imposing the upper size limit reduced the fragment mass by about 95% to 51,042g. Because the best fit was obtained by a negative Weibull distribution (i.e., a power law) rather than a positive Weibull distribution, the exact range was not critical; Methods 1 and 2 obtained almost the same result.

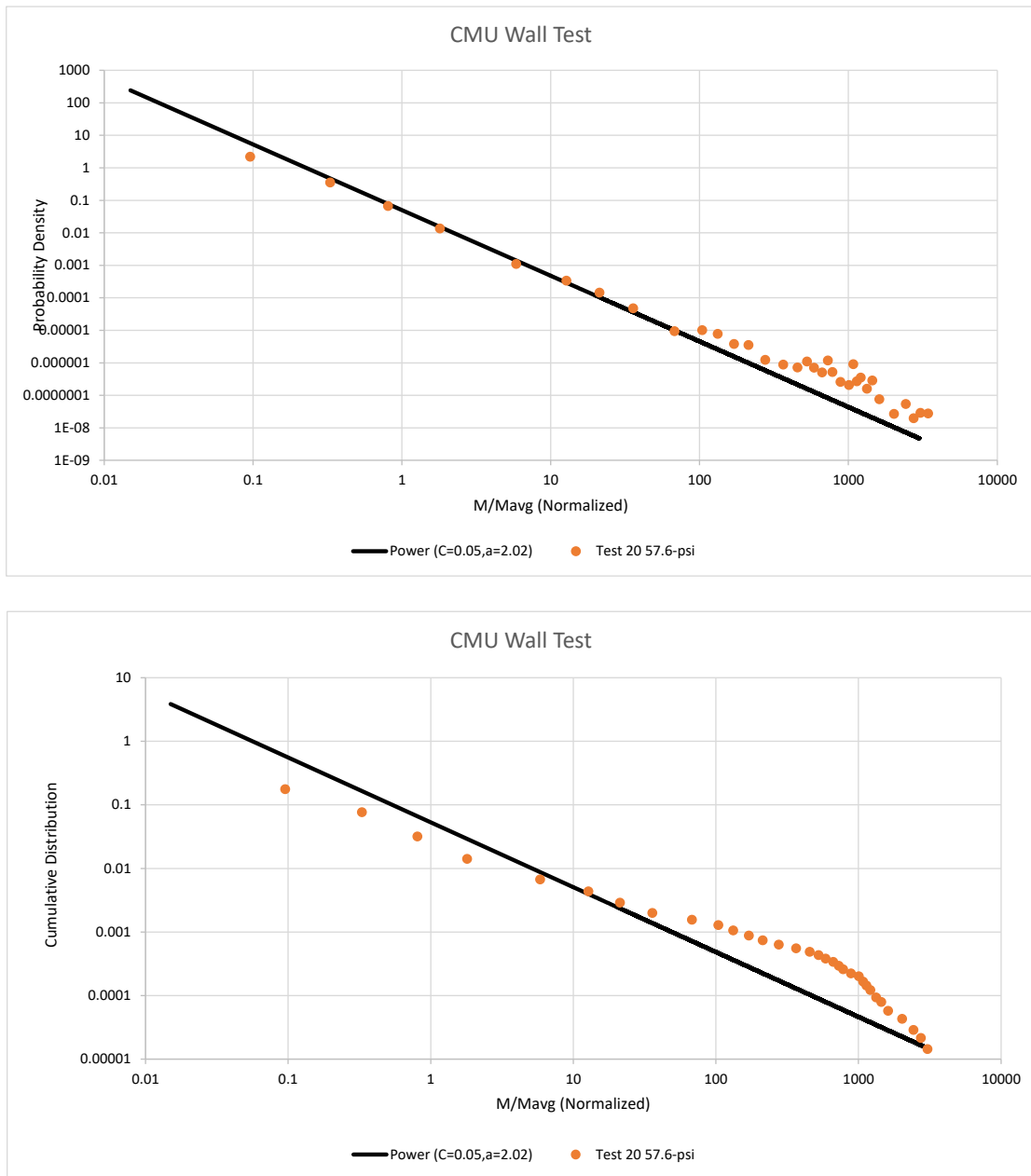


Figure 39. Best-fit power law mass distribution for physically-collected test data for PDF (top) and CDF (bottom) for Test 20 involving CMU.

5 CONCLUSIONS

Table 11 compares the results of the earlier small-scale test series [1] with those of the current large-scale test series.

Table 11. Summary of best-fit Weibull and power law size distributions.

Material	Scale	Test(s)	Weibull Parameter r		
			Early-Time (Rear-View HSV)	Mid-Time (Side-View HSV)	Late-Time (Physical Collection)
Glass	Small [1]	13, 15, 16	0.69 (0.64 – 1.06)	(*)	0.66 (0.50 – 0.69)
	Full	17, 18, 19	0.57 (0.49 – 0.62)	0.47 (***) (0.44 – 0.49)	(**)
CMU	Small [1]	3, 4, 7, 10, 12	(**)	(*)	0.64 (0.5 to 0.76)
	Full	20	(**)	(**)	–1.0
Concrete	Small [1]	5, 6, 8, 9	(**)	(*)	0.63 (0.46 to 0.66)
	Full	21	(**)	(*)	(**)

(*) Measurements were attempted but were not successful.

(**) No measurements were attempted.

(***) Measurements were distorted by the techniques employed.

In the earlier small-scale test series, the pressures were high enough to completely overwhelm the sample strengths. Consequently, all of the tests produced about the same result, to within the accuracy of the measurement and analysis techniques employed. More specifically, they all obtained a positive Weibull size distribution with $r \approx 2/3 \pm 1/6$, regardless of the exact test object, impulse and peak static overpressure. Notice that the Weibull exponent $r = 2/3$ is commonly-observed in fragmentation events; see, e.g., [4].

In this test series, the pressures were *not* high enough to overwhelm sample strength. Consequently, the results varied markedly from test to test. More specifically, the glass test objects obtained somewhat smaller r values than before. While the results are somewhat uncertain, it seems likely that $r \approx 0.57$ at early times and $r \approx 1/2$ after that. Notice that the Weibull exponent $r = 1/2$ is commonly-observed in fragmentation events; see, e.g., [4].

In addition, at late times, the CMU wall obtained a negative Weibull distribution with $r \approx -1$ or, equivalently, a power law with a mass exponent of -2 . Unlike the other results obtained in this test series, this result is highly accurate due to the measurement technique used and the extremely large sample size. Notice that the Weibull exponent $r = -1$ is commonly-observed in fragmentation events; see, e.g., [4]. The reinforced concrete wall cracked and folded, but did not truly fragment.

As in the earlier test series [1], an attempt was made to measure the fragment size distributions as three different times, to determine how the results changed. While fewer than 40% of these attempts produced useable results, there was still enough data to conclude that $|r|$ decreases over time, at least for glass, meaning that the size distribution becomes increasingly less uniform. This occurs because fragments break up due to the following: the delayed effects of pressure loading; mid-air collisions; and collisions with the fragment collection device.

The rear-view HSV obtained high-quality results in both test series with two caveats. First, it only works for thin test articles such as plate glass. For thick test object, many of the fragments form in the interior of the test object, out of view of the camera. Second, the results may vary significantly depending on the exact frame, and the exact region of the frame, chosen for analysis. The spatial variations (i.e., differences within a given frame) were more prominent for the large samples studied in this test series than for the small samples studied in the previous tests series [1].

The side-view HSV obtained unacceptable results in the earlier test series [1]. The side-view HSV results obtained better results in this test series due to the following factors:

- (i.) This test series eliminated the fragment stripper used in the earlier test series, which increased the number of observed fragments and the fragment size spread.
- (ii.) This test series used improved experimental techniques to reduce obscuration due to smoke and fire which, again, increased the number of observed fragments
- (iii) Most importantly, the lower overpressures used in this test series resulted in larger, more-easily visible fragments than the higher overpressures used in the first test series.

Eliminating the fragment stripper had mixed results. While it significantly increased the sample size, it also introduced distortions due to fragments traveling outside of the assumed fiduciary plane. These distortions were so severe that the estimated mass in Test 18 exceeded the mass of the original test object. No analysis has been done to estimate how much these distortions affected the as-measured fragment size distribution.

Physical collection is the ‘gold standard’ for determining fragment size distributions, with the caveat that glass fragments, in particular, are subject to unknown amounts of secondary breakup due to collisions with the fragment collection device. However, because physical collection is extremely time consuming and expensive for full-scale samples, it was only attempted in Test 20 involving a CMU wall, where dust obscured the high-speed video.

6 REFERENCES

- [1] B. Bewick, G. Rolater, J. Bui, M. Barsotti, M. Sanai, A. Ziemba and C. Laney, "Fragmentation of Solid Materials Using Shock Tubes. Part 1: First Test Series in a Small-Diameter Shock Tube," DTRA-TR-17-21, 2017.
- [2] M. Sanai, H. I. Lindberg and J. D. Colton, "Simulation of Blast Waves with Tailored Explosive Charges," *Journal of Fluid Mechanics*, vol. 158, pp. 137-152, 1984.
- [3] D. E. Grady and M. E. Kipp, "Mechanisms of Dynamic Fragmentation: Factors Governing Fragment Size," *Mechanics of Materials*, vol. 4, pp. 311-320, 1985.
- [4] C. B. Laney, "Effects of Mixtures on Liquid and Solid Fragment Size Distributions," DTRA-TR-16-52, May 2016.
- [5] C. B. Laney, "Transformation and Self-Similarity Properties of Gamma and Weibull Fragment Size Distributions," DTRA-TR-16-6, 2016.

APPENDIX A: LS-DYNA RESULTS FOR TEST PLANNING AND DESIGN

A.1. LS-DYNA RESULTS FOR CONCRETE SLABS

Pre-test LS-DYNA simulations were done to determine what type of concrete samples would make good candidates for testing. Three configurations for precast concrete panels were considered:

1. 5-½" (15-cm) solid panel with a single matte layer of #5 rebar @ 18" (45.7-cm) on-center (O.C.) each direction (longitudinal and transverse) – simply supported
2. 5-½" (15-cm) solid panel with a single matte layer of #5 rebar @ 18" (45.7-cm) on-center (O.C.) each direction (longitudinal and transverse) – fixed-fixed boundary condition
3. 4" (10-cm) solid panel with a welded-wire reinforcement (WWR) layer, 4x4x6, and a single #3 rebar around the perimeter of the panel

The first configuration represents a typical one-story panel or load-bearing wall, where sandwich panels were omitted to reduce the variability introduced by the insulation layer. The second configuration represents a panel that spans multiple stories with intermediate slab connections. The catenary action of a panel spanning over an intermediate slab creates a condition that is closer to the fixed-fixed boundary condition. The third configuration represents a non-load-bearing architectural panel. For architectural panels, a small WWR matte is included to account for temperature requirements and a single #3 rebar is run around the perimeter to stiffen the panel for lifting loads. Architectural panels are no thinner than 4" due to reinforcement cover requirements.

LS-DYNA was used to model these three configurations. The loading was assumed to be triangular with a constant decreasing slope from the peak pressure. The large diameter shock tube used in this effort can produce loadings that range from a 5-psi (34.4-kPa) peak with a 150-msec duration to a 100-psi (68.9-kPa) peak with a duration of 75-msec. In LS-DYNA, a load of 50-psi (34.4-kPa) with a 100-msec duration was applied. In addition, a *MAT_72R3 concrete model was used specifying a concrete strength of 5,000-psi. Rebar was modeled using an elastic-plastic kinematic model. An erosion criterion for the concrete material was applied. This was not intended to predict the actual fragmentation. Rather, it was intended to bound the types of structural level response that might be expected. The load bounds of the shock tube are well below the compressive strength of the concrete, i.e., well below 5,000-psi (34.5-MPa). The objective was to look at possible configurations that would produce debris with enough kinetic energy to cause collateral damage to surrounding buildings.

For the simply supported 5-½" (15-cm) panel, a 5-½" (15-cm) rigid plate was placed at the top and the bottom to represent a bearing surface that supports the panel from lateral motion. Figure 40 shows the initial condition and the predicted dynamic response of the panel after 50-msec. The panel is overloaded; it has a structural shear-induced failure. The shear strength near the supports is overwhelmed early on while the majority of the vertical cross section moves inward intact. At 50-msec, the top and bottom have deflected downward enough to allow the panel to begin moving inward freely. The rigid body motion of the panel is 100-fps (30.5-m/s). Depending on the height of the building that the panel is failing from, the translating panel could cause damage to structures across the street.

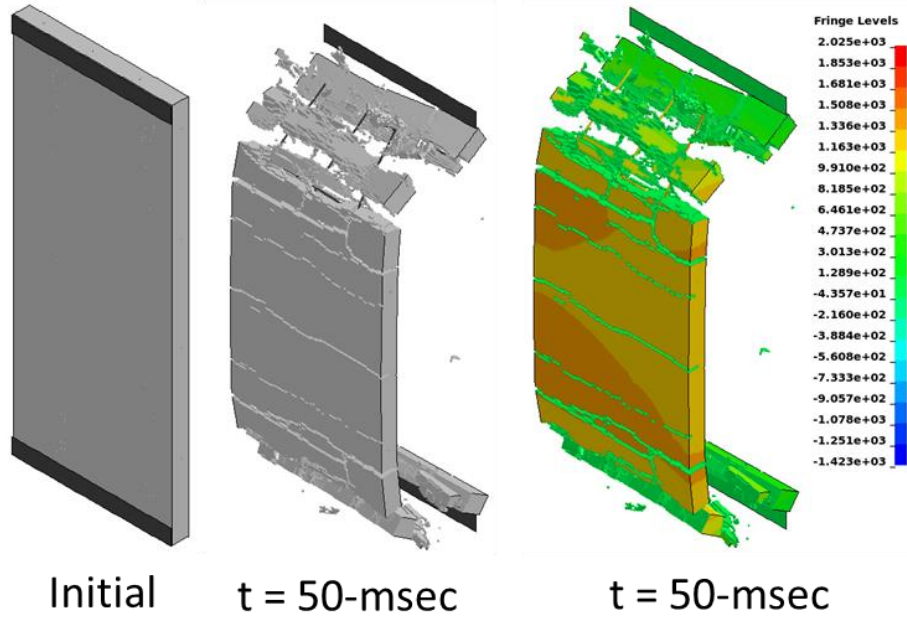


Figure 40. Response of 5-1/2"-thick simply-supported solid concrete panel ($p=50\text{-psi}$, $t=100\text{-msec}$) predicted by LS-DYNA.

The fixed condition 5-1/2" (15-cm) panel was simulated by extending the rebar to the edge of the panel and then using single point constraints (SPC) boundary conditions to represent a fully fixed boundary condition. Figure 41 shows the initial condition and the predicted dynamic response of the panel after 70-msec. When a fixed boundary condition is imposed, the rebar is stronger than the concrete. The net result is that debris is formed whose size is on the order of the spacing between the rebar and becomes smaller towards the midspan. The average debris velocity is about 100-fps (30.5-m/s) just as before.

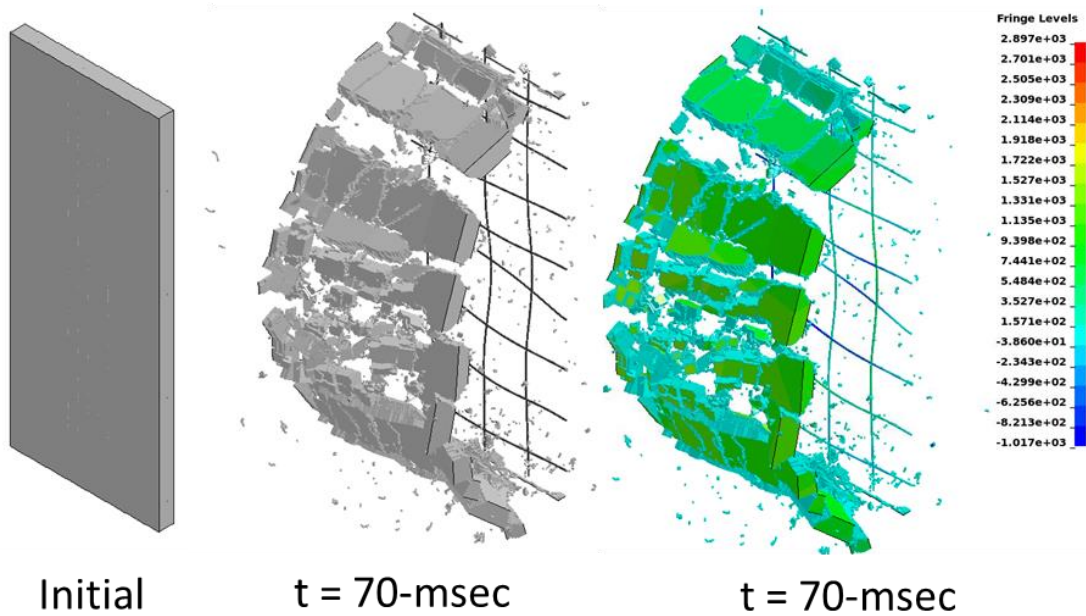


Figure 41. Response of 5-1/2"-thick, fixed-fixed solid concrete panel ($p=50\text{-psi}$, $t=100\text{-msec}$) as predicted by LS-DYNA.

Figure 42 shows the initial condition and the dynamic response of the 4"-thick architectural panel after 70-msec. The thinner architectural panel had a similar response to the simply supported 5-1/2" (15-cm) solid panel, e.g., they are both weak at the connections. The WWR mesh is enough to hold the bulk of the panel together and create a single flying panel. The displacement velocity is much higher at 233-fps (71-m/s), but the debris is larger and of little significance.

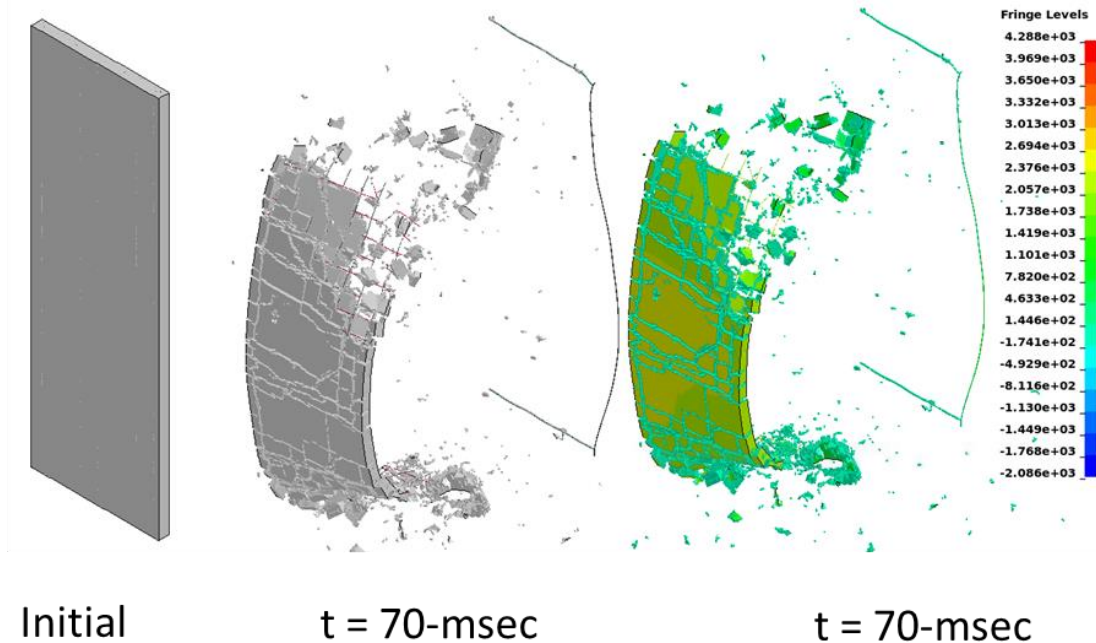


Figure 42. Response of 4" architectural precast panel ($p=50\text{-psi}$, $t=100\text{-msec}$) as predicted by LS-DYNA.

The results from these preliminary LS-DYNA analyses suggested that the 5-1/2" (15-cm) solid panel with a simple-simple configuration was the best choice for this test series.

A.2. LS-DYNA RESULTS FOR CMU WALLS

Pre-test LS-DYNA simulations were done to determine what type of CMU wall samples would make good candidates for testing. As with the concrete simulations given in Section A.1, the CMU wall simulations had a 50-psi (34.4-kPa) load which linearly decreased to zero over a duration of 100-msec. Two simulations were performed: an ungrouted CMU wall and a partially grouted CMU wall.

The ungrouted CMU wall experienced little breakup in the simulations. Rather, the CMU blocks remained mainly intact and experienced only bulk displacement.

The partially-grouted CMU wall represents a standard design with minimal reinforcement. The National Concrete Masonry Association (NCMA) allows for spacings of up to 54" (1.37-m) in 8" (0.2-m) block unit CMU walls. The simulation was completed using a 48" (1.22-m) spacing between grouted, reinforced columns. Figure 43 shows LS-DYNA results for breakup of the partially-grouted masonry wall subjected to a 50-psi (34.4-kPa) long-duration blast load. As before, the simulation is not intended to predict fragmentation; however, it does provide a general sense of the response. In particular, the LS-DYNA results show that a partially grouted, minimally

reinforced CMU wall will generate large amounts of energetic debris that could cause collateral damage to adjacent structures and personnel.

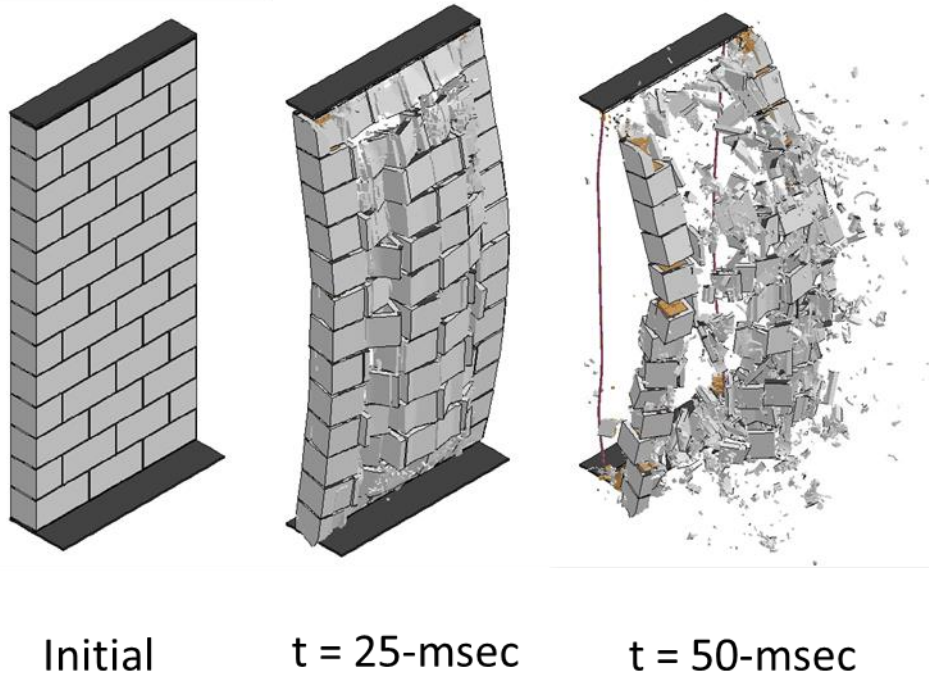


Figure 43. Response of partially grouted CMU wall ($p=50$ -psi, $t=100$ -msec) as predicted by LS-DYNA.

APPENDIX B: LARGE DIAMETER SHOCK TUBE PRESSURE DATA

Test 17 - P0 A-Location
Glass Sample

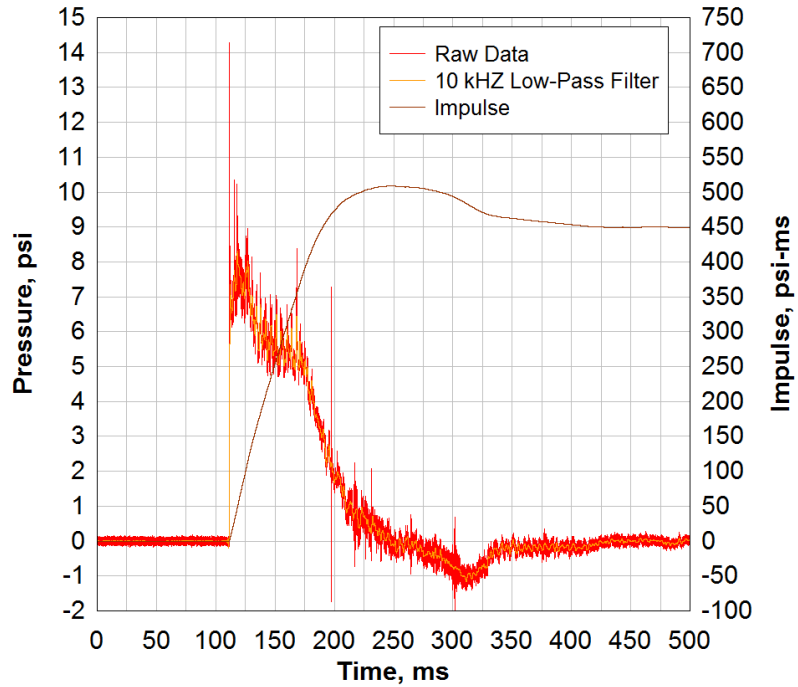


Figure 44. Test 17 P0 A-location pressure gauge data.

Test 17 - P0 B-Location
Glass Sample

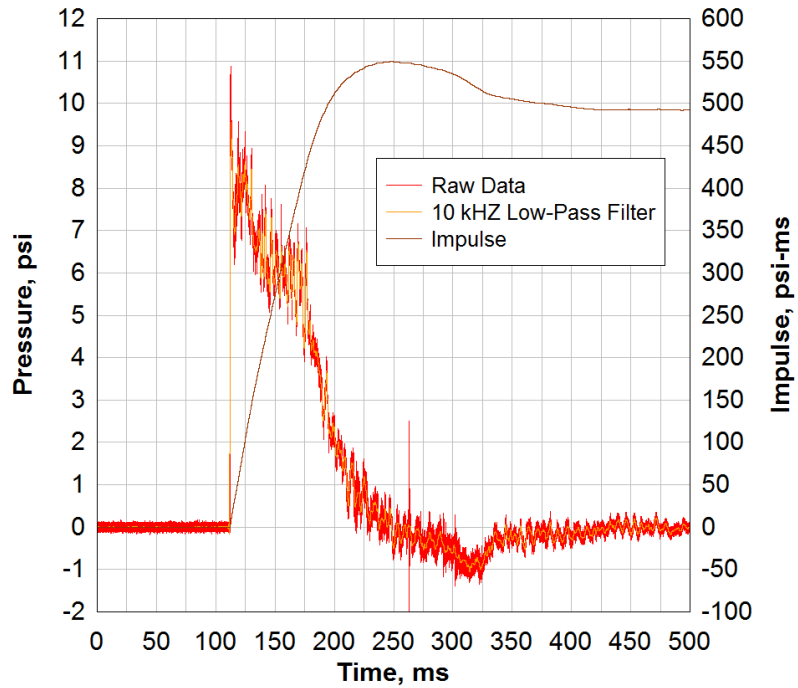


Figure 45. Test 17 P0 B-location pressure gauge data.

Test 17 - P1 East
Glass Sample

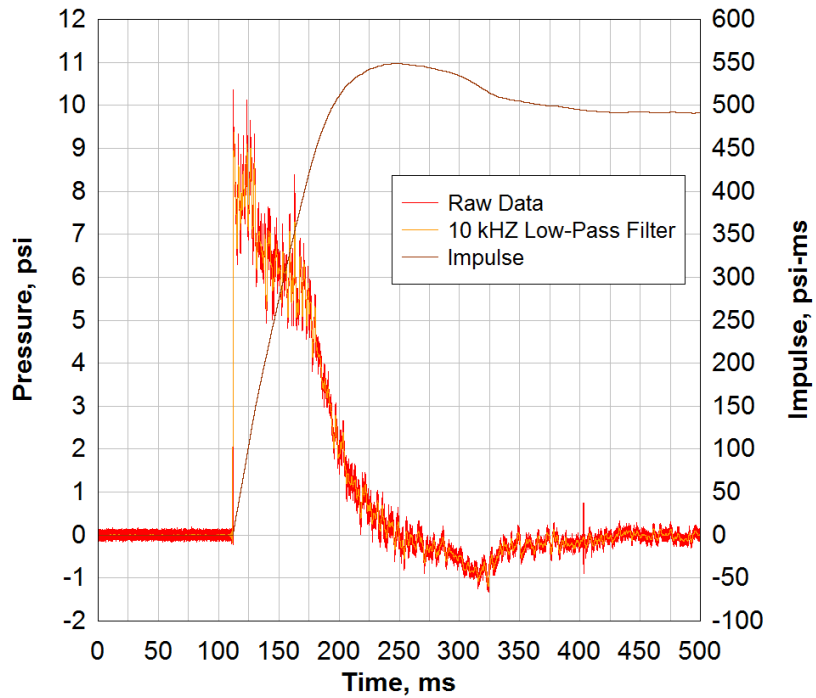


Figure 46. Test 17 P1 east pressure gauge data.

Test 17 - P1 West
Glass Sample

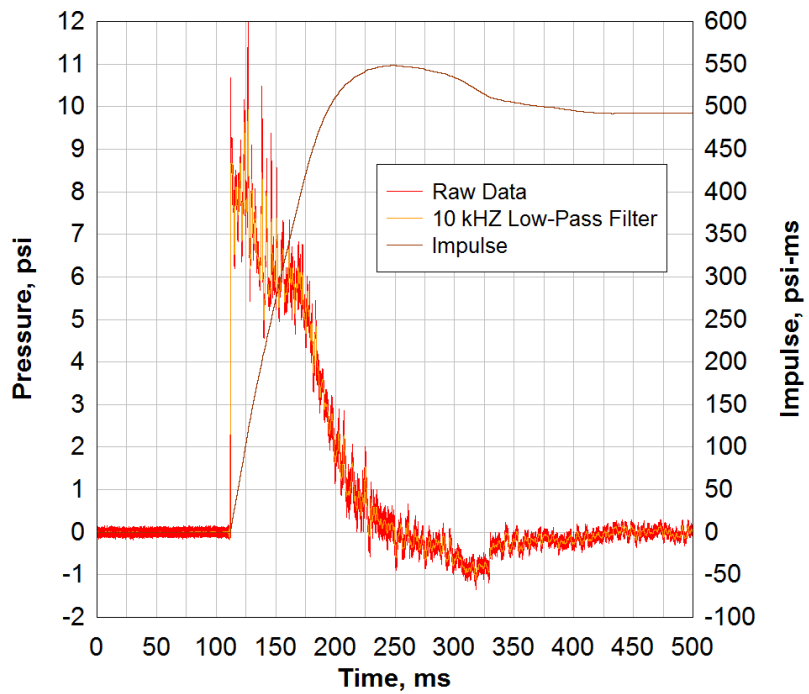


Figure 47. Test 17 P1 west pressure gauge data.

Test 17 - P12
Glass Sample

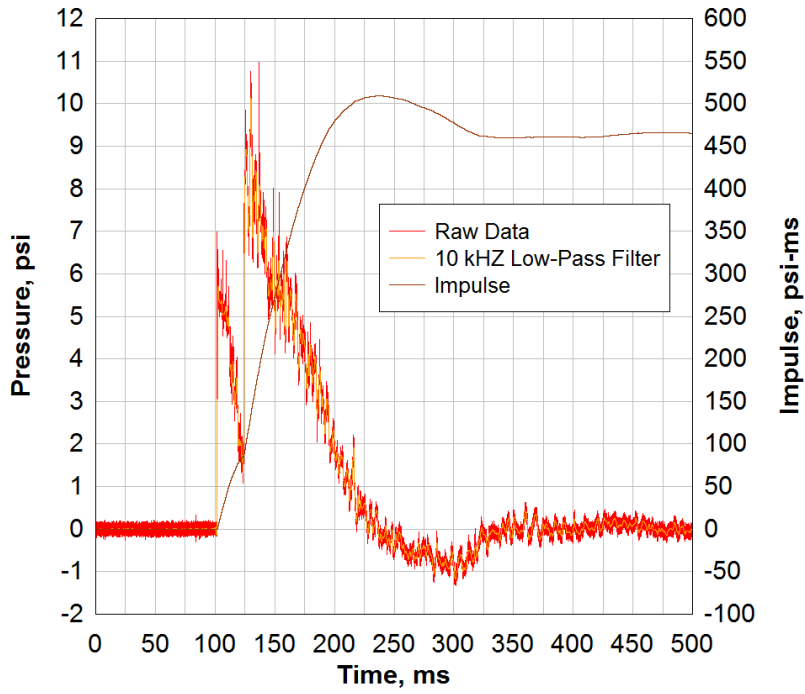


Figure 48. Test 17 P12 pressure gauge data.

Test 17 - P20
Glass Sample

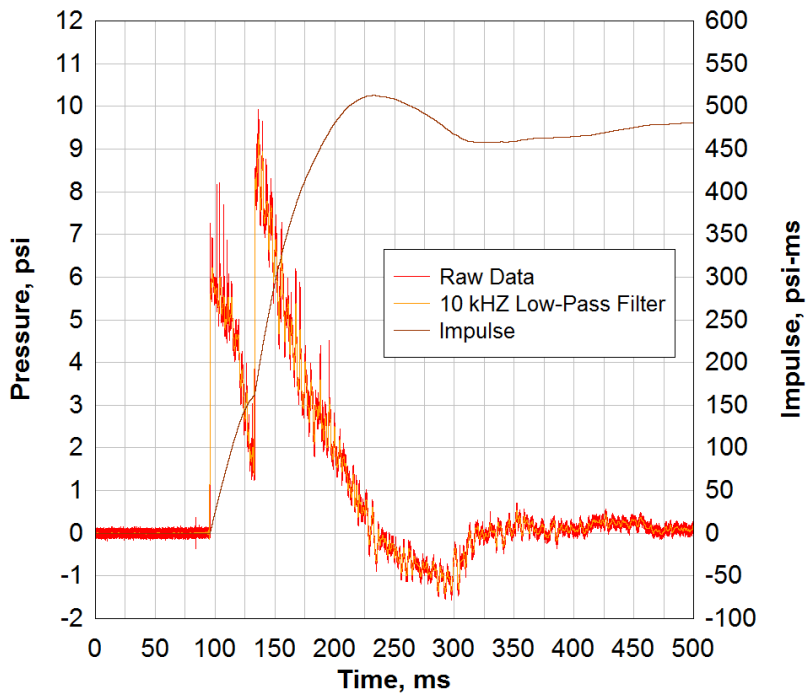


Figure 49. Test 17 P20 pressure gauge data.

Test 17 - P39
Glass Sample

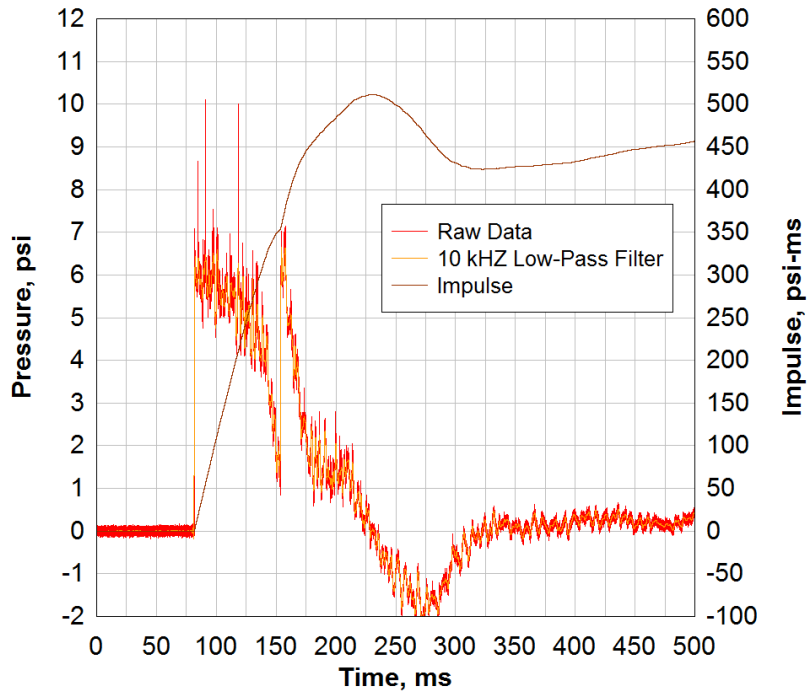


Figure 50. Test 17 P39 pressure gauge data.

Test 17 - P80
Glass Sample

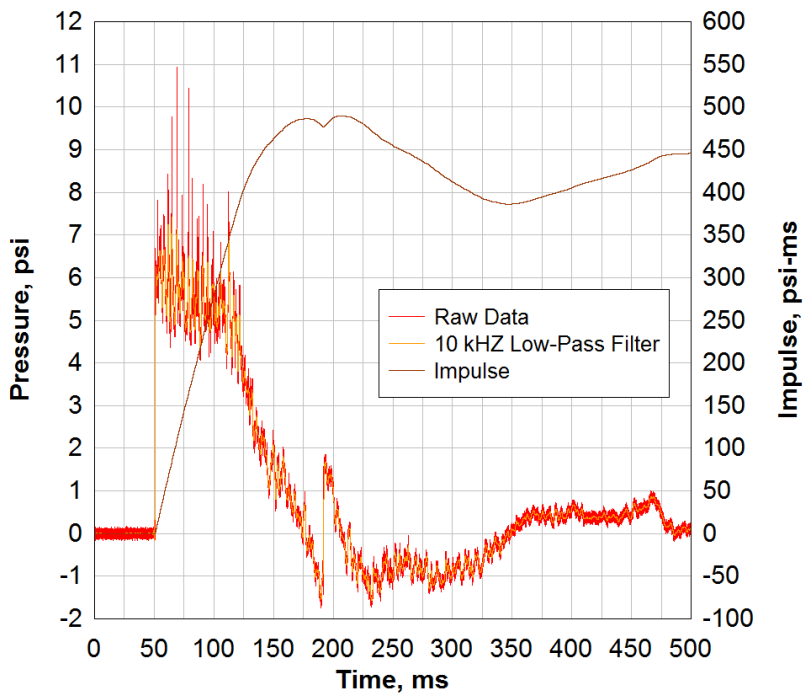


Figure 51. Test 17 P80 pressure gauge data.

Test 17 - P118
Glass Sample

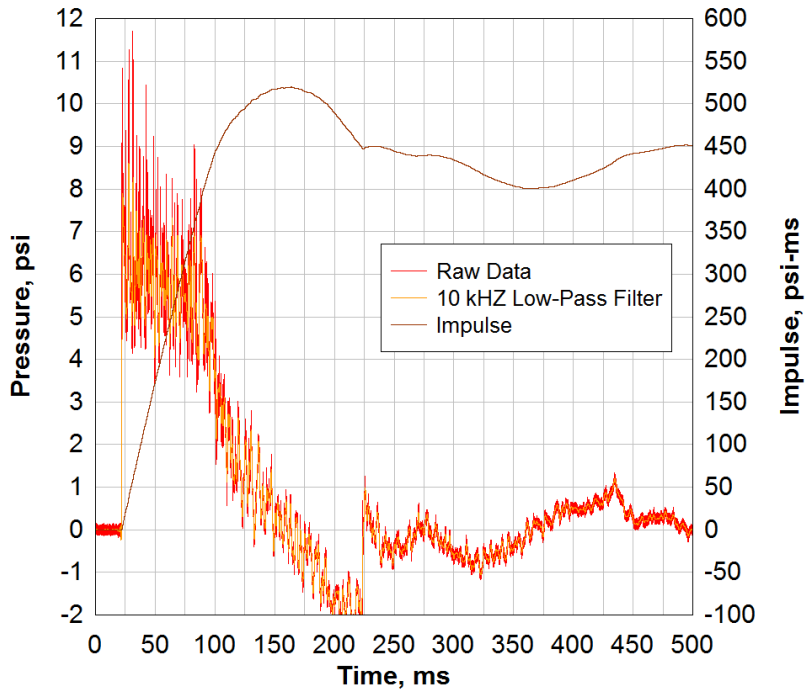


Figure 52. Test 17 P118 pressure gauge data.

Test 17 - P176
Glass Sample

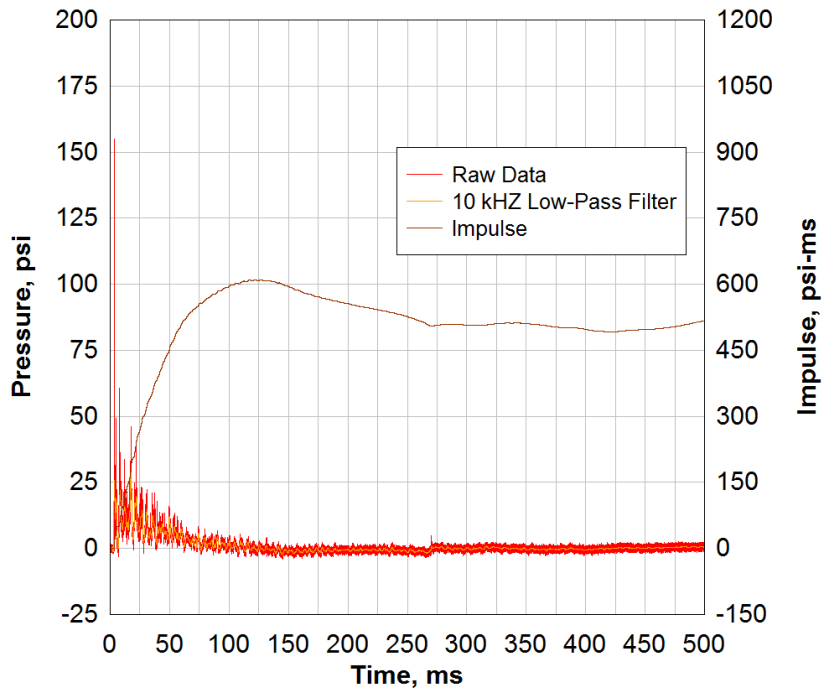


Figure 53. Test 17 P176 pressure gauge data.

Test 18 - P0 A
Glass Sample

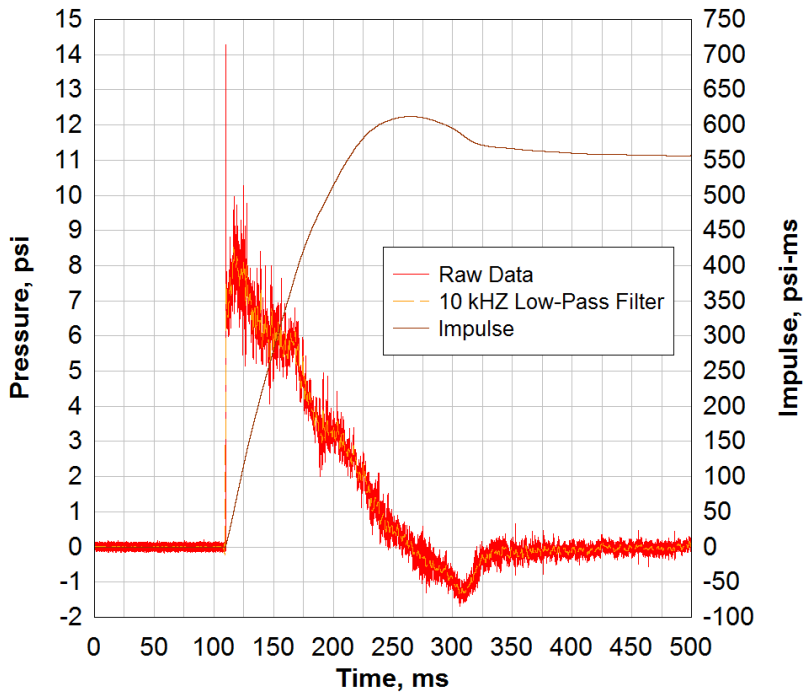


Figure 54. Test 18 P0 A-location pressure gauge data.

Test 18 - P0 B
Glass Sample

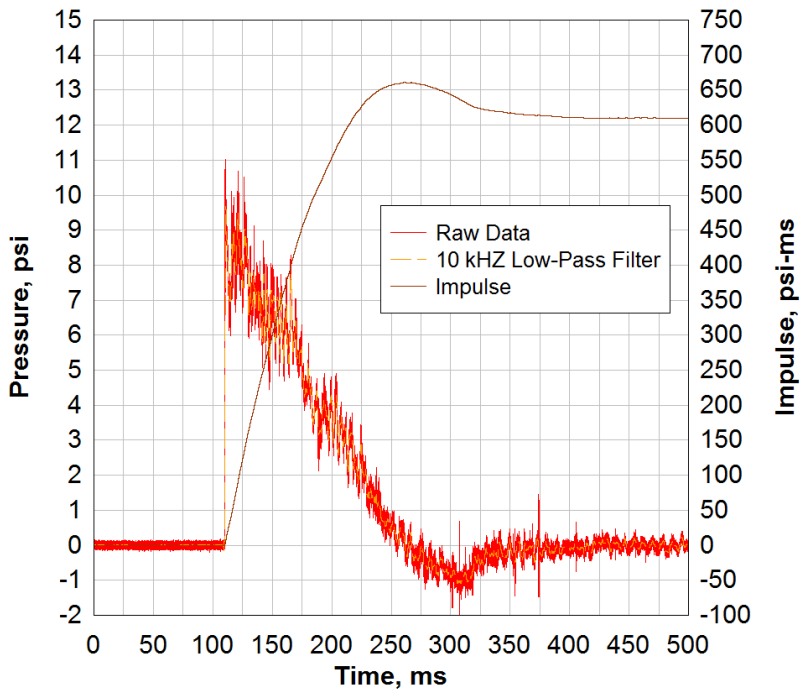


Figure 55. Test 18 P0 B-location pressure gauge data.

Test 18 - P1 East
Glass Sample

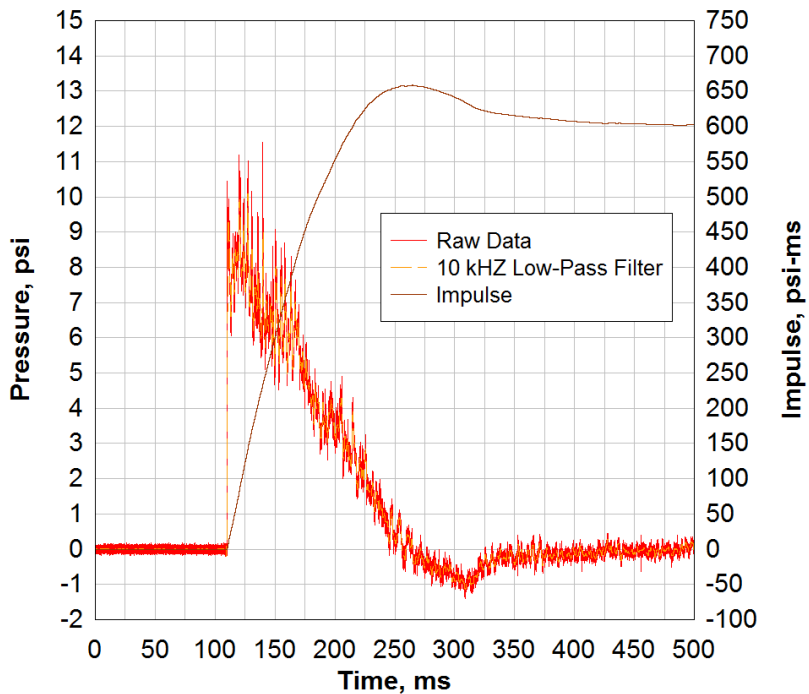


Figure 56. Test 18 P1 east pressure gauge data.

Test 18 - P1 West
Glass Sample

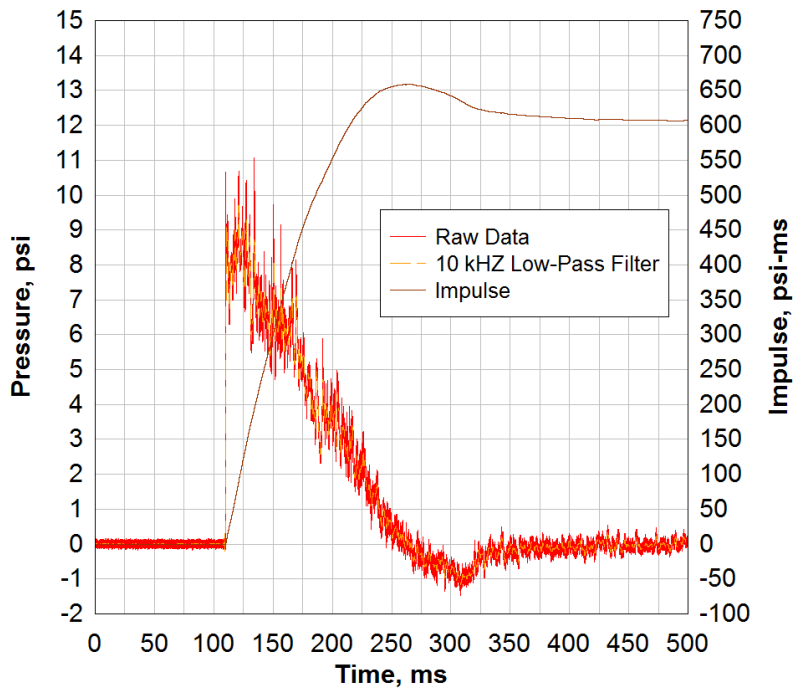


Figure 57. Test 18 P1 west pressure gauge data.

Test 18 - P12
Glass Sample

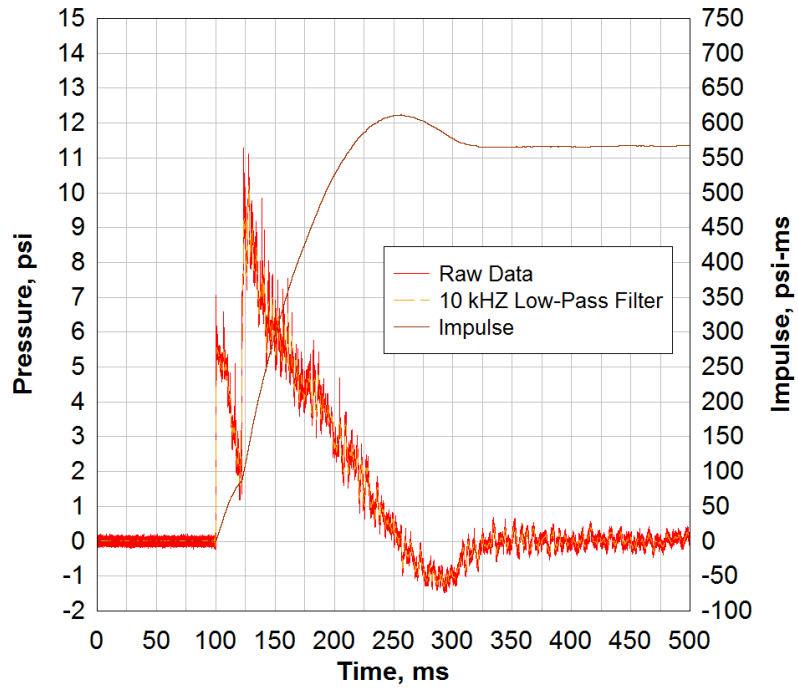


Figure 58. Test 18 P12 pressure gauge data.

Test 18 - P20
Glass Sample

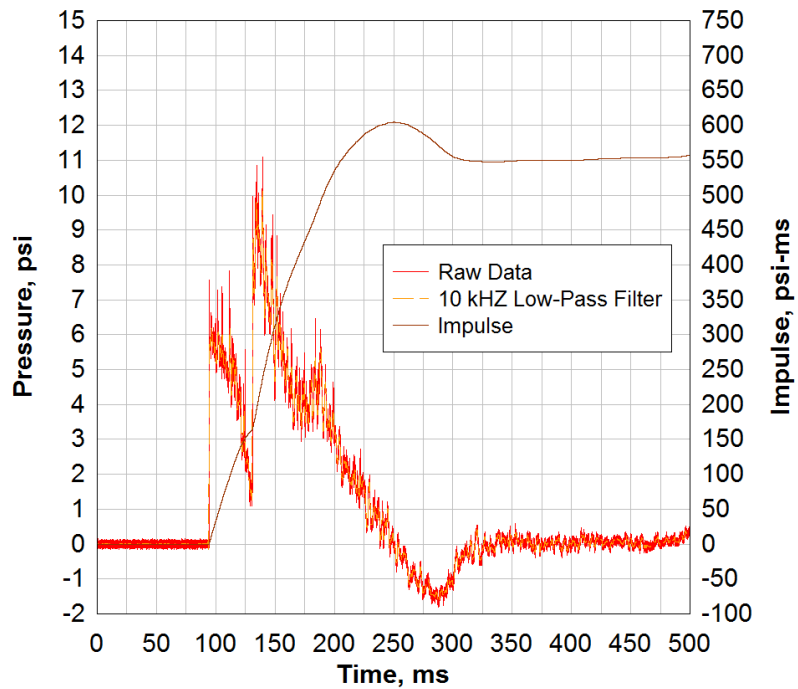


Figure 59. Test 18 P20 pressure gauge data.

Test 18 - P39
Glass Sample

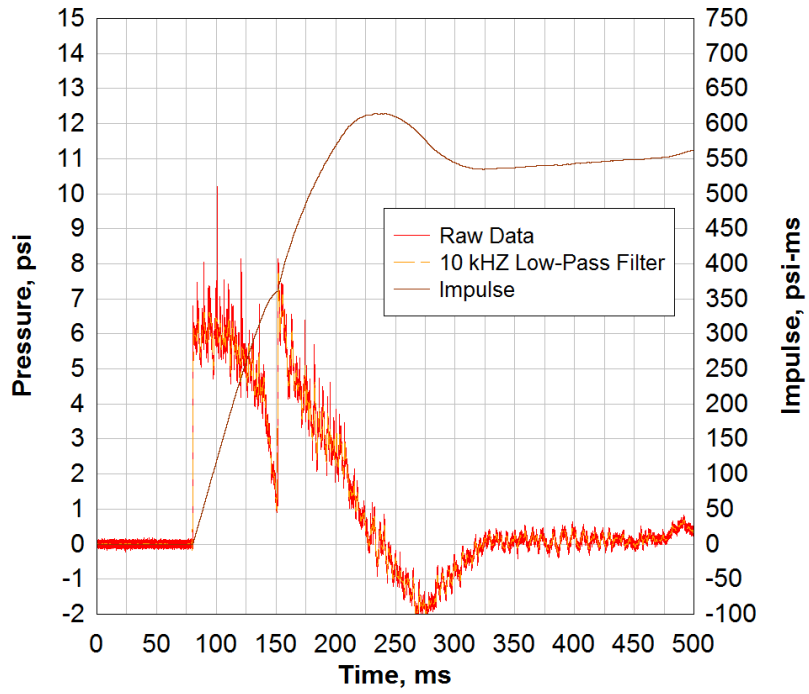


Figure 60. Test 18 P39 pressure gauge data.

Test 18 - P80
Glass Sample

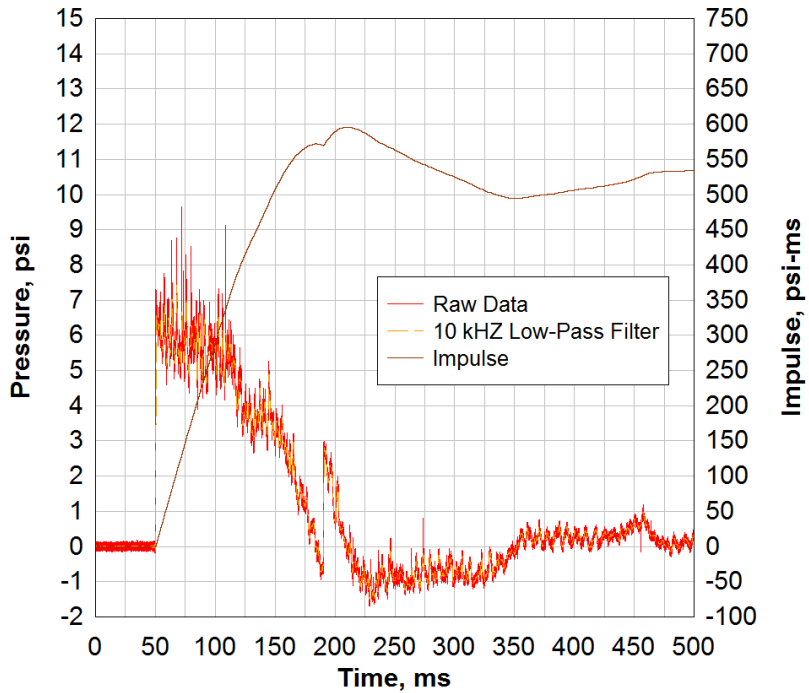


Figure 61. Test 18 P80 pressure gauge data.

Test 18 - P118
Glass Sample

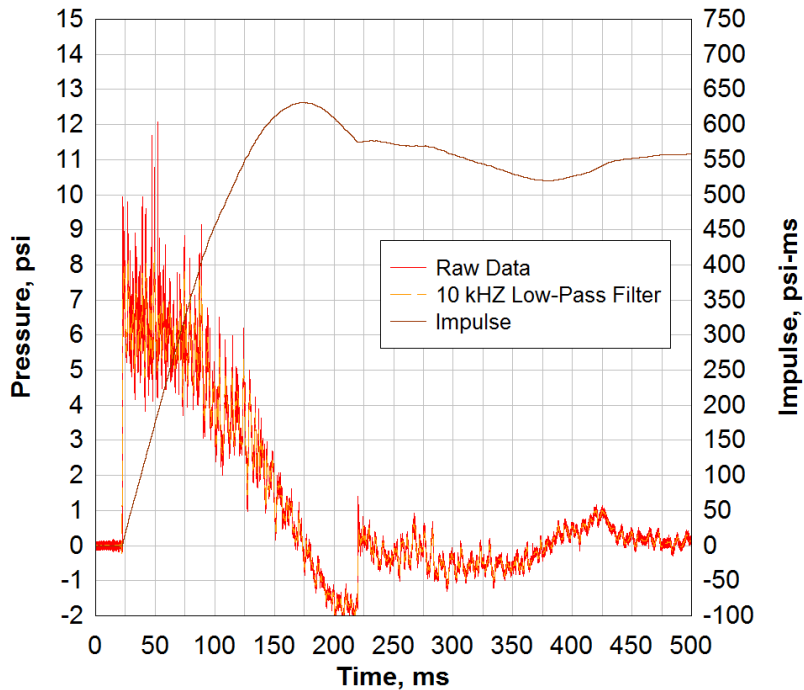


Figure 62. Test 18 P118 pressure gauge data.

Test 18 - P176
Glass Sample

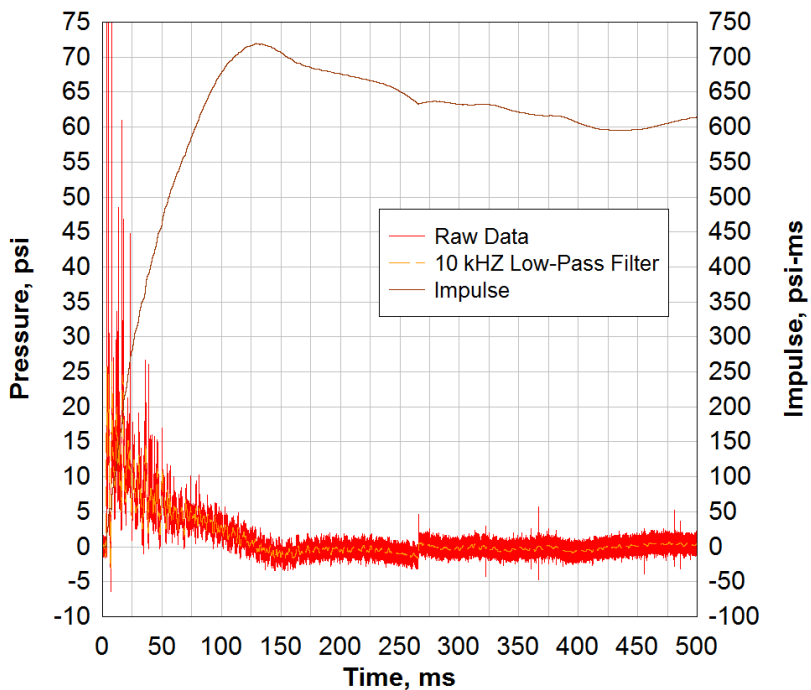


Figure 63. Test 18 P176 pressure gauge data.

Test 19 - P0 A
Glass Sample

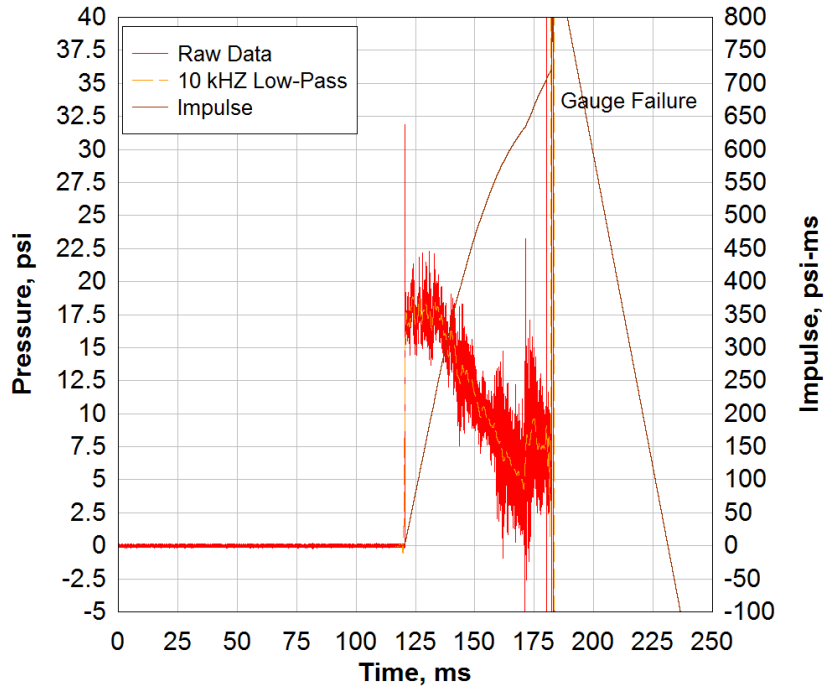


Figure 64. Test 19 P0 A-location pressure gauge data.

Test 19 - P0 B
Glass Sample

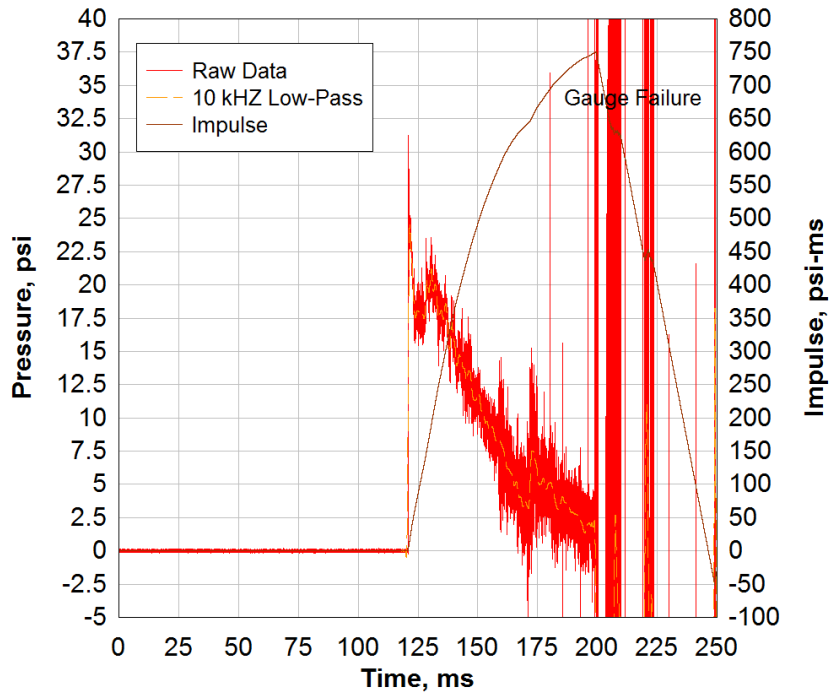


Figure 65. Test 19 P0 B-location pressure gauge data.

Test 19 - P1 East
Glass Sample

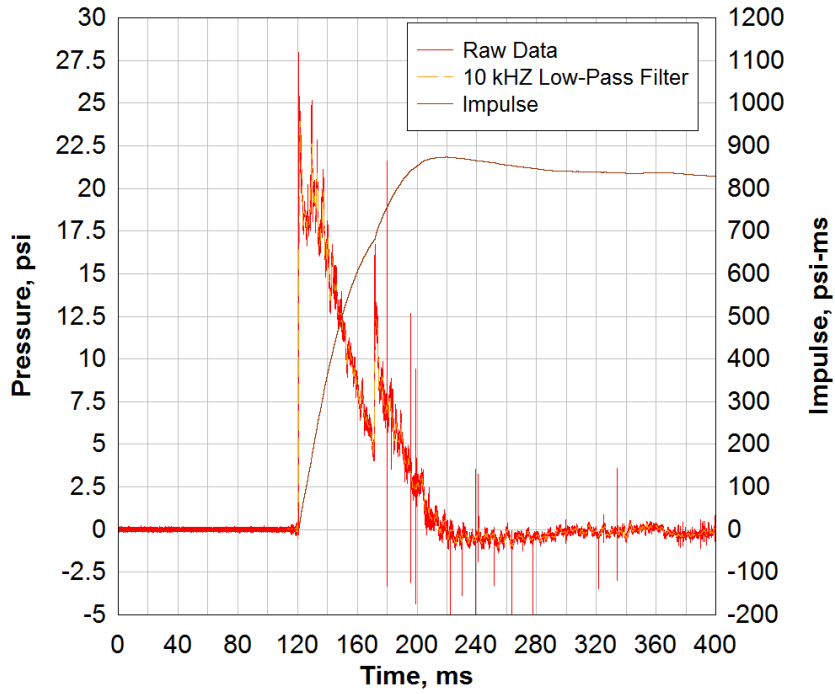


Figure 66. Test 19 P1 east pressure gauge data.

Test 19 - P1 West
Glass Sample

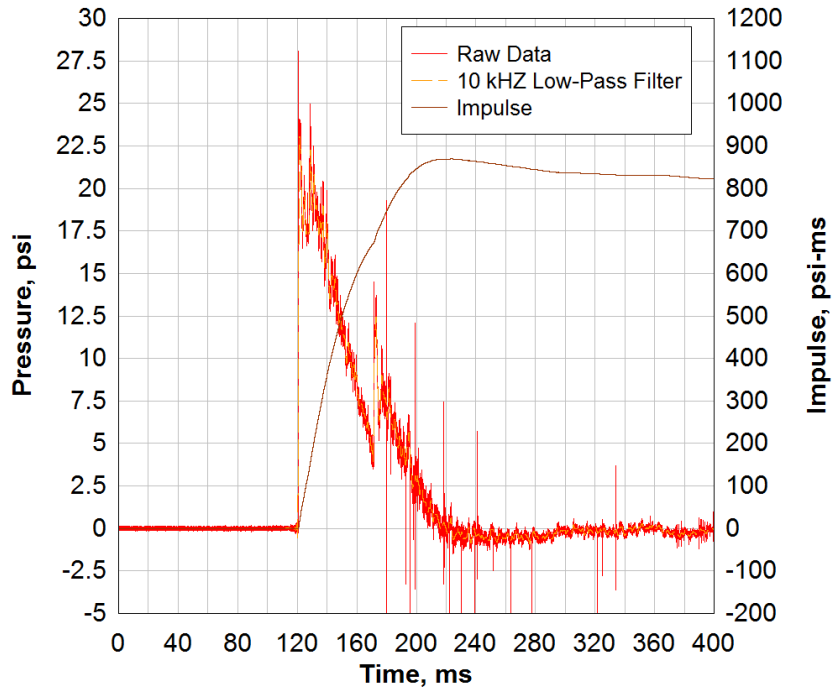


Figure 67. Test 19 P1 west pressure gauge data.

Test 19 - P12
Glass Sample

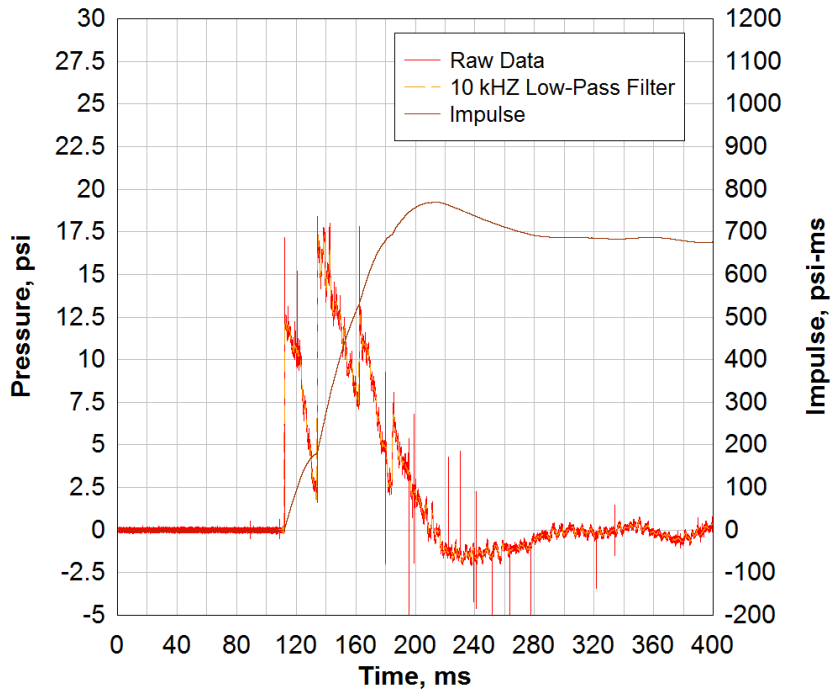


Figure 68. Test 19 P12 pressure gauge data.

Test 19 - P20
Glass Sample

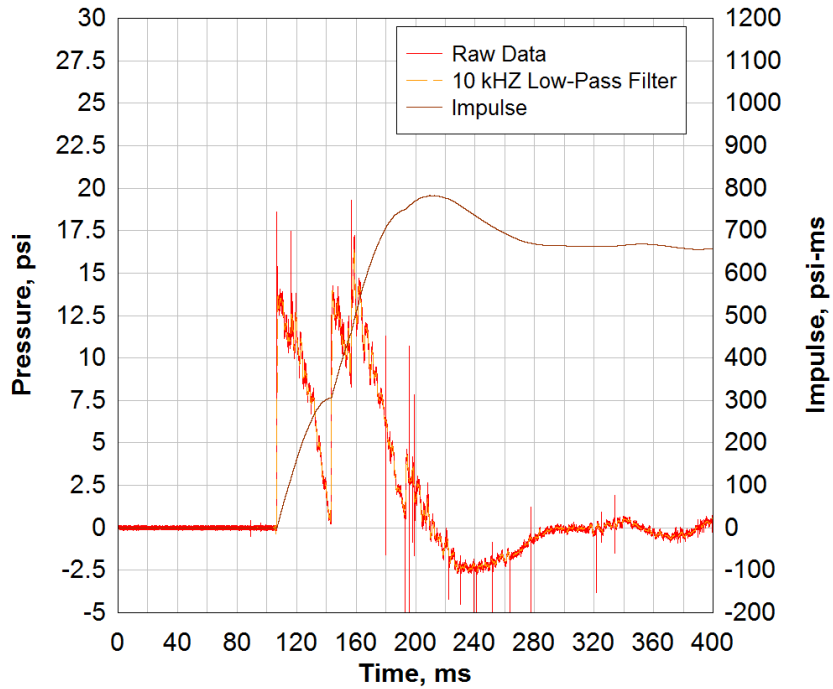


Figure 69. Test 19 P20 pressure gauge data.

Test 19 - P39
Glass Sample

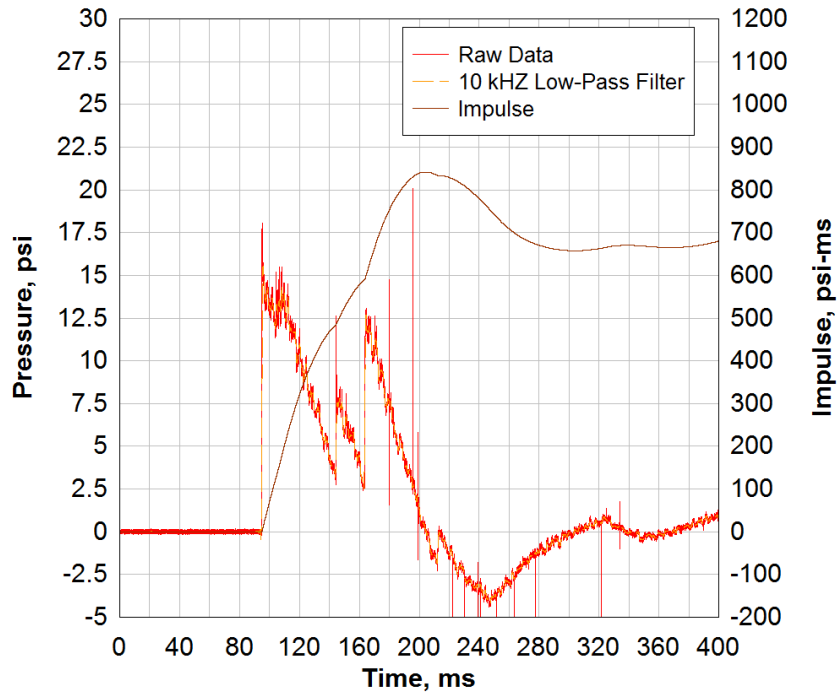


Figure 70. Test 19 P39 pressure gauge data.

Test 19 - P80
Glass Sample

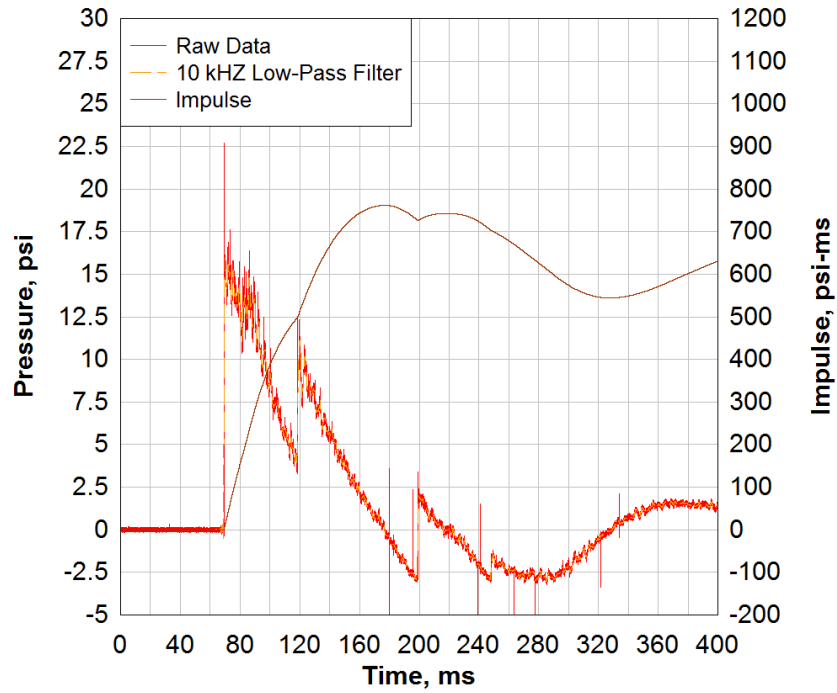


Figure 71. Test 19 P80 pressure gauge data.

Test 19 - P118
Glass Sample

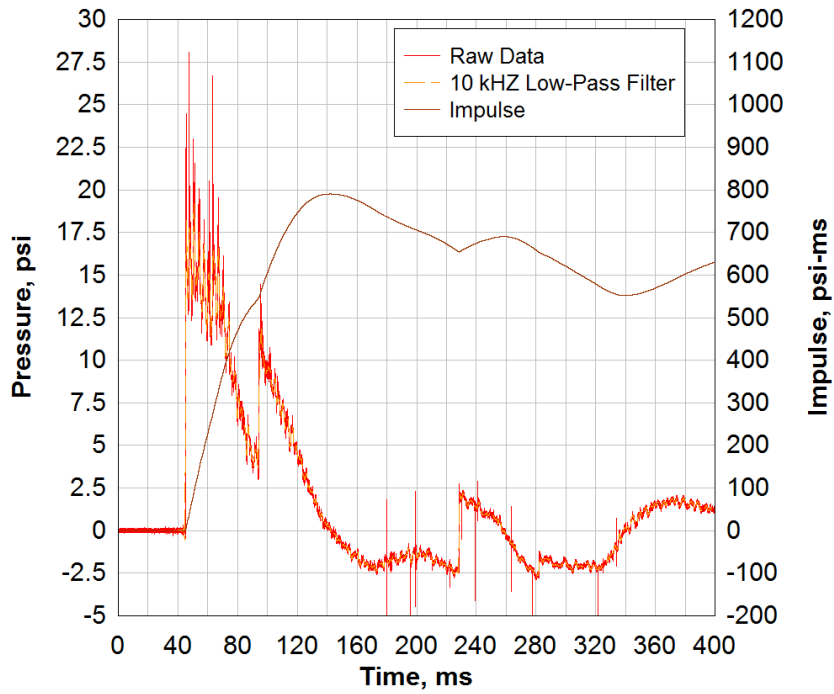


Figure 72. Test 19 P118 pressure gauge data.

Test 19 - P176
Glass Sample

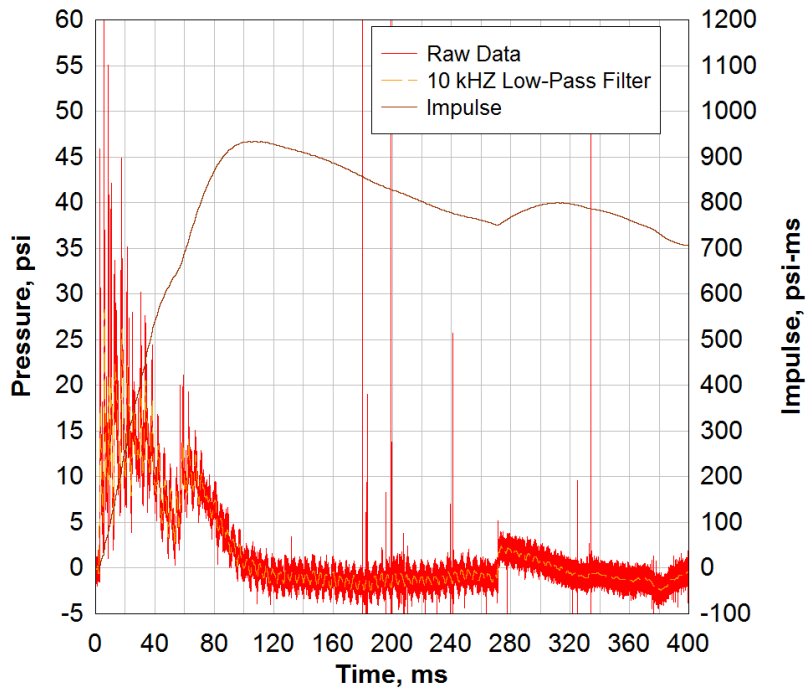


Figure 73. Test 19 P176 pressure gauge data.

Test 20 - P1 East
CMU Sample

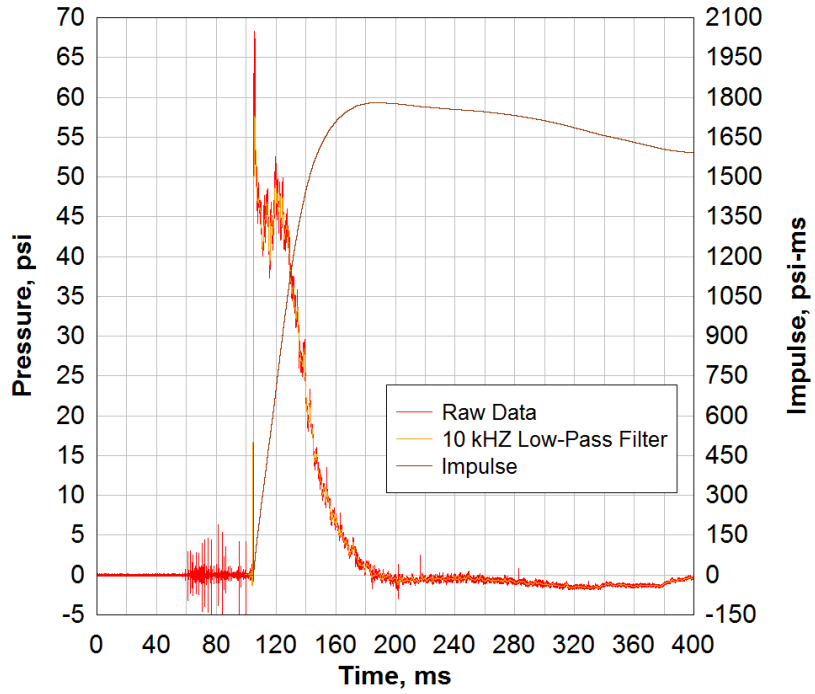


Figure 74. Test 20 P1 east pressure gauge data.

Test 19 - P1 West
CMU Sample

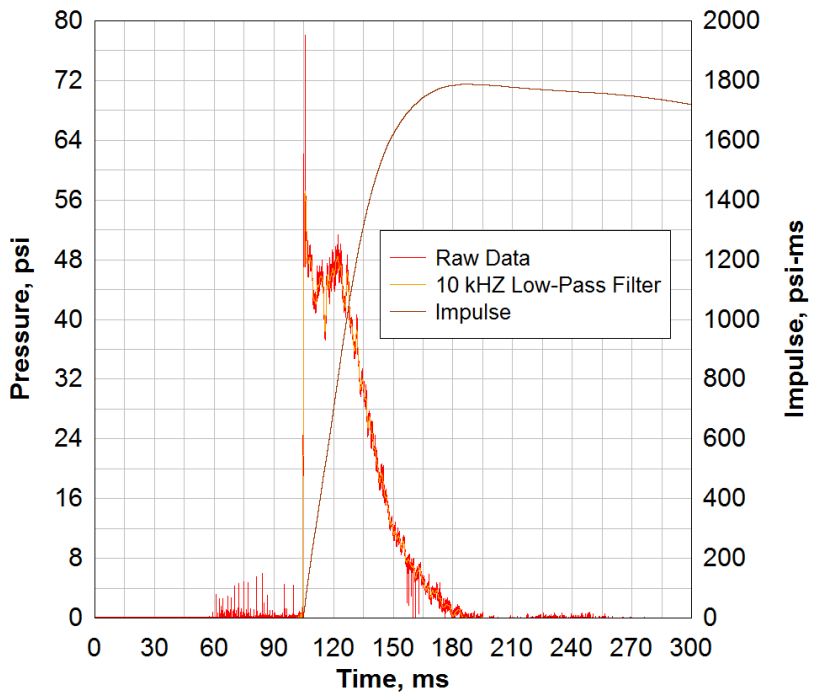


Figure 75. Test 20 P1 west pressure gauge data.

Test 19 - P12
CMU Sample

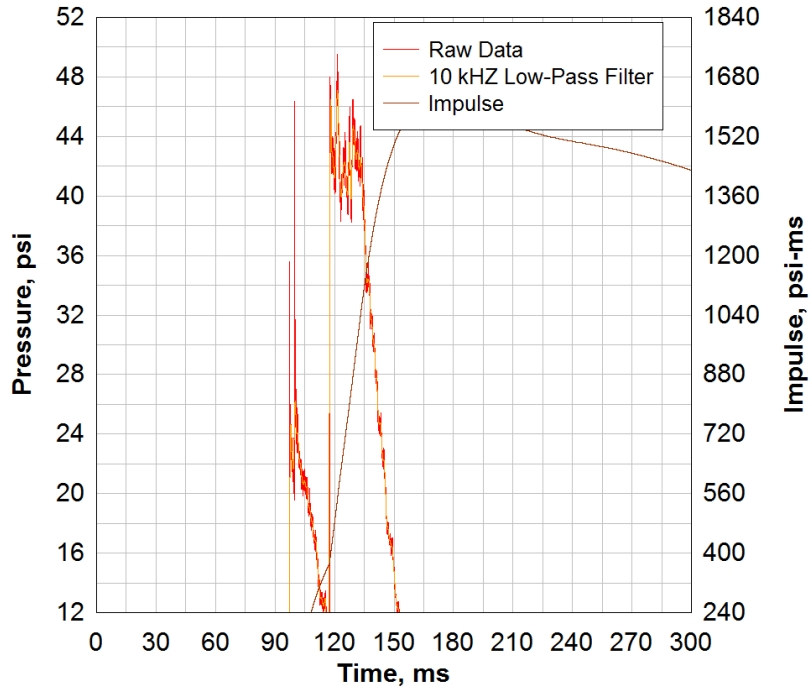


Figure 76. Test 20 P12 pressure gauge data.

Test 19 - P20
CMU Sample

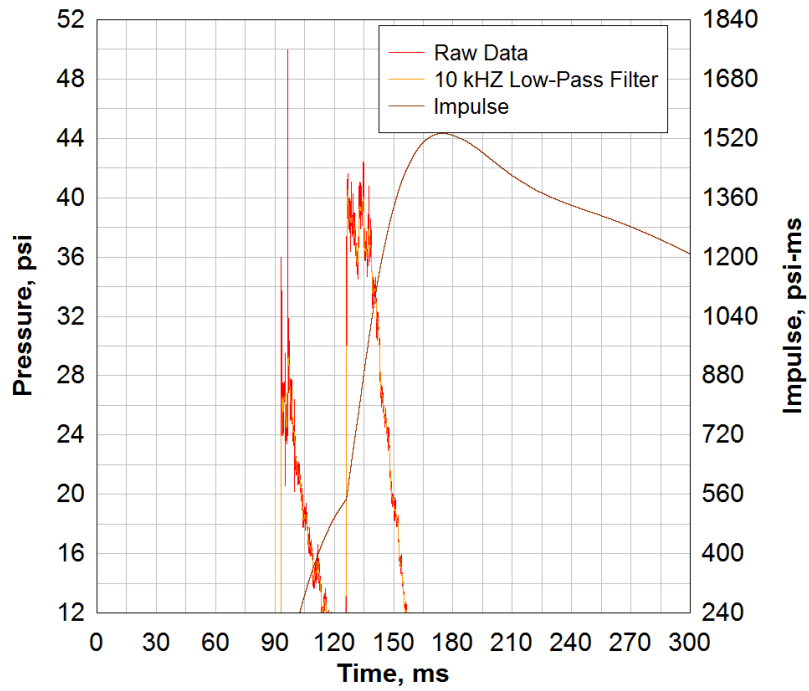


Figure 77. Test 20 P20 pressure gauge data.

Test 19 - P39
CMU Sample

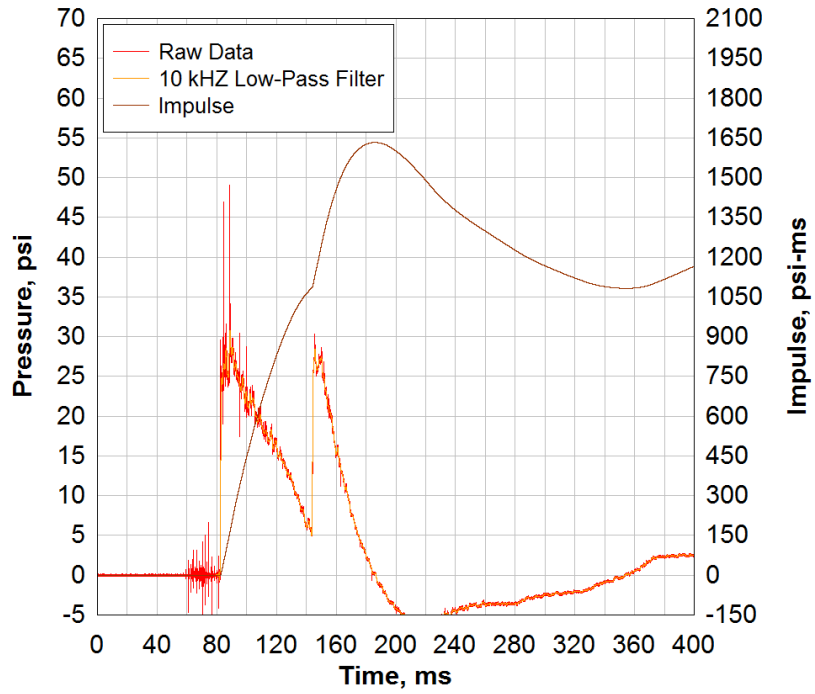


Figure 78. Test 20 P39 pressure gauge data.

Test 19 - P80
CMU Sample

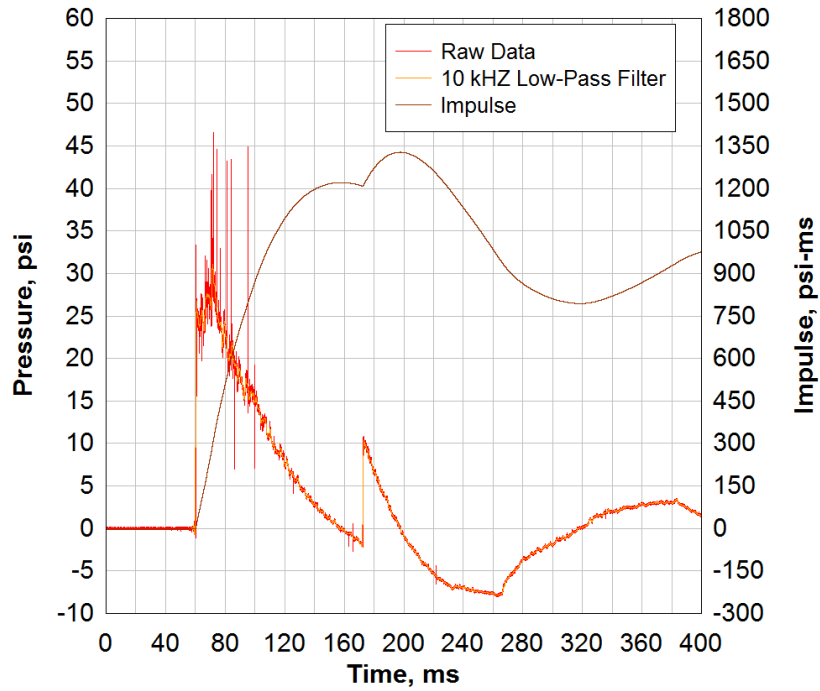


Figure 79. Test 20 P80 pressure gauge data.

Test 19 - P118
CMU Sample

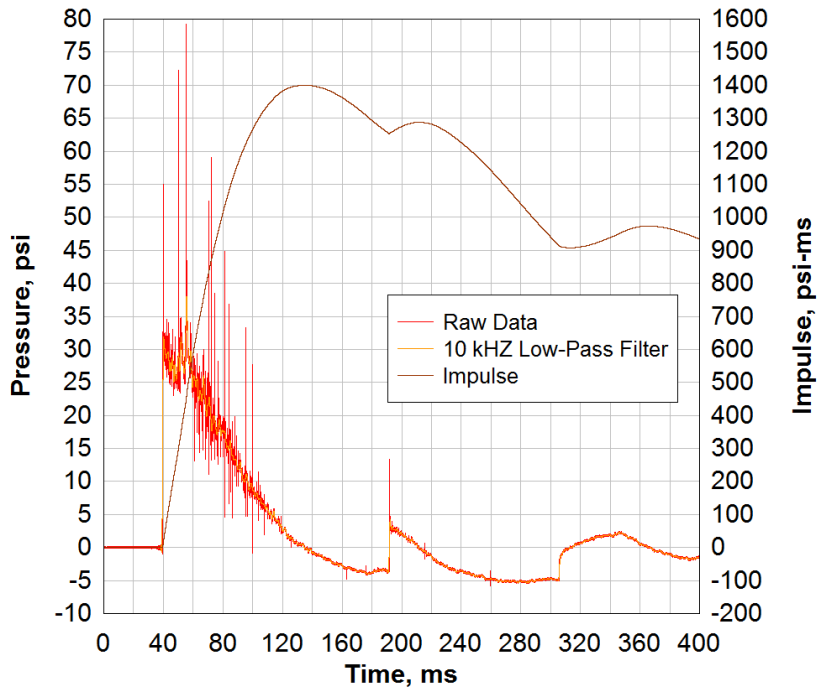


Figure 80. Test 20 P118 pressure gauge data.

Test 19 - P176
CMU Sample

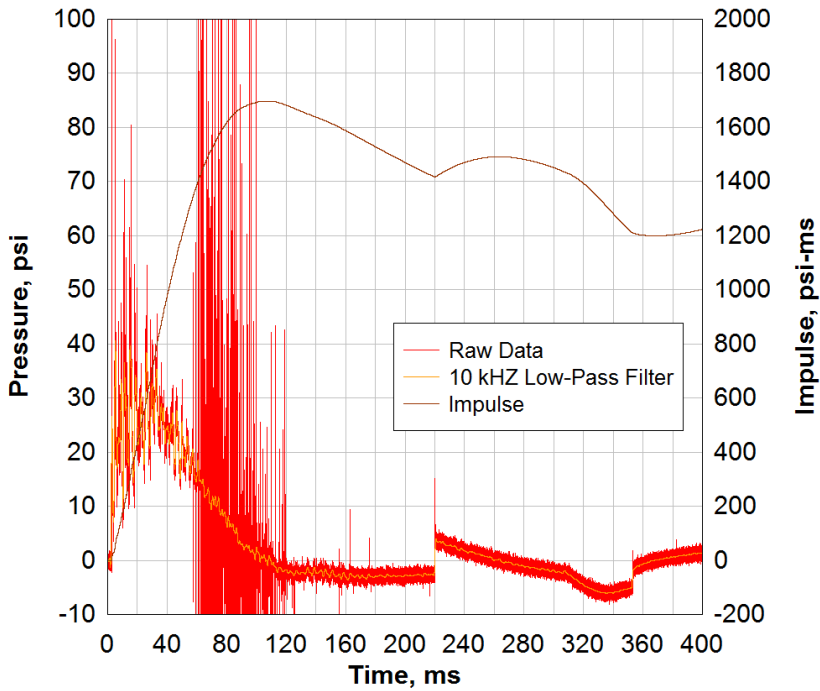


Figure 81. Test 20 P176 pressure gauge data.

Test 21 - P1 East
Concrete Sample

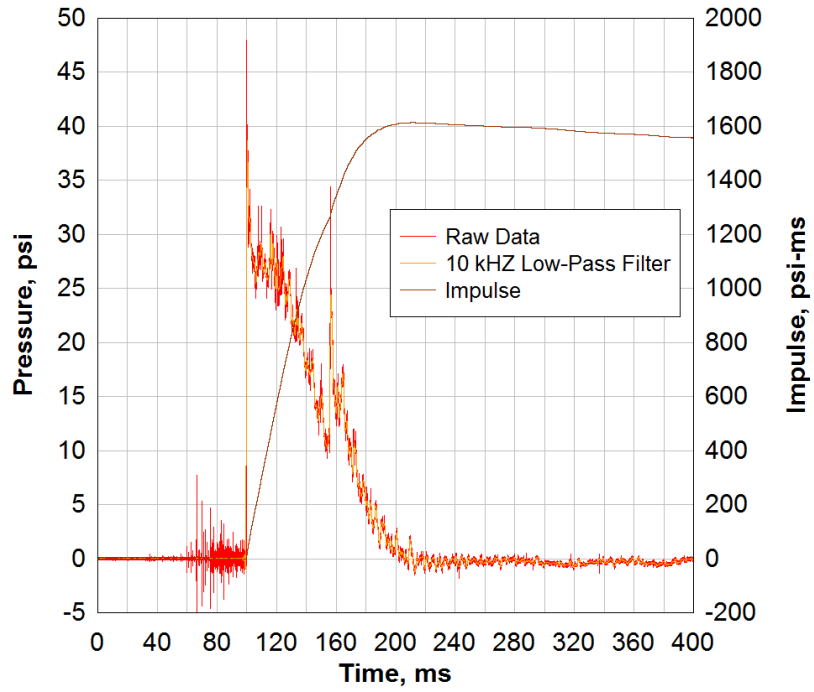


Figure 82. Test 21 P1 east pressure gauge data.

Test 21 - P1 West
Concrete Sample

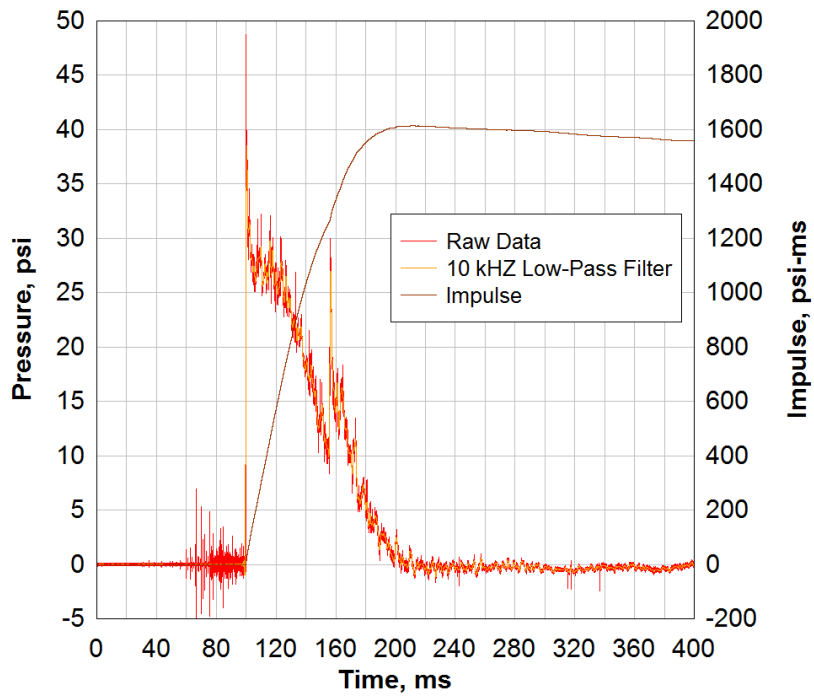


Figure 83. Test 21 P1 west pressure gauge data.

Test 21 - P12
Concrete Sample

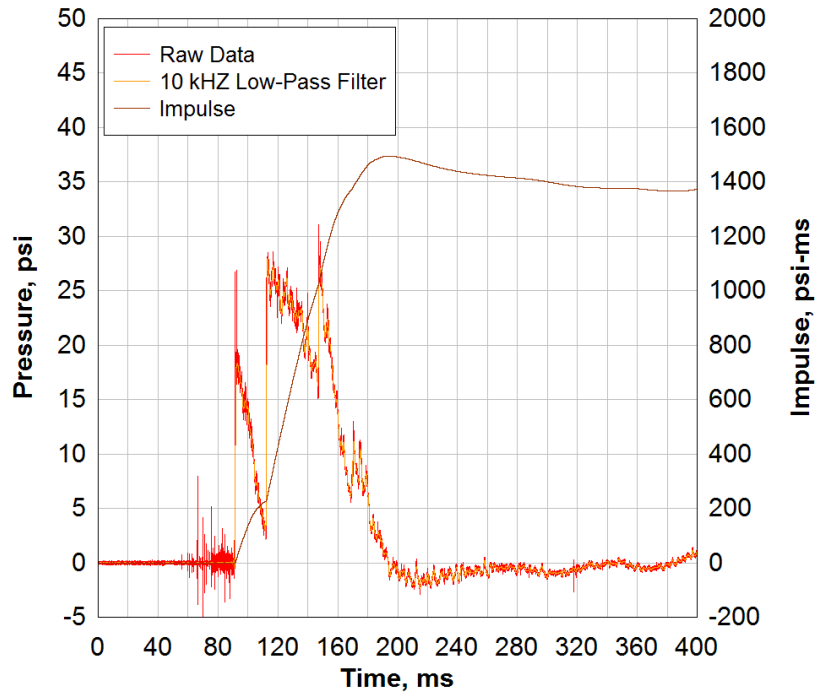


Figure 84. Test 21 P12 pressure gauge data.

Test 21 - P20
Concrete Sample

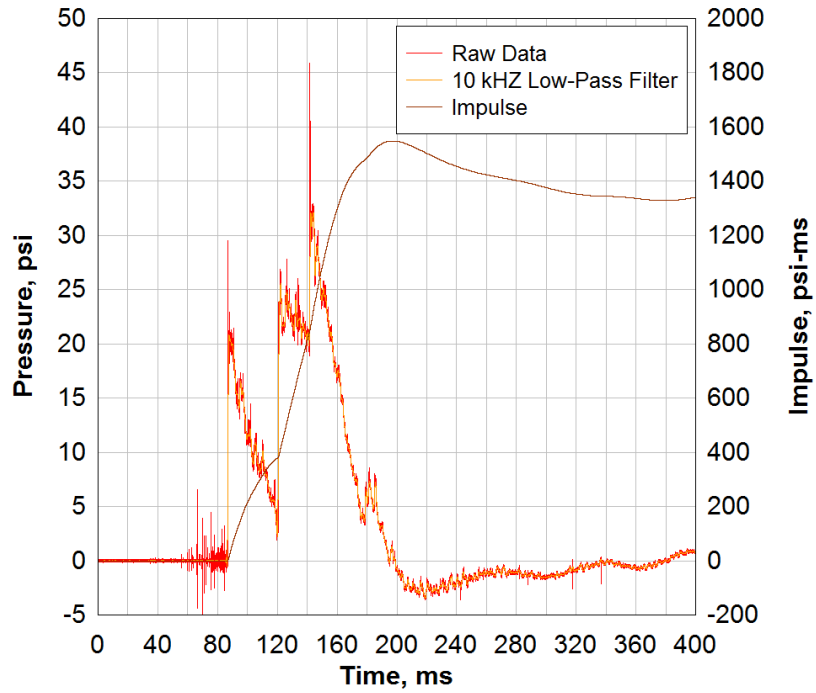


Figure 85. Test 21 P20 pressure gauge data.

Test 21 - P39
Concrete Sample

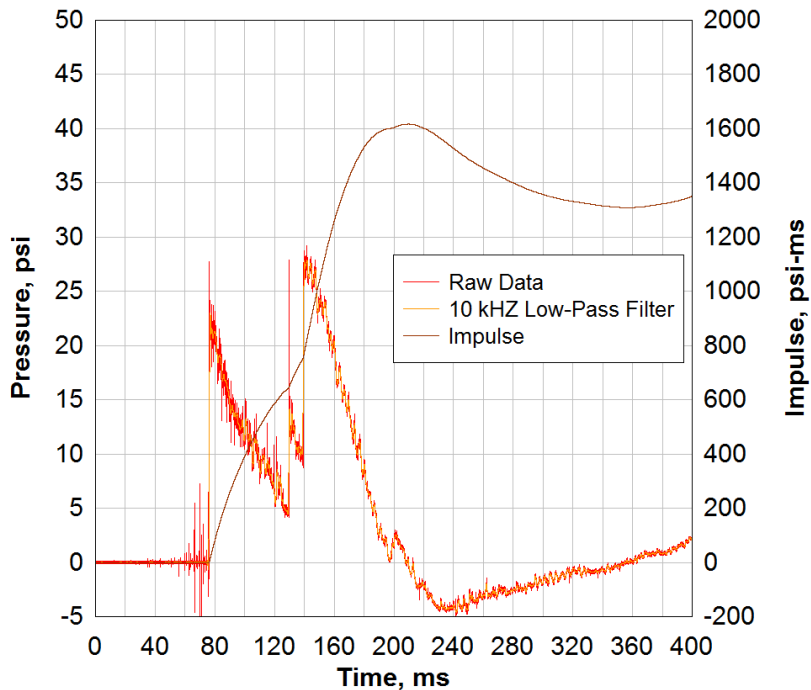


Figure 86. Test 21 P39 pressure gauge data.

Test 21 - P80
Concrete Sample

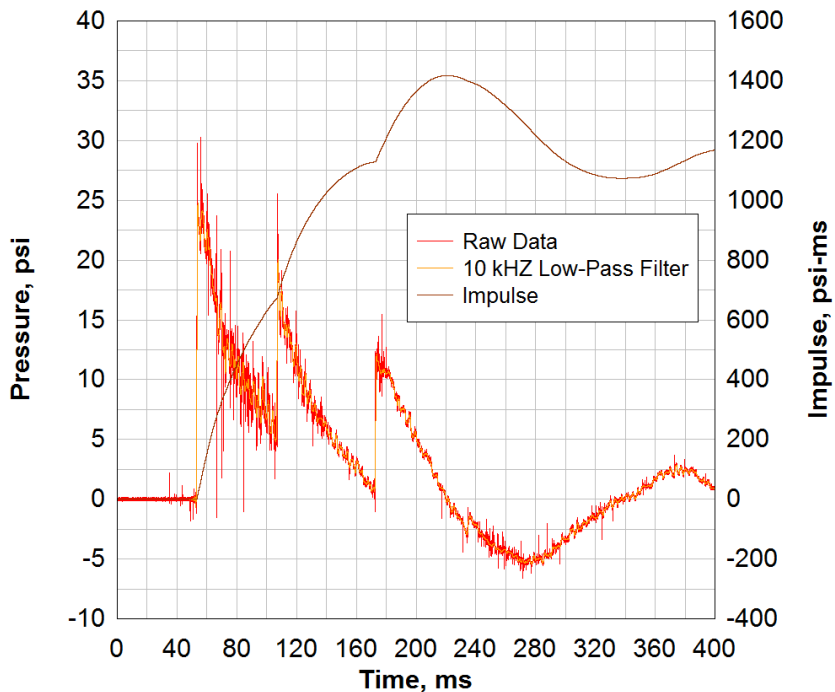


Figure 87. Test 21 P80 pressure gauge data.

Test 21 - P118
Concrete Sample

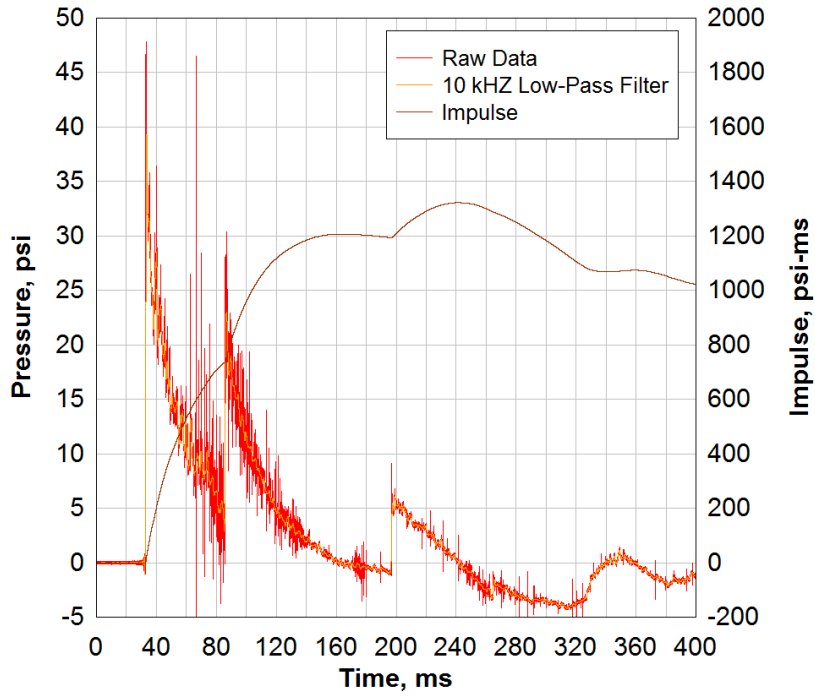


Figure 88. Test 21 P118 pressure gauge data.

Test 21 - P176
Concrete Sample

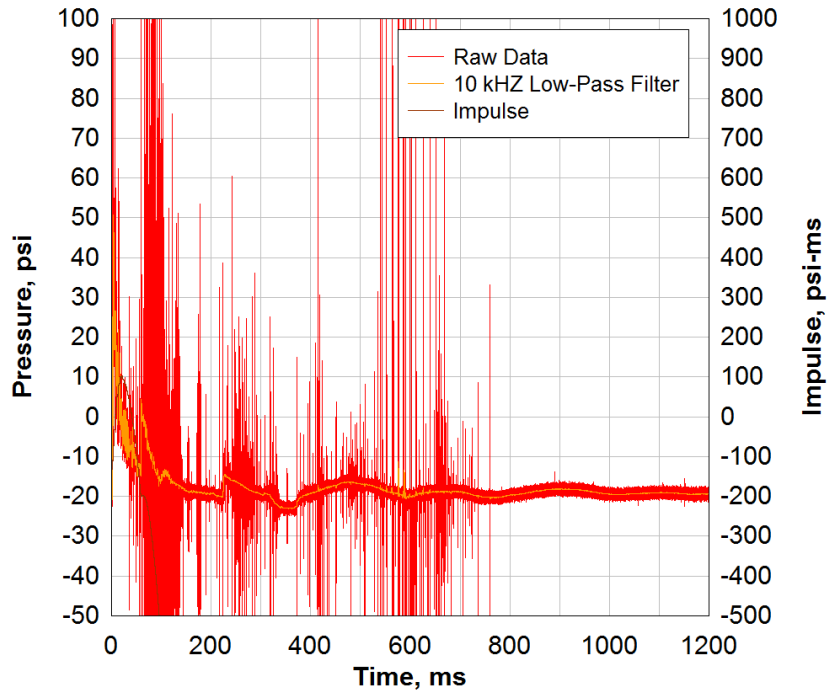


Figure 89. Test 21 P176 pressure gauge data.